

## DIPLOMARBEIT

# SURFACES OF TRANSITION-METAL **OXIDES**

ausgeführt am Institut für Angewandte Physik an der Technischen Universität Wien

unter der Anleitung von

Univ.Prof.in Dipl.-Ing.in Dr.in techn. Ulrike Diebold

Dr. Michele Riva

und

Dr. Erik Rheinfrank

eingereicht von

Marie Kienzer

01535340

Wien, September 2024

## Kurzfassung

Übergangsmetalloxide (TMOs) weisen ein breites Spektrum an elektronischen, magnetischen und katalytischen Eigenschaften auf, was sie für verschiedene technologische Anwendungen wie Katalyse, Elektronik und für Systeme zur Energieumwandlung sehr interessant macht. Die Oberflächeneigenschaften eines Materials spielen eine entscheidende Rolle für seine Leistungsfähigkeit, da die atomare Anordnung an der Oberfläche die chemische Reaktivität und das elektronische Verhalten stark beeinflusst. Niederenergetische Elektronenbeugung (low-energy electron diffraction, LEED) in Kombination mit Intensität–Spannungs–Analyse — LEED I(V) — ist eine leistungsfähige Technik zur Untersuchung der atomaren Struktur von Oberflächen.

Die vorliegende Masterarbeit umfasst oberflächenwissenschaftliche Untersuchungen an  $SrTiO_3(110)$ ,  $La_{0.8}Sr_{0.2}MnO_3(001)$  (LSMO) und  $Cu_2O(111)$ . Verschiedene Methoden um gut definierte Oberflächenrekonstruktionen zu erhalten und zu charakterisieren wurden angewandt. An diesen Oberflächenrekonstruktionen wurden dann LEED-I(V)-Messungen durchgeführt.

Die Präparation von SrTiO<sub>3</sub> umfasst die Abscheidung von Sr mittels Molekularstrahlepitaxie (molecular-beam epitaxy, MBE) oder Ar<sup>+</sup> Sputtering, jeweils gefolgt von Heizen in einer Sauerstoffumgebung, wobei der Einfluss dieser Methoden auf die Struktur der (110)-Oberfläche verdeutlicht wird. Die Herausforderungen bei der LEED-I(V)-Datenerfassung unterstreichen die Relevanz einer genauen Nachbearbeitung. LSMO(001)-Filme wurden auf einem SrTiO<sub>3</sub>(001)-Substrat durch Laserstrahlverdampfen (pulsed-laser deposition, PLD) und Ar<sup>+</sup> Sputtering hergestellt. Durch Heizen bei unterschiedlichen Sauerstoffpartialdrücken und Temperaturen konnten zwei verschiedene Phasen der Cu<sub>2</sub>O(111)-Oberfläche erzielt werden. Allerdings traten Schwierigkeiten auf, insbesondere eine mangelnde Reproduzierbarkeit, da die Oberflächeneigenschaften stark von der Vorgeschichte des Kristalls abhängig waren.

Die LEED-I(V)-Daten für diese fünf Oberflächenrekonstruktionen, die mit Struktursimulationen verglichen werden, sollen in Zukunft dazu beitragen, das Verständnis der atomaren Anordnungen auf den Oberflächen zu verbessern.

## Abstract

Transition-metal oxides (TMOs) display a wide range of electronic, magnetic, and catalytic properties, rendering them highly relevant for various technological applications such as catalysis, electronics, and energy-conversion devices. The surface properties of a material play a crucial role in determining its performance, as the atomic arrangement on the surface significantly influences the chemical reactivity and electronic behavior. Low-energy electron diffraction (LEED) combined with intensity-voltage analysis — LEED I(V) — is a powerful technique to investigate the atomic structure of surfaces.

This thesis contains surface-science studies on SrTiO<sub>3</sub>(110), La<sub>0.8</sub>Sr<sub>0.2</sub>MnO<sub>3</sub>(001) (LSMO), and Cu<sub>2</sub>O(111). A variety of surface-science techniques were employed to prepare and characterize well-defined surface reconstructions. LEED-I(V) measurements were then acquired on such surface reconstructions.

The preparation of SrTiO<sub>3</sub> involves depositing Sr via moecular-beam epitaxy (MBE) or Ar<sup>+</sup> sputtering, both followed by oxygen annealing, highlighting the impact of these methods on the (110) surface structure. Challenges in the LEED-I(V)data extraction, such as spot splitting due to antiphase boundaries, emphasize the importance of accurate postprocessing to ensure reliable comparisons with simulated models. LSMO(001) films were grown on a SrTiO<sub>3</sub>(001) substrate using pulsed-laser deposition and Ar<sup>+</sup> sputtering. The comparison of the LEED-I(V)measurements recorded on the same surface structure differently prepared showed that they are in perfect agreement to each other. Two different surface phases of  $Cu_2O(111)$  could be achieved through annealing in varying oxygen partial pressures and temperatures. The preparation encountered challenges, especially a lack in reproducibility, as the surface properties were strongly dependent on the annealing history of the crystal.

The LEED-I(V) data for these five surface reconstructions, compared with ongoing structural calculations, aim to enhance the understanding of the atomic arrangements of the surfaces in the future.



# Contents

1	Intr	oduction
	1.1	Metal-oxide surfaces
		1.1.1 Stability of metal-oxide surfaces
	1.2	Low-energy electron diffraction
		1.2.1 Periodic structures and diffraction
		1.2.2 Diffraction on surfaces
	1.3	Outline of the thesis
2	Exp	perimental methods
	2.1	UHV setup
	2.2	PLD
	2.3	Scanning-probe microscopy
		2.3.1 STM
		2.3.2 AFM
	2.4	XPS
	2.5	LEED
	2.6	Ex-situ preparation
		2.6.1 Sample cleaning
		2.6.2 Sample mounting
3	$\mathbf{SrT}$	${ m iO_3(110)}$ : The $(4 imes1)$ reconstruction
	3.1	Introduction
		3.1.1 Perovskite oxides
	3.2	Structure and surface reconstructions
		3.2.1 The $(4 \times 1)$ reconstruction
	3.3	Sample preparation and characterization
		$3.3.1  SrTiO_3(110) \text{ substrates} \dots 26$
		$3.3.2  (4 \times 1) \text{ preparation} \dots \dots$
		3.3.3 Non-uniformity of the sample surface

		3.3.4 Coexistence of reconstructions
		3.3.5 LEED- $I(V)$ measurements
	3.4	Discussion
	3.5	Conclusion
4	_	$_{0.8}{ m Sr}_{0.2}{ m MnO}_3$ films on
	$\mathbf{SrT}$	$\mathrm{GiO}_{3}(001)$
	4.1	Introduction
	4.2	Structure and surface terminations
	4.3	Sample preparation and results
		4.3.1 $SrTiO_3(001)$ substrates
		4.3.2 Surface structures
		4.3.3 LSMO film growth
		4.3.4 Ar <sup>+</sup> sputtering
		4.3.5 MnO deposition and subsequent LSMO film growth 42
		4.3.6 LEED- $I(V)$ measurements
	4.4	Discussion
		4.4.1 Influence of the bulk structure on the $I(V)$ curves
	4.5	Conclusion
5	$\mathrm{Cu}_2$	$_{2}$ O(111)
	5.1	Introduction
	5.2	Bulk structure and surface terminations
	5.3	Sample preparation and results
		5.3.1 Characterization of the $(1 \times 1)$ and $(\sqrt{3} \times \sqrt{3})$ R30° surfaces 52
		5.3.2 Other effects observed during sample preparation 56
		5.3.3 LEED- $I(V)$ measurements 60
	5.4	Discussion
	5.5	Conclusion
6	Sun	nmary and outlook

# List of Figures

1.1	Classification of oxide surfaces by Tasker
1.2	Schematic illustration of Bragg-diffraction
1.3	2D Ewald sphere of a 3D structure
1.4	Bulk-truncated surface and surface reconstructions with their diffrac-
	tion patterns
1.5	Ewald sphere for diffraction on surfaces
1.6	Muffin-tin potential for calculating the scattering intensities
2.1	Picture of the UHV setup
2.2	Schematic representation of PLD
2.3	Schematic representation of an STM measurement setup 14
2.4	Topography vs electronic structure in STM
2.5	Experimental setup of an XPS measurement
2.6	LEED setup
2.7	Spot tracker in ImageJ
2.8	Sample mounting used for STM measurements
3.1	Exemplary cubic ABO <sub>3</sub> perovskite structure
3.2	Structure of $SrTiO_3$
3.3	Surface phase diagram of $SrTiO_3(110)$
3.4	$(4 \times 1)$ surface of $SrTiO_3(110)$
3.5	Characterization of the ${\rm SrTiO_3(110)}$ substrate after three sputtering—
	annealing cycles
3.6	LEED patterns after Sr deposition and $Ar^+$ sputtering
3.7	Diffraction patterns from LEED after Ar <sup>+</sup> sputtering
3.8	Coexistence of the $(4 \times 1)$ and $(5 \times 1)$ reconstructions
3.9	Coexistence of the $(4 \times 1)$ and $(2 \times 4)$ reconstructions
3.10	LEED- $I(V)$ curves of SrTiO <sub>3</sub> -(4 × 1) measured at different distances
	between the sample and the LEED screen
3.11	Spot tracking of the $(-3/4 1)$ spot at different energies 31

4.1	Bulk-truncated structure of $La_{0.8}Sr_{0.2}MnO_3$	36
4.2	Characterization of the surface of the $SrTiO_3(001)$ substrate	38
4.3	Characterization of the two distinct surfaces of LSMO(001)	39
4.4	Detailed view of the surface after LSMO film growth	40
4.5	LEED patterns and STM images of the surface after Ar <sup>+</sup> sputtering	41
4.6	STM images of the surfaces after film growth	42
4.7	Selected LEED- $I(V)$ curves and resulting $R_{\rm P}$ factors of the two dif-	
	ferently prepared $MnO_x$ surfaces	43
4.8	Energy dependence of the overall $R_{\rm P}$ factors	44
5.1	Structure model of $Cu_2O$	48
5.2	Models for the $(1 \times 1)$ periodicity and the $(\sqrt{3} \times \sqrt{3})$ R30° recon-	
	struction of $Cu_2O(111)$	49
5.3	Model of the $(\sqrt{3} \times \sqrt{3})$ R30° reconstruction of Cu <sub>2</sub> O(111) formed	
	by nanopyramids	49
5.4	Phase diagram of copper oxide	51
5.5	Characterization of the $(1 \times 1)$ -ordered $Cu_2O(111)$ surface	53
5.6	Characterization of the $(\sqrt{3} \times \sqrt{3})$ R30° reconstruction of Cu <sub>2</sub> O(111)	54
5.7	Mostly $(\sqrt{3} \times \sqrt{3})$ R30°-reconstructed surface	55
5.8	STM images of a different phase appearing on the $(1 \times 1)$ surface	
	after annealing at high oxygen partial pressures	57
5.9	Comparison of STM images of the $(\sqrt{3} \times \sqrt{3})$ R30° surface structure	
	obtained by different cooling rates	58
5.10	One-layer-deep vacancy islands after aprupt changes in the chemical	
	potential of oxygen $(\mu_{\mathrm{O}_2})$ between two subsequent annealing steps $% \left( 1\right) =\left( 1\right) \left( 1\right) $	59
5.11	Diffraction patterns and selected symmetry-equivalent diffraction spots	
	obtained from the LEED- $I(V)$ curves of the $(1 \times 1)$ and the $(\sqrt{3} \times \sqrt{3})$ I	R30°
	surface of $Cu_2O(111)$	61

#### 1.1 Metal-oxide surfaces

Metal oxides represent one of the most important material classes in today's world and are indispensable in modern technologies. Given that the majority of metals undergo oxidation in ambient conditions, they are of significant importance. Furthermore, they display an extraordinarily broad range of physical and chemical properties [1].

Of particular interest within the class of metal oxides are transition-metal oxides (TMOs), which show a remarkable diversity of functionalities. For instance, in the context of electrical conductivity, both insulators and superconductors fall within this class [2]. There are TMOs that exhibit piezo-, pyro-, and ferroelectricity and high dielectric permittivities [3]. By introducing defects, such as oxygen vacancies or interstitials into the crystal lattice, their physicochemical behavior can change significantly [4]. Due to their versatility, TMOs are ideal for applications in optoelectronic devices, corrosion protection, catalysis, and are widely used in energy technologies for energy production, conversion, storage, as well as emission control [5, 6].

The interaction between a material and its environment occurs via its surface. It is therefore crucial to gain an understanding of the atomic structures of surfaces, as it allows to understand and influence the ongoing processes and reactions. To this end, the so-called surface-science approach was pursued in this thesis. Here, single-crystalline materials with distinctive physical properties and precisely defined surfaces are investigated in an ultra-high vacuum (UHV) environment. The truncation of a crystal results in an interruption of the three-dimensional periodicity, which in turn gives rise to a rearrangement of the atoms at the surface into structures known as surface reconstructions. Metal oxides, in particular, exhibit a variety of complex surface reconstructions, which often depend on their cation or oxygen composition [7].

The contamination-free UHV environment along with the well-known atomic positions in single-crystals allow for a meaningful comparison with computational structure models.

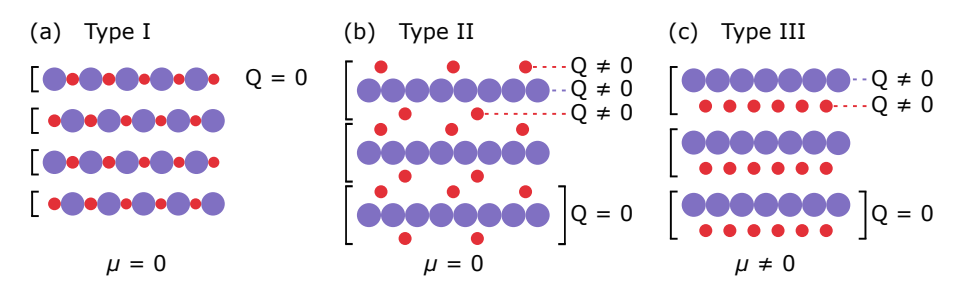


Figure 1.1: Classification of oxide surfaces by Tasker [8] into three types. Type I and Type II surfaces are stable due to their net dipole moment of 0. For Type III surfaces, a non-zero net dipole moment exists, rendering them unstable. Adapted from Ref. 9.

#### Stability of metal-oxide surfaces 1.1.1

Metal oxides are ionic compounds, which can be conceptualized as a structure composed of alternating planes of ions. Surfaces are created by truncating the bulk crystal along these planes. The atoms at the surface are rearranged to maintain electrostatic charge neutrality. In order to classify oxide surfaces based on electrostatic criteria alone, Tasker [8] provided a classification method comprising three types, which differ in their stacking sequence, displayed in Fig. 1.1. The repeat units are marked by the square brackets. Each layer contains a net charge Q. Repeat units composed of these layers are charge neutral, but may carry a dipole moment  $\mu$  depending on the relative arrangement of the layers. Type I surfaces [Fig. 1.1(a)] are charge neutral in the planes, with no dipole moment perpendicular to the surface. In Type II and Type III [Figs. 1.1(b) and 1.1(c), respectively], a non-zero net charge within the layers occurs. The stacking of Type II allows for the cancellation of the individual dipole moments, resulting in  $\mu = 0$ . Both Type I and Type II show stable bulk-truncated surfaces. A cancellation is not the case for Type III, which leads to a summation of the dipole moments and, further, to an infinite electrostatic energy. These surfaces are generally unstable in their bulk-truncated form. Nevertheless, they appear in nature through the stabilization of the surface via various mechanism, including surface reconstructions, adsorption of atoms or ions, or electron transfer [9].

#### 1.2Low-energy electron diffraction

Low-energy electron diffraction (LEED) is the most commonly used diffraction method in the field of surface science. The technique determines the symmetry of the surface structure by employing low-energy electrons in the 20–500 eV range, resulting in wavelengths from 1.7 to 0.5 Å. These wavelengths are slightly shorter



than typical interatomic distances, rendering them well suited for diffraction on atomic structures. In this energy range, the inelastic mean free path of electrons is only in the order of a few atomic layers, which makes LEED a very surface-sensitive method as the diffracted signal comes only from the topmost crystal layers. As the diffraction pattern produced is a mapping of reciprocal space, it is relatively straightforward to interpret qualitatively. Additionally, sources and detectors are readily available, making the technique easy to implement [10].

#### 1.2.1Periodic structures and diffraction

Diffraction is typically employed to investigate periodic structures. These can be described through the use of a lattice and a basis. The lattice can be visualized as a set of points and is defined by three translation vectors a, b, and c, also known as basis vectors. Every point of the lattice can be reached by multiplying the three translation vectors by integers (u, v, w), resulting in the lattice vector

$$\mathbf{R} = u\mathbf{a} + v\mathbf{b} + w\mathbf{c} . \tag{1.1}$$

The basis can consist of a single atom or a group of atoms and, together with the lattice, forms the crystal structure.

An incoming plane wave with wave vector k is scattered by a crystal only under specific conditions. These conditions are defined by the periodic structure of the crystal and are described by Bragg's law as

$$n\lambda = 2d\sin(\theta), \tag{1.2}$$

which relates the scattering angle  $\theta$  to a periodicity d of the crystal lattice, and the

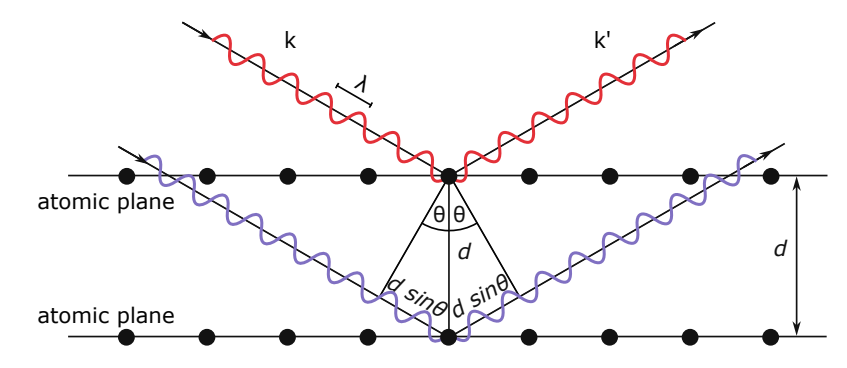


Figure 1.2: Schematic illustration of Bragg-diffraction. The phase difference of the incoming k and scattered waves k' must be a multiple integer of the wavelength  $\lambda$  for constructive interference. Reproduced from Ref 11.



wavelength  $\lambda$  of the incoming wave. In order to achieve constructive interference and, consequently, diffraction, the phase difference between the incoming and scattered beam must be a multiple integer of the wavelength, as seen in Fig. 1.2. Different lattice planes diffract waves at distinct angles, producing a diffraction pattern in which each spot corresponds to a specific family of lattice planes. [12].

The reciprocal space, also referred to as k space, is a mathematical construct in crystallography to describe diffraction patterns. For each translation vector  $\boldsymbol{a}$  there is a corresponding reciprocal vector  $a^*$ . Thus, there is a corresponding reciprocallattice vector G with each real-space vector R. Both  $a^*$  and G have units of inverse length. This inverse relationship implies that large unit cells in real space correspond to small unit cells in reciprocal space, and vice versa. The spatial arrangement of the diffracted beams is directly connected to the reciprocal lattice by the Laue condition. It states that the difference between the incoming and diffracted wave vectors must be a reciprocal-lattice vector G in order to fulfill the diffraction law. This condition can also be illustrated graphically via the Ewald sphere. Figure 1.3 displays the Ewald sphere in 2D, from a 3D structure. The **k** space is formed by a point lattice, and diffraction only occurs when the circle intersects at least two lattice points (bold line). The dashed line shows a case in which diffraction is not observed, as only one point (red circle) lies on the circle [13].

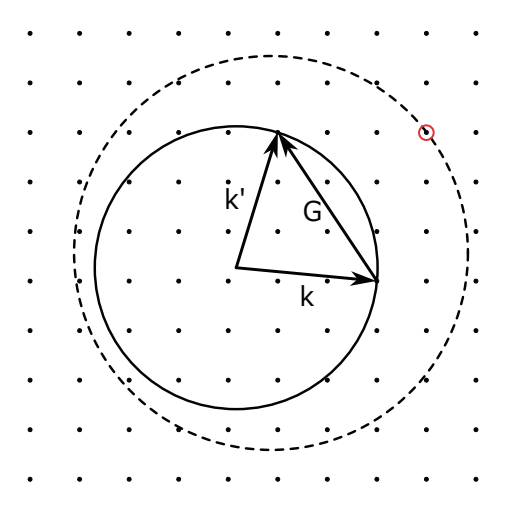


Figure 1.3: 2D Ewald sphere of a 3D structure. The incoming wave k is only diffracted by the crystal when k - k' = G. This is the case for circles that intersect at least two lattice points (solid line) and does not hold for k values with circles that only correlate with one lattice point (red circle and dashed line).



#### 1.2.2 Diffraction on surfaces

For crystal surfaces, the periodicity is broken in the out-of-plane direction. Therefore, only two translation vectors are present, which are often different from those of the corresponding 3D structure. For bulk-truncated surface structures that are energetically less favorable than a change in the atomic positions, a rearrangement occurs. This is often accompanied by a change in the surface periodicity, which is known as a surface reconstruction. The unit cells of reconstructed surfaces are larger than those of the truncated bulk, and described by their relation to the bulk unit cell. For this, the so-called Wood notation in the form of either  $(n \times m)$  or  $(n \times m)R\alpha^{\circ}$  is used. n and m indicate the scaling factor of the unit-cell vectors of the superlattice compared to those of the bulk cell, and  $R\alpha^{\circ}$  indicates that the superlattice is rotated by the angle  $\alpha$ . It is important to note that a given material can form several different surface reconstructions, depending on the preparation conditions employed. Figure 1.4 gives an example for the notation of superstructures (top row) and their corresponding diffraction patterns (bottom row). The bulk-truncated surface and its diffraction pattern is depicted in Fig. 1.4(a). In the diffraction pattern, the superstructure is visible as an additional set of spots, as

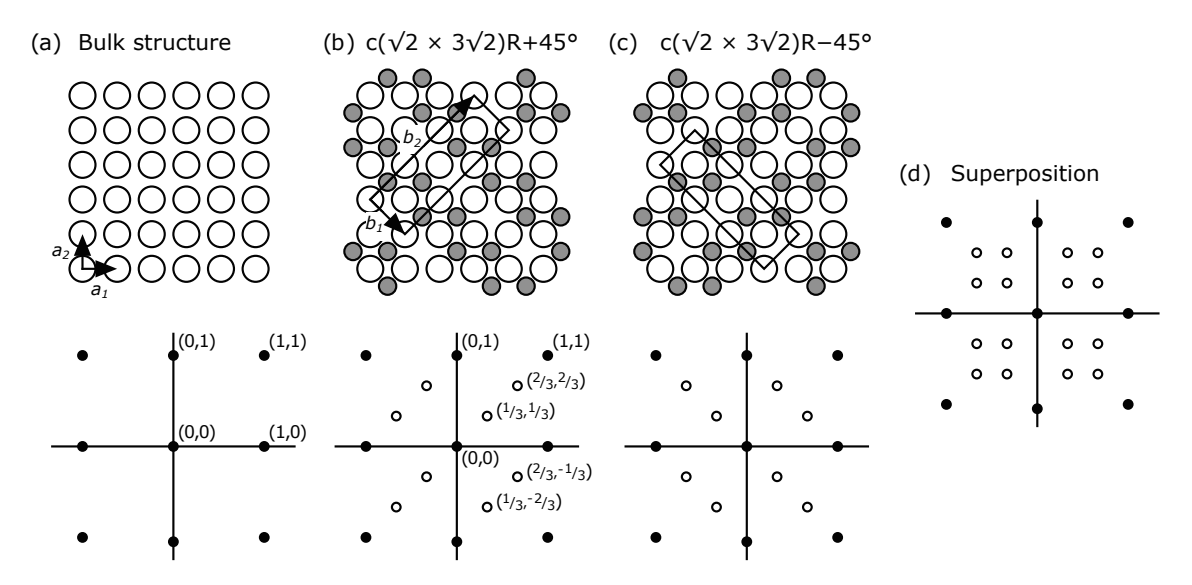


Figure 1.4: Bulk-truncated surface and surface reconstructions (top row) with their diffraction patterns (bottom row). (a) Bulk structure. (b), (c) Two rotational domains of the  $c(\sqrt{2} \times 3\sqrt{2})R45^{\circ}$  reconstruction. In the diffraction pattern, lattice spots are marked with solid circles, and reconstruction spots with open ones. The unit cell of the superlattice is  $\sqrt{2}$  times larger in  $a_1$  and  $3\sqrt{2}$  times larger in  $a_2$ , with the cell being rotated by  $\pm 45^{\circ}$ , respectively. The c indicates additional atoms in the center, which results in a c( $\sqrt{2} \times 3\sqrt{2}$ )R45° structure. (d) Superposition of the individual c( $\sqrt{2} \times 3\sqrt{2}$ )R45° diffraction patterns. Adapted from Ref. 14.

seen in the bottom row of Fig. 1.4. As the reconstructed cell is larger than the bulk one, it appears smaller in reciprocal space. According to the notation with Miller indices, the spots can have non-integer coefficients. When the unit cell of the reconstruction differs in symmetry from the bulk structure, the structure forms domains with different orientations. Figures 1.4(b) and 1.4(c) show two rotational domains of the  $c(\sqrt{2} \times 3\sqrt{2})R45^{\circ}$  reconstruction, where the 'c' indicates additional atoms in the center of the unit cell. Their unit cell is  $\sqrt{2}$  times larger in  $a_1$  and  $3\sqrt{2}$ times larger in  $a_2$ , and is rotated by  $+45^{\circ}$  or  $-45^{\circ}$ , respectively. If these domains are smaller than the diameter of the electron beam used in LEED (typically, 0.5-1 mm), the resulting diffraction pattern is a superposition of the diffraction patterns from each domain, as seen in Fig. 1.4(d) [15].

The reciprocal space of surfaces is a 2D array of points. In the third direction, perpendicular to the plane, it becomes an array of lattice rods or crystal-truncation rods. This means that the Ewald sphere (Fig. 1.5) intersects the rods at every energy, as long as  $|\mathbf{k}|$  is large enough, resulting in continuous diffraction patterns with varying energy. By changing the energy of the incoming electrons, the intensities along the rods can be measured, providing information about the third spatial direction (e.g., layer distances) [16].

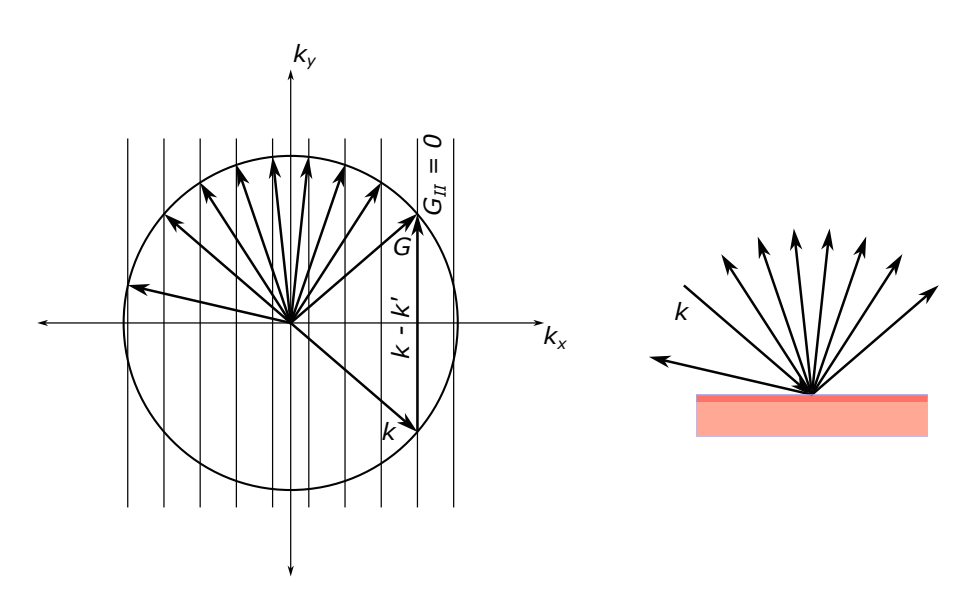


Figure 1.5: Ewald sphere for diffraction on surfaces. If  $|\mathbf{k}|$  is large enough, a diffraction pattern occurs for each energy. The diffraction geometry is shown in real space on the right. Reproduced from [14].

## Quantitative analysis — LEED I(V)

Besides extracting symmetry information from the surface, LEED can also provide quantitative information such as atomic positions and compositions [17]. To achieve this, the intensities of the diffracted spots are measured as a function of the energy of the incoming beam. This results in LEED-I(V) curves. The energy steps in the measurement are chosen to be small enough to obtain a quasi-continuous function [18].

In the context of single scattering (i.e., kinematic approximation), the intensity of the scattered beam is proportional to the square absolute value of the Fourier transform of a scattering strength f, resulting in

$$I(\mathbf{k}') \propto \left| \int f(\mathbf{r}) e^{i(\mathbf{k} - \mathbf{k}') \cdot \mathbf{r}} d^3 \mathbf{r} \right|^2.$$
 (1.3)

In case of diffraction using electrons, f is a function of the electrical potential. A back-transformation however is not possible because the measurement lacks phase information due to the squared value of the original wave. To determine the structure, the measured intensities must be compared with simulated models [19].

The intensities in the kinematic approach for a single layer of 2D points are independent of the energy. However, this approximation is not applicable to a stack of 2D layers, as the impact of multiple scattering between layers becomes In a multi-layer structure, electrons can be scattered not only by atoms in a single layer but also by atoms in adjacent layers, leading to dynamical scattering effects. These interactions cause the observed intensities to depend on

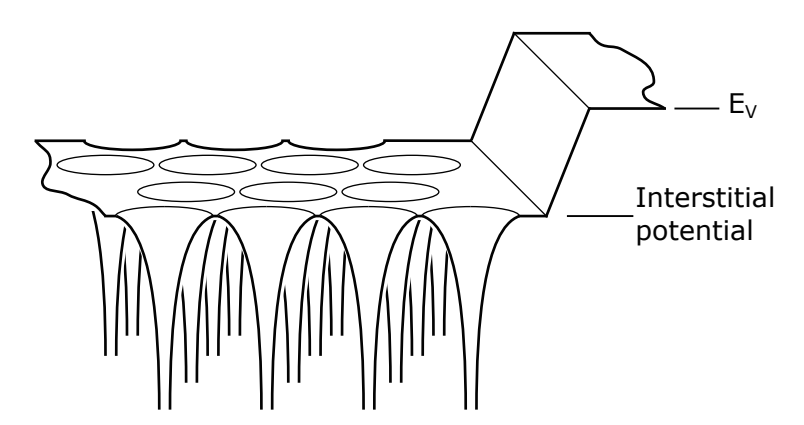


Figure 1.6: Muffin-tin potentials used for calculating the scattering intensities. The potential is spherically symmetrical around the atoms and constant in the regions between them. The shape of the potential step to the vacuum level is usually neglected. Reprinted from Ref. 14.



the electron energy, as the electron wavelength changes with energy, influencing the constructive and destructive interference between scattered waves from different layers. A multiple-scattering approach is necessary to account for these interactions. In order to calculate the scattering intensity, so-called muffin-tin potentials are used (Fig. 1.6). These potentials are spherically symmetric around the ion cores, with a common constant potentials assumed in between. In the majority of cases, the scattering at the occurring potential step to the vacuum level can be neglected. The constant potential between the atoms allows the calculation to utilize spherical waves, which are expanded into spherical harmonics after scattering. The scattering on each atom can then be described as a simple shift of the phase of each sphericalharmonic component of the electron wave. The atoms are then assembled into layers and multiple scattering within the layers is taken into account. The solid is constructed from these layers, taking into consideration multiple scattering between them.

The calculated I(V) curves are compared to the experimental data. In order to quantify the agreement between them, the so-called R factor (reliability factor) is utilized. There are several different factors, whereby the Pendry R factor (Ref. 20) is most commonly used. It is based on the quadratic deviation of  $d\ln I/dE$  of the experimental and calculated I(V) curves and is defined as

$$R_{\rm P} = \frac{\int (Y_{\rm exp} - Y_{\rm theor})^2 dE}{\int (Y_{\rm exp}^2 + Y_{\rm theor}^2) dE}, \qquad (1.4)$$

with

$$Y = \frac{L}{1 + (V_{0i} * L)^2}$$
, where  $L = \frac{d \ln I}{dE}$ , (1.5)

and  $V_{0i}$  is a constant. In an optimization procedure, structural parameters (e.g., atom positions, their vibration amplitudes, layer distances, etc.) are varied until the smallest  $R_{\rm P}$  factor is obtained. Eq. (1.4) leads to values of  $R_{\rm P}=0$  for perfect agreement of calculation and experiment,  $R_{\rm P} = 1$  for no correlation at all, and  $R_{\rm P} = 2$  for total anticorrelation. R factors of  $\leq 0.1$  are considered as an excellent correlation. For values between 0.2 and 0.3, the structure model may be correct, but one or more parameters do not fit the experimental data. A similar approach can be used to compare differently prepared sample structures, whereby LEED-I(V)can be employed as a 'fingerprint' technique to ascertain the structural identity.

Typically, an individual R factor is determined for each diffraction spot, and the overall R factor is calculated by sums over all beams in the numerator and



denominator in Eq. (1.4). As the definition of  $R_{\rm P}$  contains a derivative, the calculation is sensitive to noise in the experimental data. Therefore it is useful to average the individual I(V) curves by either repeating the experiment multiple times or averaging over symmetry-equivalent spots [18].

#### Outline of the thesis 1.3

This thesis addresses the preparation and characterization of three different TMO systems:  $SrTiO_3(110)$ ,  $La_{0.8}Sr_{0.2}MnO_3(001)$  [LSMO(001)], and  $Cu_2O(111)$ . These materials exhibit different surface reconstructions. The structural details of many of those reconstructions are still unknown. Consequently, LEED-I(V) measurements were conducted on one surface reconstruction of SrTiO<sub>3</sub>(110), and two surface phases of LSMO(001) and Cu<sub>2</sub>O(111), respectively. In this thesis, experimental LEED-I(V) curves of these five surfaces are reported. Work on computational structure models of these systems is currently underway, with which the experimental data will be compared to further elucidate the structural details of this surfaces.

During the experiments, a variety of techniques typically used in the field of surface science was employed. A detailed overview of the methods and the UHV apparatus can be found in Chapter 2. The focus of Chapters 3–5 is on the material systems under investigation, starting with  $SrTiO_3(110)$  in Chapter 3.  $SrTiO_3(110)$ exhibits a variety of surface reconstructions adjustable by the near-surface composition. Fine-tuning of the surface stoichiometry was done via molecular-beam epitaxy (MBE) and  $Ar^+$  sputtering, both followed by  $O_2$  annealing, which resulted in the  $(4 \times 1)$ -reconstructed surface. Chapter 4 deals with thin-film growth of LSMO on  $SrTiO_3(001)$  substrates using pulsed-laser deposition (PLD). The Chapter shows the sensitivity of thin films to the choice of PLD parameters during the deposition process. An incommensurate and a  $(\sqrt{2} \times \sqrt{2})$ R45° surface were prepared by PLD growth or MnO deposition, and Ar<sup>+</sup> sputtering, respectively. Cu<sub>2</sub>O(111) in Chapter 5 showcases the importance of the correct bulk composition in order to prepare the desired reconstruction. Two surface periodicities — a  $(1 \times 1)$  and a  $(\sqrt{3} \times \sqrt{3})$ R30° periodicity — were achieved by annealing at different temperatures and oxygen partial pressures. The preparation procedures were accompanied by scanning tunneling microscopy (STM) measurements. LEED-I(V) measurements on each of the five surfaces were performed. The results are presented and discussed at the end of the respective Chapters.

Finally, Chapter 6 gives a summary of the work and outlines future directions.



## 2. Experimental methods

#### 2.1 UHV setup

The experiments were performed in the UHV setup shown in Fig. 2.1. The setup consists of two main systems: the PLD chamber and the surface-science system. A detailed description of the laboratory is given in Ref. 21.

The PLD chamber consists of  $\mu$ -metal, ensuring the screening of external magnetic fields. After bakeout, the base pressure was  $1 \times 10^{-10}$  mbar. The chamber is combined with reflection high-energy electron diffraction (RHEED) to monitor growth rates in real time during deposition. However, the focus of this work is not on PLD growth, and therefore no RHEED measurements are reported in this thesis. It is equipped with a ultaviolet (UV) laser (KrF excimer laser) with a wavelength of 248 nm (Coherent COMPexPro 205F) for target ablation, where the energy can be adapted with an attenuator. Through an exit window, the laser energy can be measured for calibration. Up to five targets can be attached to a rotatable carousel. An infrared (IR) laser (DILAS, 980 nm) is used for heating, which hits the sample directly in the back through a hole in the sample plate. The temperature is

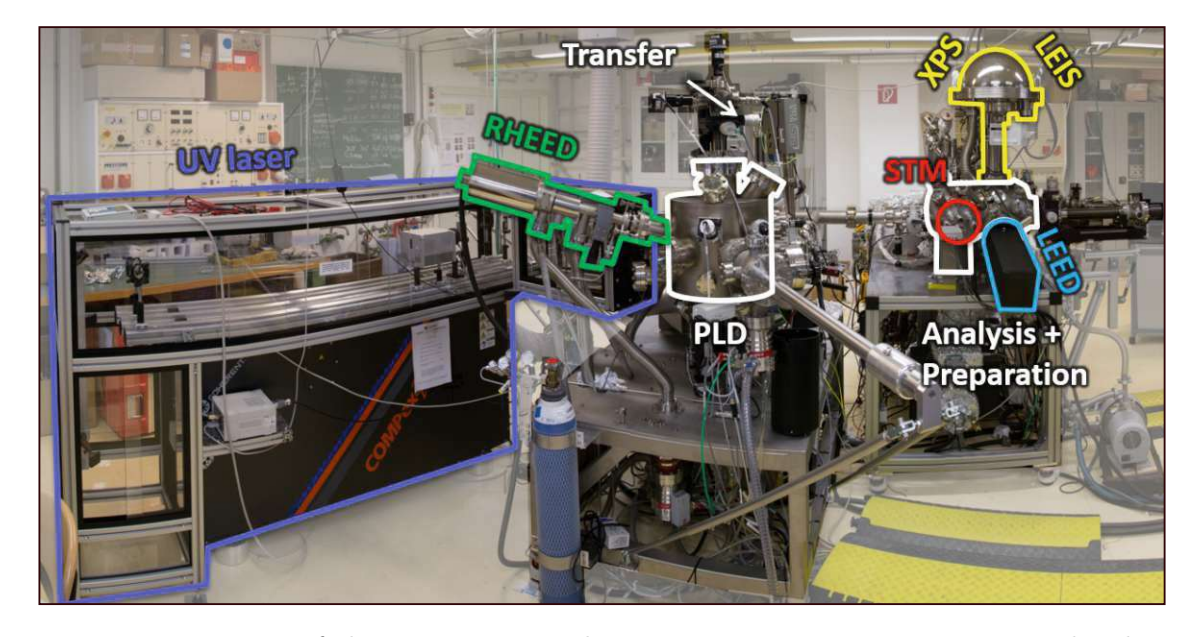


Figure 2.1: Picture of the UHV setup. The apparatus innterconnects a PLD chamber and a surface-science facility in UHV. Reprinted from Ref. 21.

measured from the front of the sample surface with a pyrometer [Impac IGS5] (MB20)]. Different gases (O<sub>2</sub>, N<sub>2</sub>, Ar) can be leaked into the chamber, while the flow is controlled via mass-flow controllers. Pressures up to 1 mbar can be achieved at temperatures up to 1200 °C [22].

The surface-science system is connected in UHV through a transfer chamber. The base pressure in both chambers was below  $5 \times 10^{-11}$  mbar. In the surfacescience system, samples are prepared and characterized in two different chambers: a preparation and an analysis chamber. Samples can be cleaned through Ar<sup>+</sup>sputtering cycles in the preparation chamber. The preparation chamber is also equipped with a molecular-beam epitaxy (MBE) system to deposit Sr in order to adjust the surface composition of SrTiO<sub>3</sub>. The deposition is performed from a low-temperature effusion cell held at 420 °C. Growth rates are calibrated by a homebuilt quartz-crystal microbalance (QCM). The analysis chamber is equipped with LEED, X-ray photoelectron spectroscopy (XPS), low-energy ion scattering (LEIS), and scanning tunneling microscopy (STM) for a complete characterization of the materials. Additionally, samples can be annealed with an electron-beam heater in both chambers.

#### 2.2PLD

PLD is a process of physical vapor deposition used for growth of thin films. It is both used for the synthesis of devices and for material studies [23]. Typically, a UV laser emits short pulses with pulse lengths on the range of nanoseconds, and is focused on a target. The high energy density of the laser ablates target material. The material is ejected from the target in a plasma plume and deposited on the substrate, which can be heated to enhance diffusion and surface mobility. The process is schematically illustrated in Fig. 2.2.

This method of film growth has several characteristics that make it particularly attractive for complex materials like TMOs. For example, it enables the transfer of the target stoichiometry to the substrate, given that the PLD parameters are chosen correctly. The deposition of multication films can be realised with multiple targets for each element or with a single stoichiometric target of the required material system. The targets are polycrystalline and therefore readily produced.

Typically, one laser pulse deposits a sub-monolayer amount of material. This allows for the precise control of the film thickness by adjusting the number of pulses. However, the quality and properties of the resulting film are dependent on multiple parameters throughout the growing procedure.

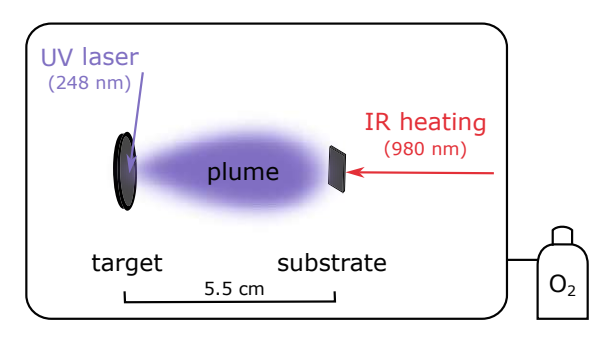


Figure 2.2: Schematic representation of PLD. The UV laser hits the target and ablates material. A plasma plume is created and ejected forward-directed to the substrate. The material is deposited on the sample while heated with an IR laser. Adapted from Ref. 21.

An oxygen-gas background both participates actively in the chemistry of the film and slows down the ejected material. For oxides, multication thin films often need a reactive species as a component in the plume [24]. By adjusting the oxygen partial pressure, the kinetic energy of the ablated material species is changed via scattering processes, which influences directly their mean free path and thus the properties of the film [25]. This interaction can be divided roughly into three different pressure regimes. At low pressures, the mean free path of the ejected material is larger than the distance between the target and the substrate. The composition of the plume and the one ablated from the target are the same. Within an intermediate regime, the interaction of the plasma species and the oxygen molecules depends on their mass: With higher pressures the film is enriched with the heavier plume species, as they get scattered less than the lighter ones. Very high pressures result again in a congruent transfer of the ablated material. The regime is called the shock-wave regime, where all species are slowed down equally [26]. However, the composition of the plume is not necessarily the same as the one of the target: it is affected by the energy density (also referred to as fluence) of the ablating laser. The target-to-substrate distance (55 mm in the used setup) plays a significant role in the classification of the three regimes [27].

Besides the oxygen background, several other parameters like the laser pulse energy and duration, the pulse-to-pulse standard deviation, the energy density, the repetition rate, the beam divergence, the target selection, and the condition of the surface, have a huge impact on the film properties and homogeneity [24, 28].

## Experimental setup

PLD was used to grow LSMO films on SrTiO<sub>3</sub>(001) substrates. The experimental setup was already discussed in Section 2.1. Home-prepared LSMO and MnO targets were used for PLD [29]. Before film growth, the targets were preablated using the same parameters as those employed in the growth process, except with higher repetition rates. Preablation ensures a clean target surface prior to film growth. During preablation, the substrate was kept in a separate UHV chamber to avoid deposition of unwanted material [22]. During the ablation procedure with the UV laser, the targets are moved in a raster pattern. This approach ensures that the ablated area is sufficiently large to prevent the formation of holes and enabling a uniform ablation throughout the process.

### 2.3 Scanning-probe microscopy

#### 2.3.1STM

In STM, the sample is probed with an atomically sharp metal tip, usually made out of tungsten or Pt-Ir, to image the surface at an atomically resolved level. This is achieved by bringing the tip extremely close to the sample (within nanometer range), until a tunneling current is observed. Consequently, the material selection is restricted to electrical conductors or semiconductors. The fine adjustment of the tip movement is achieved by piezoelectric elements. Typical operating parameters for a STM measurement are 0.1–40 nA in current, and around  $\pm 1$  mV to  $\pm 5$  V applied voltage [30]. Figure 2.3 shows a schematic setup for STM measurements.

From the time-separated Schrödinger equation applied on a rectangular potential barrier, an approximation of the dependence of the wave function  $\psi$  on the distance d can be derived. The tunneling current is then proportional to the transmission probability T, as

$$I \propto T \propto |\psi(d)|^2 \propto e^{-2\kappa d}$$
. (2.1)

Since d appears in the exponent of Eq. (2.1), the current drops rapidly with increasing distance. A change in distance of 1 Å results in a current change up to an order of magnitude. This makes resolutions in the picometer range possible.

Imaging can be performed in two different modes: constant-height mode, which keeps the tip at the same height while scanning over the surface and measuring the

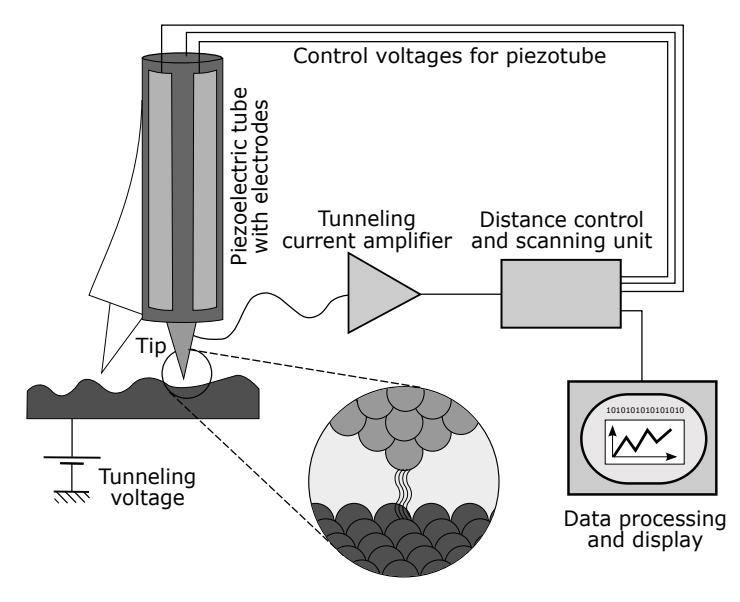


Figure 2.3: Schematic representation of an STM measurement setup. Reprinted from Ref. [31].

varying current, and constant-current mode. Usually, the latter is used, as the risk of crashing the tip at protrusions from the surface is quite high in constant-height mode. In constant-current mode, the vertical position of the tip is continuously adjusted by a feedback loop to maintain a constant current flow. The monitored displacement of the tip results in an image of constant local density of states (LDOS), which means that the measurement is not necessarily a depiction of the surface topography but also contains electronic information [32]. In Fig. 2.4(a), the structure model of TiO<sub>2</sub> is shown as an example. The O atoms are geometrically higher than the Ti atoms. The LDOS calculation depicts an opposite behavior, as seen in Fig. 2.4(b), which leads to an inversion of the contrast in the STM images when a positive bias voltage is applied between the tip and the sample [Fig. 2.4(c)]. The Ti atoms and O vacancies appear brighter, as the tunneling current is higher than that occurring for the O atoms. Consequently, the appearance of the O atoms is dark.

## Experimental setup

STM was utilized for the characterization of surface structures, with positive sample bias voltage (measuring empty states) in constant-current mode. The employed tip is made out of tungsten and permanently integrated in the system. Ideally, the tip consists of a single atom, as blunt tips lead to bad resolution. In the case of tips consisting of two or more atoms, the surface features are multiplied. A tip

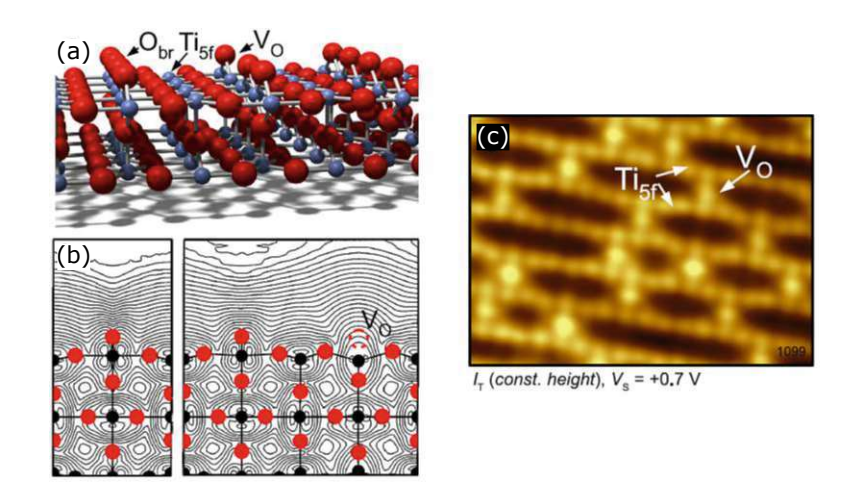


Figure 2.4: Topography vs electronic structure in STM. (a) Structure model and topography of a TiO<sub>2</sub>(110) surface. The O atoms protrude above the Ti atoms. (b) Graphical representation of the calculated LDOS of TiO<sub>2</sub>. (c) The Ti atoms and O vacancies appear brighter than the O atoms, given that the tunneling current is lower for the O atoms when a positive bias voltage is applied to the sample. Adapted from Ref. 14.

replacement in the UHV chamber used is only possible by venting it. To avoid this, two different methods for tip preparation were applied. Ar<sup>+</sup> sputtering for about one hour, with an ion current around 1.5  $\mu$ A, an Ar partial pressure of  $5 \times 10^{-6}$  mbar, and an acceleration voltage of 3 kV. Alternatively, the tip can be reshaped by applying voltage pulses up to  $\pm 10 \,\mathrm{V}$  while in tunneling contact. The pulse can either eject atoms or molecules or deposit them, both resulting in a sharper tip [33].

#### 2.3.2 **AFM**

Atomic-force microscopy (AFM), like STM, is a scanning-probe microscopy technique. A sharp tip, positioned on a cantilever, scans the sample in a raster pattern and interacts with it. The interaction forces are measured by recording the deflection of a laser reflected by the cantilever with a position-sensitive photodiode. The method needs minimal sample preparation and can also be performed on nonconductive materials.

The measurement with AFM can be carried out in different modes. In tapping mode, the cantilever is driven to oscillate near its resonance frequency, while the oscillation amplitude is measured. The interaction between the tip and the sample alters the resonant frequency depending on the surface topography. A feedback loop maintains the cantilever at a constant oscillation frequency, transforming the information into a height profile [34–36].



## Experimental setup

The measurements were performed in an ambient-pressure AFM in tapping mode. It was used to check the cleanliness of the samples and substrates before introducing them into the UHV chamber.

#### **XPS** 2.4

XPS is a characterization technique in surface science for chemical analysis. It is based on the photolectric effect. Photons emitted from an x-ray source interact with the sample, where electrons are excited and subsequently ejected from the surface with a characteristic energy. The emitted electrons and their kinetic energy, which is dependent on the source energy, are measured through an analyzer. From the known photon energy, the original binding energy of the emitted electrons can be calculated [37]. A drawing of the experimental setup with the interactions between an atom and the incident photon can be seen in Fig. 2.5.

Since x-ray photons have an absorption length in the micrometer range, the surface sensitivity of the method comes from the scattering behavior of the electrons with matter. The IMFP of electrons in the measured energy range (0–1400 eV) is in the nanometer range, meaning that the signal originates from a few atomic layers close to the surface.

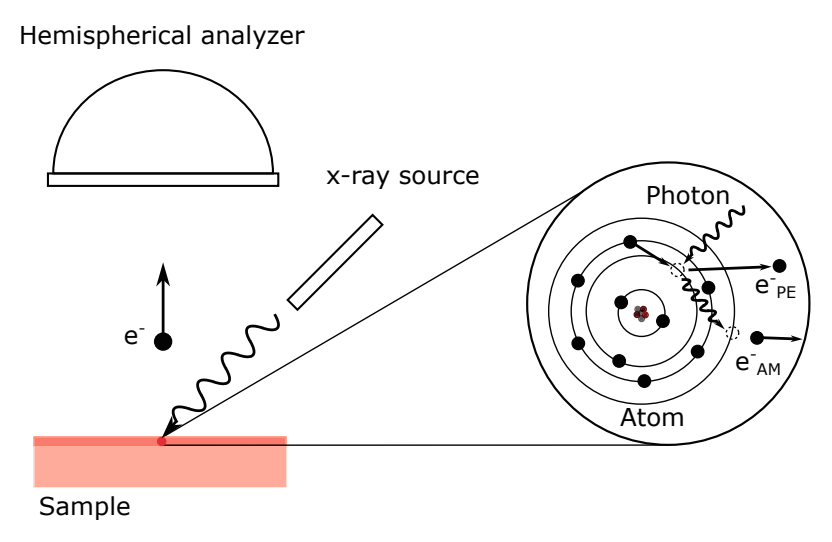


Figure 2.5: Experimental setup of an XPS measurement. The enlarged region shows a drawing of the interactions between a photon and an electron. An incoming photon can either create a photoelectron (PE) by knocking an electron out of its initial state or an Auger-Meitner electron (AM). The latter results from an outer-shell electron filling the vacancy, with the released energy from this process ejecting a third electron.

The peak position in a spectrum provides qualitative information about the chemical composition of the sample. It can vary by a few electronvolts, depending on the chemical environment in which the elements are located, such as their oxidation state. A quantitative analysis is not straightforward since the peak intensities are not only a function of the element concentration but also of parameters like the photoelectric cross section, and photon flux, and the (usually unknown) spatial distribution of the emitting atoms [38]. The incident photons create another electron species, while interacting with the solid: the Auger–Meitner electrons. Auger-Meitner electrons are produced when an electron is knocked out of a shell, and the excited ion relaxes to the ground state. The released energy ejects another electron, which is then detected. The energy of an Auger-Meitner electron is independent of the incoming radiation energy [39]. In the recorded spectra, the peaks resulting from photoelectrons are sharp and high in intensity. Conversely, the Auger-Meitner peaks are typically broader in width, due to the very short lifetime of the intermediate excited state, and low in intensity [40].

## Experimental setup

The XPS used for investigations is equipped with non-monochromated Al  $K_{\alpha}$  and Mg  $K_{\alpha}$  sources with excitation energies of 1486.6 eV and 1253.6 eV, respectively. The spectra were recorded by measuring the photoelectron energies with a hemispherical analyser. Most of the experiments were performed with the Al source.

#### 2.5 $\mathbf{LEED}$

A theoretical description of LEED was already given in Section 1.2 in detail.

A LEED setup consist of the following parts: an electron gun, a retarding grid, and a detection screen. The retarding grid filters out the incoming electrons that were scattered inelastically by applying a voltage so that only elastically scattered electrons with the incident energy can pass and arrive at the detector. For detection, phosphor screens are used, which reproduce the diffraction pattern via photoluminescence. In Fig. 2.6, a typical LEED setup is shown. After sorting out the inelastically scattered electrons, the remaining electron signal is amplified. One common method for this amplification is the use of microchannel plates (MCPs), where numerous channeltrons are connected in parallel [37].



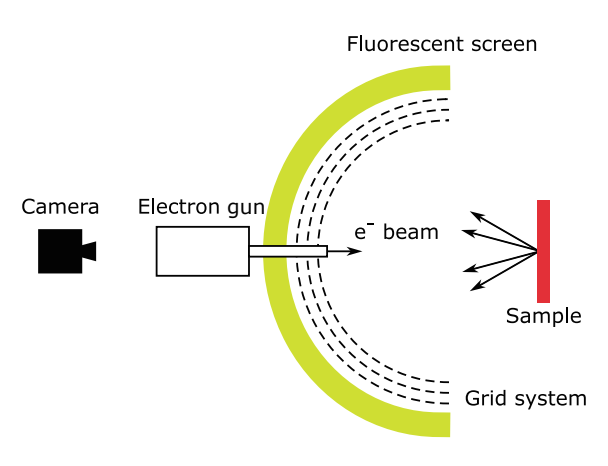


Figure 2.6: LEED setup. The camera is positioned outside the UHV chamber and records the diffraction pattern from the backside of the fluorescent screen (reverse-view LEED).

## Experimental setup

Unlike the PLD chamber, the LEED setup in which the data was recorded is not situated in a UHV chamber consisting of  $\mu$ -metal. Consequently, magnetic fields generated by external sources, such as public transportation close to the laboratory, are not shielded, which can have a significant impact on the measurements by deflecting the electrons on their way from and to the screen. To compensate for this, two coils were installed generating magnetic fields that counteract this disruption. Additionally, the setup has been upgraded with ViPErLEED (Vienna Package for Erlangen LEED) electronics [41] to enable fully automated LEED-I(V)measurements.

While measurements can be conducted in the energy range between 20 eV and 1000 eV, the investigated diffraction patterns were within the range of 25 eV to 150 eV. The diameter of the electron beam is about 0.7 mm. For each image at a certain energy, a flat-field image acquired by shining the electron beam onto the polycrystalline sample plate is taken to record a uniform distribution of the intensity without the spots. In addition, a dark frame at zero screen voltage ensures that the contribution of the surrounding light sources to the intensity is corrected. These data were used for background correction [42]. Additionally, a pincushion distortion correction has been applied. The pincushion distortion arises from the projection of scattered electrons onto a flat screen, while their scattering geometry is in fact spherical. This geometric mismatch causes the diffraction spots at larger scattering angles to appear farther apart than they should, creating a 'pushed-out' effect at the edges of the LEED pattern [37]. All post-processing steps were performed with ImageJ, a public-domain image-processing program with implemented plugins [43].

## The LEED-I(V) measurement

The LEED-I(V) measurements were implemented with the ViPErLEED package [43, 44], while the usual LEED setup was used.

For each measurement, an energy calibration was carried out. This ensures that the energy set by the controller is actually the energy that arrives at the sample, as almost all LEED optics are affected by an energy offset or a gain miscalibration. The difference can be corrected by comparing the nominal and the output energies. The relation provides a linear correction function to compensate for this error.

The measurement procedure follows the same principle as that of the standard LEED. For each recorded I(V) image stack, corresponding flat-field and a darkframe 'movies' were recorded. 3-5 measurements at different distances from the screen were performed. The collected data was averaged afterwards to eliminate contributions from the grid, and for noise cancellation [43].

In order to obtain good results, it is important to precisely adjust the incidence angle of the beam relative to the sample surface. This is because the measured (and calculated) I(V) curves depend strongly on the exact incidence angle of the electron beam. The manipulator of the analysis chamber only allows for the adjustment of two of the three spatial angles. Consequently, these two angles need to be adjusted as precisely as possible, while the third direction needs to be varied during the calculations. Energy ranges between 20 eV and 720 eV were used.

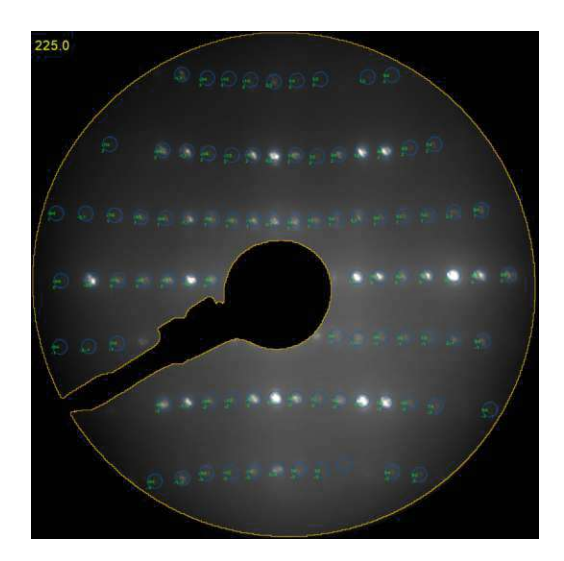


Figure 2.7: Spot-tracker tool implemented in ImageJ, shown for the LEED measurements on the  $(4 \times 1)$ -reconstructed surface of SrTiO<sub>3</sub>(110). By providing a pattern file which contains the symmetry information of the measured structure, the tool recognises the correct diffraction spots and follows them over the entire energy range. The energy is extracted and the data is converted into an I(V) curve.

Data was evaluated with the ViPErLEED analysis package in ImageJ [43]. A spot tracker follows the diffraction spots over the measured energy range and extracts their intensities. This is possible by providing a structure file, which contains the symmetry information of the examined surface with the occurring diffraction spots. Figure 2.7 depicts an example tracking the spots of the  $(4 \times 1)$  reconstruction of  $SrTiO_3(110)$  at 225 eV.

### Ex-situ preparation 2.6

The samples were cleaned before introducing them into the UHV chamber, and were characterized via an ambient-pressure AFM. After that, depending on the characterization methods needed in UHV, the samples were mounted with two different strategies, as explained in Section 2.6.2.

#### Sample cleaning 2.6.1

To remove polishing residues, all samples and substrates were cleaned using the same procedure. Round-bottom flasks, which were boiled in 20% HNO<sub>3</sub>, were utilized as glassware. The samples were first sonicated in isopropanol and ethanol for 30 min each. This was followed by sonication in 3% Extran for 30 min, and then in ultrapure water for 20 min. The last two steps were repeated until the samples were free of obvious contamination in a  $6 \times 6 \text{ }\mu\text{m}^2$  AFM image. After each step, the samples were rinsed thoroughly with ultrapure water. During the sonication process, the solvents were additionally warmed ( $\approx 60$  °C) in the sonication bath.

#### 2.6.2Sample mounting

All samples were mounted on sample plates that feature a hole for direct heating with the IR laser and a pocket for securing the sample. The sample is fixed on the plate with different clip designs via spot welding. Both plate and sample are made of Nicrofer<sup>®</sup>, an alloy consisting mainly of nickel, chromium, and iron, with suitable properties for high temperatures and oxygen pressures. Before use, the sample plates and clips were cleaned by boiling in 20% HNO<sub>3</sub> and then rinsing with ultrapure water.

Two different mounting strategies were used during the experiments. A loose mounting was chosen for samples not intended for STM measurements. In this case, a 0.17 mm-thick Nicrofer® foil was cut into thin stripes and diagonally spot welded on two opposing corners of the plate. No direct force is applied from the clips to

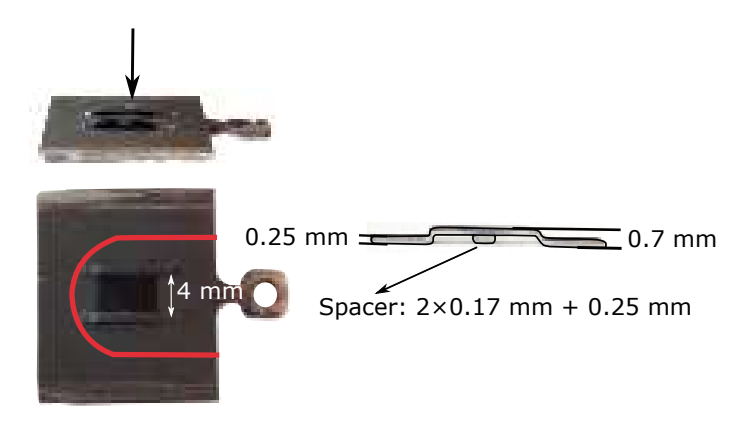


Figure 2.8: Sample mounting used for STM measurements. The clips are made out of a spacer (indicated by the black arrow) and a stripe composed of Nicrofer<sup>®</sup>. The red line marks the area where the clips need to be placed to fit in the STM holder. Adapted from Ref. 21.

the sample. This limits stress induced by the clips and helps preventing sample cracking during heating.

Samples for STM measurements require a more rigid mounting to minimize vibrations while scanning. Special clips with a spacer in the middle, consisting of three Nicrofer® stripes spot welded together, were utilized. The spacer is spot welded onto a stripe and formed with a home-designed tool. The shape and geometry of the clips is shown in Fig. 2.8. The red line highlights the requisite placement to fit the STM holder. As the sample protrudes by 0.25 mm from the sample plate, the spacer exerts pressure on the sample, potentially elevating the risk of cracking during the first annealing step. Nevertheless, this mounting approach remains the best solution for the intended application.

# $SrTiO_3(110)$ : The $(4 \times 1)$ 3. construction

#### 3.1 Introduction

For decades now, SrTiO<sub>3</sub> has been a highly relevant topic in surface science, with many surface structures still remaining unsolved [45, 46]. This TMO finds application in oxide electronics such as high-density data-storage devices as well as catalysis and photocatalysis [47, 48]. It is a favored substrate material for film growth of other perovskite oxides due to their good lattice mismatch with each other [49, 50]. For thin-film growth, well-defined substrate surfaces are required to control the deposition process, which makes it crucial to understand the surface structure [51]. The same holds for catalytic and photocatalytic processes, where the surface morphology plays a major role during the reactions. SrTiO<sub>3</sub> represents a prototype perovskite oxide with particularly interesting material properties. For example, transitions from metallic, to insulating, to even superconducting behavior can be realized through field effect and chemical doping with oxygen [52, 53]. At interfaces with other oxides, as well as directly on the SrTiO<sub>3</sub> surface, a 2D electron gas can form, potentially offering an alternative to conventional semiconductor devices [54].

The focus of this Chapter lies on the (110) surface of the perovskite oxide SrTiO<sub>3</sub>, more specifically the  $(4 \times 1)$  reconstruction of the (110) surface. SrTiO<sub>3</sub> exhibits a large number of surface reconstructions, which can be influenced by slight changes of the near-surface composition. For that, molecular beam epitaxy (MBE) from a lowtemperature effusion cell and Ar<sup>+</sup> sputtering, both followed by a high-temperature  $O_2$  annealing, were used. The surface stochiometry is extremely sensitive to small deviations from the ideal preparation conditions, resulting in a coexistence of the individual reconstructions, a known phenomenon for SrTiO<sub>3</sub> surfaces. A detailed overview of the preparation conditions and the following results is provided in Sections 3.3.2-3.3.4. The postprocessing of the recorded LEED-I(V) measurement on the  $(4 \times 1)$  reconstruction of SrTiO<sub>3</sub>(110) is presented in Section 3.3.5, followed by a discussion of the results in Section 3.4.

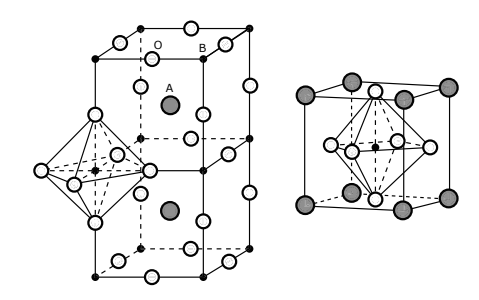


Figure 3.1: Exemplary cubic ABO<sub>3</sub> perovskite structure. Reprinted from Ref. 21.

#### Perovskite oxides 3.1.1

Perovskite oxides are a class of functional materials generally described by the formula ABO<sub>3</sub>. The cations at the A and B sites can be varied and partially substituted in a multitude of combinations, which significantly impacts the properties and allows considerable flexibility in material design [55, 56]. The unit cell is cubic with A-site cations at the corners, and B-site cations in the center, which is sixfold coordinated by oxygen. The structure is represented in Fig. 3.1. A-site cations have larger ionic radii than B-site ones and are typically alkaline-earth or rare-earth metals, whereas the B cations are transition metals [57].

#### 3.2 Structure and surface reconstructions

Figure 3.2(a) displays the cubic-perovskite structure of SrTiO<sub>3</sub> with a lattice constant of a = 3.905 Å. In this perovskite, the Sr atoms occupy the corners of the unit cell (A site), with a Ti atom located in the center (B site), octahedrally coordinated by O atoms. Figure 3.2(b) shows the (110) bulk-truncated surface in side view. Along the [110] direction, the crystal consists of alternating (SrTiO)<sup>4+</sup> and  $(O_2)^{4-}$  planes. This stacking results in an infinitely high electrostatic potential of the (110) bulk-truncated model and thus to an inherently unstable polar surface (Tasker Type III, see Section 1.1.1). The polarity is compensated by a  $TiO_x$ -richreconstructed overlayer on a (SrTiO)<sup>4+</sup> plane [58].

As mentioned above, SrTiO<sub>3</sub> shows a great diversity of reconstructions depending on its near-surface stoichiometry. To describe them, a  $(n \times m)$  notation is used, where n is the number of bulk unit cells in the [001] direction, and m the number in the [110] direction of the superstructure. In Fig. 3.3, a phase diagram of selected occurring structures with varying Sr or Ti content, respectively, can be seen [21]. The unit cells in the STM images are marked in white and the bulkderived diffraction spots of the respective LEED patterns underneath are marked

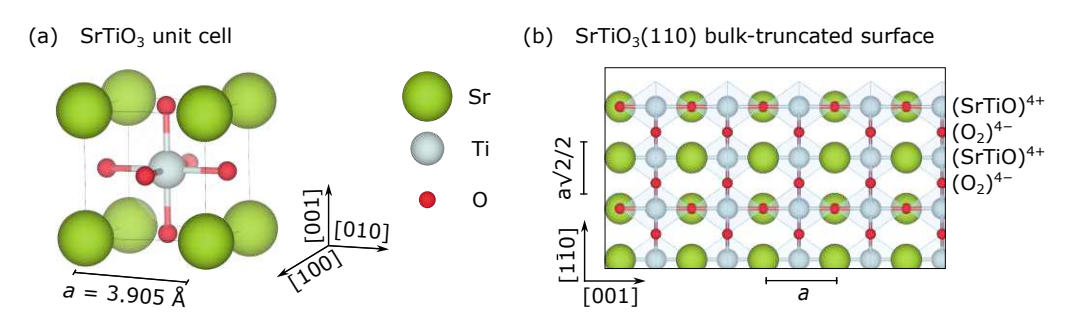


Figure 3.2: Structure of SrTiO<sub>3</sub>. (a) Perspective view of the cubic unit cell with lattice constant a = 3.905 Å. (b) Bulk-truncated model of the (110) surface structure in side view. Along the [110] direction the crystal has a stacking of alternating (SrTiO)<sup>4+</sup> and  $(O_2)^{4-}$ , resulting in a polar surface, which is unstable.

with red circles. On the Sr-rich side, the surface exhibits  $(n \times 1)$  reconstructions, all of them very similar in structure. This can lead to coexisting reconstructions at the surface, where different  $(n \times 1)$ -reconstructed lines appear side by side. The  $(n \times m)$  terminations are found on the Ti-rich side and are not related in their structure [59]. However, as the surface is highly sensitive to local deviations, multiple reconstructions can coexist at the macroscopic scale, for example in the case of non-uniform deposition. With increasing density of the  $TiO_x$ -rich overlayer, a transformation from the  $(n \times 1)$  series to the  $(n \times m)$  series takes place, where the Ti atoms change their coordination from tetrahedral to octahedral [60].

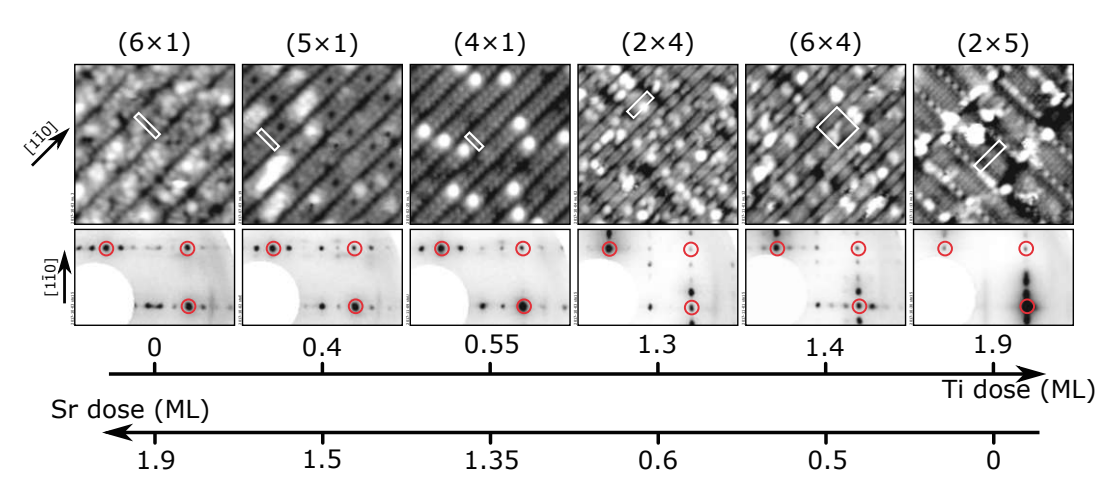


Figure 3.3: Surface phase diagram of SrTiO<sub>3</sub>(110) showing selected reconstructions depending on their relative Sr or Ti content, respectively. The  $(n \times 1)$  series is considered as more Sr-rich than the  $(n \times m)$  series. The unit cells are highlighted by white rectangles in the STM images, and the bulk-derived diffraction spots of the corresponding LEED patterns by red circles. One monolayer (ML) is defined as the density of cation sites in a bulk-truncated  $SrTiO_3(110)$  plane, amounting to  $4.64 \times 10^{14}$  atoms/cm<sup>2</sup>. Reprinted from Ref. 21.

#### 3.2.1 The $(4 \times 1)$ reconstruction

The  $(4 \times 1)$  reconstruction is the most commonly observed surface reconstruction of SrTiO<sub>3</sub>(110). It is formed by a network of TiO<sub>4</sub> tetrahedra on top of the last (SrTiO)<sup>4+</sup> layer. By sharing oxygen corners, the structure is built up through rings consisting of six or ten tetrahedra. From the STM image in Fig. 3.4(a), one can see that the reconstruction appears as lines following the  $[1\overline{1}0]$  direction separated by dark trenches. The unit cell is outlined by the white rectangle. Figure 3.4(b) represents a DFT model of the six- or ten-membered titania rings on the (110) surface. Since the mirror symmetry of the reconstructed surface unit cell is lower than that of the bulk-truncated one, two domains are present at the surface. When the two domains meet, an antiphase domain boundary develops, which can either result in a  $\mathrm{Sr}^{2+}$  adatom (orange) or a  $(\mathrm{Ti_2O_3})^{2+}$  vacancy (violet), depending on how they are oriented when combined. The so-called 'C-type' is observed when the wings of the 'boomerangs' point away from each other [marked in violet in Fig. 3.4(a)] and the 'W-type' boundary for 'boomerangs' pointing towards each other [marked in orange in Fig. 3.4(b)] [61]. In the DFT model [Fig. 3.4(b)], the 'W-type' antiphase domain boundary is shown with a white star representing a Sr<sup>2+</sup> adatom. A domain consisting of eight surface unit cells is highlighted in white  $(4 \times l \text{ with } l = 8)$ . In Fig. 3.4(c), a LEED pattern of the  $(4 \times 1)$  reconstruction is shown. As the distribution of the antiphase domain boundaries is not random,

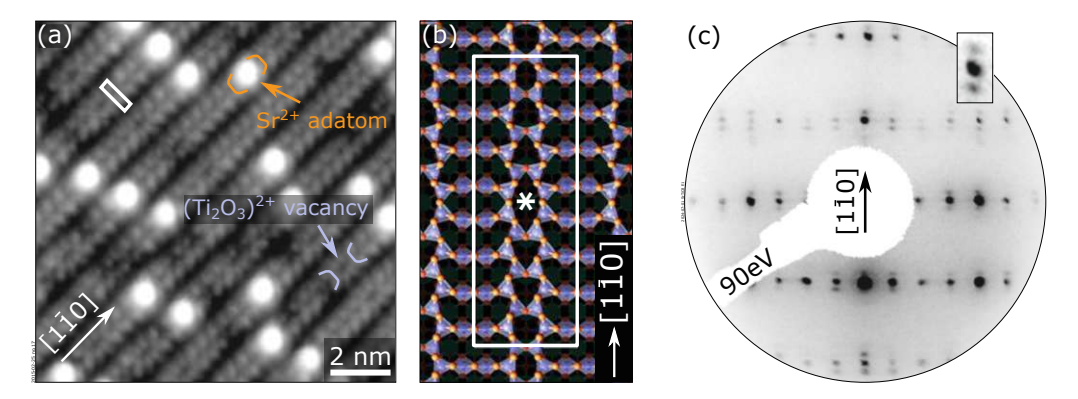


Figure 3.4:  $(4 \times 1)$  surface of SrTiO<sub>3</sub>(110). (a) Atomically resolved STM image with the unit cell marked in white. A symmetry break from the superstructure referred to the bulk-truncated surface leads to antiphase domain boundaries, which result in either  $Sr^{2+}$  adatoms (orange) or  $(Ti_2O_3)^{2+}$  vacancies (violet). (b) DFT model of the surface reconstruction consisting of six- or ten-membered corner-sharing TiO<sub>4</sub> tetrahedra. The white rectangle highlights a domain consisting of eight unit cells. (c) LEED pattern at 90 eV. The antiphase domain boundaries have a certain periodicity, which causes a splitting of the diffraction spots. Panels (a) and (b) are reprinted from Ref. 21.

their occurrence gives rise to an additional periodicity on the surface. This results in a splitting of the diffraction spots.

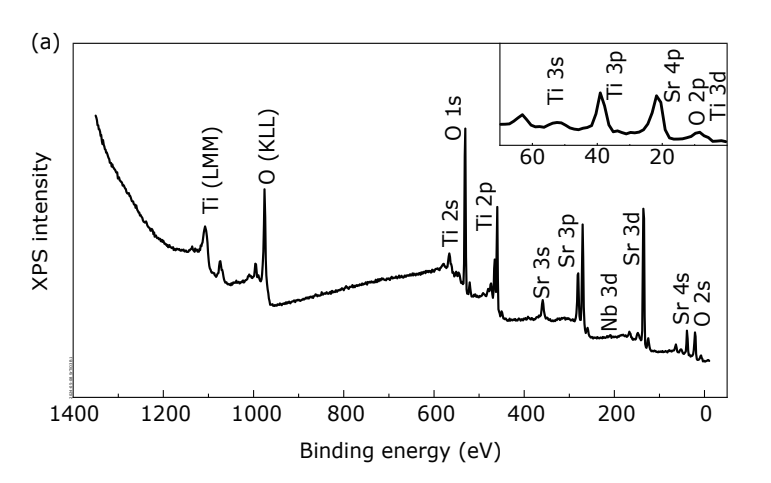
#### 3.3 Sample preparation and characterization

Each annealing step throughout the *in-situ* cleaning and preparation was carried out at 1000 °C and an oxygen partial pressure  $p_{\rm O_2}$  of 6  $\times$  10<sup>-6</sup> mbar with ramp rates in the 10–30 °C/min range, with a typical duration of 1 h.

#### 3.3.1 $SrTiO_3(110)$ substrates

 $5 \times 5 \times 0.5 \text{ mm}^3$  Nb-doped SrTiO<sub>3</sub>(110) single crystals, with a miscut of less than 0.2° (CrysTec GmbH) were utilized as substrates. The substrates were cleaned, analyzed with AFM, and mounted for STM in accordance with the procedures outlined in Section 2.6.

After introduction into the vacuum chamber, a test annealing was performed to check the mounting. Samples prepared for STM measurements tend to crack if the attachment of the clips is too tight. However, annealing at such high temperatures can also loosen the clips, making STM measurements challenging or even impossible due to vibrations. For surviving samples, this step was followed by sputtering-annealing cycles, with an  $Ar^+$  ion dose D in the range of 300 ions/nm<sup>2</sup>, to clean the surface. XPS measurements to monitor the cleanliness were performed in between. An exemplary XPS spectrum of a clean substrate is presented in Fig. 3.5(a).



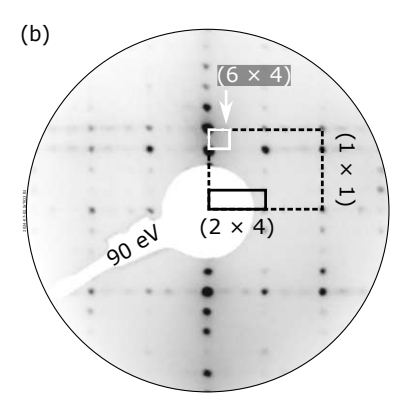


Figure 3.5: Characterization of the SrTiO<sub>3</sub>(110) substrate after three sputtering annealing cycles. (a) XPS spectrum (Al  $K_{\alpha}$ ) of a clean substrate with labelled characteristic peaks. (b) LEED pattern of the mixed  $(2 \times 4)$ - and  $(6 \times 4)$ -reconstructed surface at 90 eV. The unit cells of the bulk-derived  $(1 \times 1)$  (dashed rectangle), the  $(2 \times 4)$  (solid rectangle), and the  $(6 \times 4)$  (white rectangle) are highlighted.

The characteristic peaks are labelled. After three sputtering—annealing cycles, the surface was clean and exhibited a mixed  $(2 \times 4)$  and  $(6 \times 4)$  termination, which is shown in the LEED pattern in Fig. 3.5(b). The bulk-derived  $(1 \times 1)$  unit cell is indicated by the dashed rectangle, the  $(2 \times 4)$  unit cell by the solid rectangle, and the unit cell of the  $(6 \times 4)$  reconstruction is outlined in white.

#### $(4 \times 1)$ preparation 3.3.2

The preparation procedure aimed for a fully  $(4 \times 1)$ -reconstructed surface and is based on previous studies [21]. MBE using a low-temperature effusion cell was employed for Sr deposition. Sr was evaporated at 420 °C and subsequently deposited onto the substrate surface, which was kept at room temperature. A calibration of the deposition rate with a home-designed QCM allowed precise control of the growth process. Depositing Sr was only reasonable for structures richer in Ti than the  $(4 \times 1)$  reconstruction. In the other case, the samples were Ar<sup>+</sup>-sputtered with

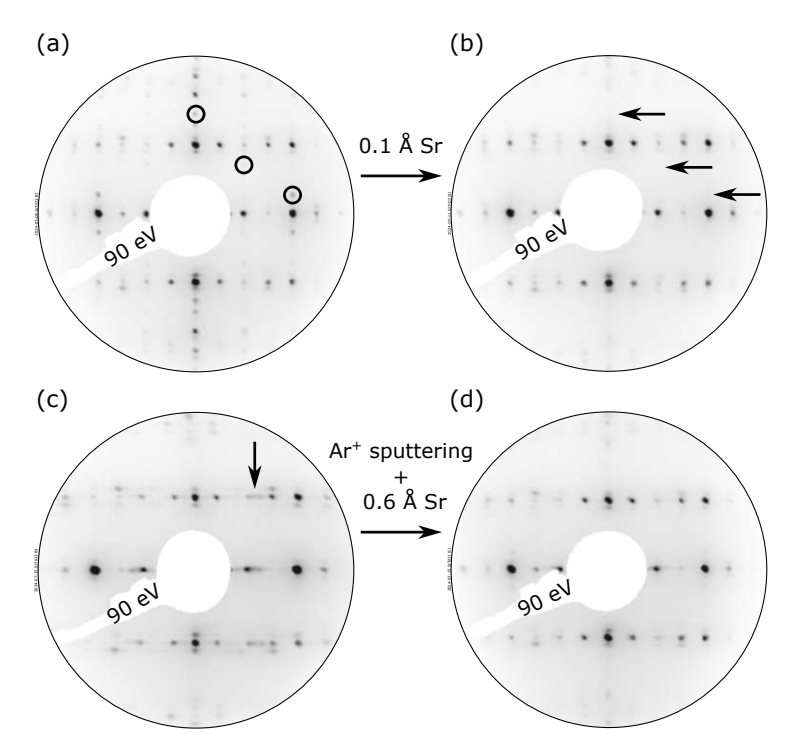


Figure 3.6: LEED patterns after Sr deposition and Ar<sup>+</sup> sputtering. (a) Initial state showing a mixed  $(4 \times 1)$  and  $(2 \times 4)$  reconstruction. The diffraction spots belonging to the  $(2 \times 4)$  reconstruction are marked with black circles. (b) After deposition of 0.1 Å Sr. The  $(2 \times 4)$  spots are barely recognisable (black arrows). (c)  $(4 \times 1)/(5 \times 1)$ -reconstructed surface before Ar<sup>+</sup> sputtering. The coexistence results in smeared out spots (black arrow). (d) Surface after Ar<sup>+</sup> sputtering followed by the deposition of 0.6 Å Sr, showing a mostly  $(4 \times 1)$  reconstruction.

a sputter current of  $I_{\rm sp}=1.6~\mu{\rm A}$  and sputtering times ranging from 5 to 7 min. Both the deposition and sputtering steps were accompanied by a subsequent O<sub>2</sub> annealing. Figure 3.6 illustrates the sensitivity of the reconstruction to slight compositional changes. The LEED pattern in Fig. 3.6(a) shows a mixed  $(2 \times 4)$ - and  $(4 \times 1)$ -reconstructed surface. Selected  $(2 \times 4)$  diffraction spots are highlighted by black circles. After depositing 0.1 Å of Sr, the diffraction spots belonging to the  $(2 \times 4)$  were nearly undetectable, as seen in Fig. 3.6(b) (black arrows). Figures 3.6(c) and 3.6(d) provide an example of the impact of the Ar<sup>+</sup> sputtering followed by the deposition of 0.6 Å Sr. Prior to the Ar<sup>+</sup> bombardment, the surface displayed a  $(4 \times 1)/(5 \times 1)$  reconstruction visible due to the blurring of the spot indicated by the black arrow in Fig. 3.6(c). The surface underwent a transformation into a predominantly  $(4 \times 1)$ -terminated structure as a result of the treatment [no blurring in Fig. 3.6(d), see the black arrow. Moreover, regardless of the preparation conditions, the recorded  $(4 \times 1)$  and  $(5 \times 1)$  diffraction patterns displayed a splitting of the spots.

#### Non-uniformity of the sample surface 3.3.3

After Ar<sup>+</sup> sputtering, the samples often displayed a non-uniformity in the LEED patterns depending on the position on which the measurement was performed, as seen in Fig. 3.7. The LEED pattern at 90 eV shows that the  $(4 \times 1)$  reconstruction, along with a bit of the  $(2 \times 4)$  reconstruction, appears in the center [Fig. 3.7(b)]. 2 mm above and 1 mm to the right of the center [Figs. 3.7(a) and 3.7(c), respectively, some spots indicated by the black arrows are smeared out, indicative of

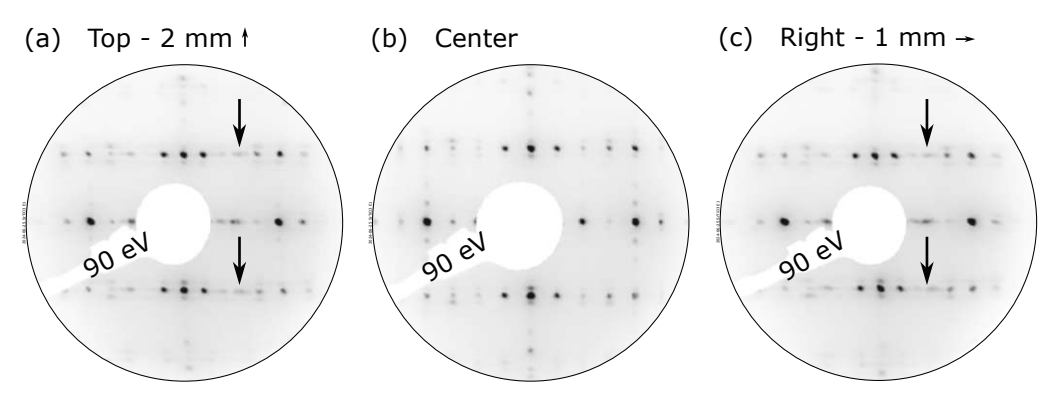


Figure 3.7: Diffraction patterns from LEED at 90 eV after Ar<sup>+</sup> sputtering. The sample shows different reconstructions depending on the location on which the electron beam hits the surface. (a) Top (2 mm above), and (c) right side (1 mm to the right) relative to the center, with smeared out diffraction spots outlined with black arrows. (b) Center of the sample mostly with  $(4 \times 1)$  reconstruction.

the presence of a mixed  $(4 \times 1)/(5 \times 1)$  structure in those regions. Through sputtering, and a subsequent long annealing step in O<sub>2</sub> for a few hours, it was possible to reduce this non-uniformity.

#### 3.3.4 Coexistence of reconstructions

Another observed phenomenon was the coexistence of the  $(4 \times 1)$ , and the  $(5 \times 1)$ or  $(2 \times 4)$  reconstructions, respectively, on the microscopic scale.

In Fig. 3.8(a), an STM image of a prepared SrTiO<sub>3</sub> sample after the deposition of Sr (0.6 Å) followed by  $O_2$  annealing on a mixed  $(4 \times 1)/(2 \times 4)$ -reconstructed surface is depicted. The terraces are flat and the surface looks homogeneous. In the diffraction pattern from LEED at 90 eV [Fig. 3.8(b)], a blurring of the spots occurs once more (black arrows). Figure 3.8(c) shows an atomically resolved STM image of the surface. Lines with different appearance are observable. The  $(4 \times 1)$  lines with their characteristic defined bright dots are partly substituted with lines that exhibit hole-like features, a characteristic of the  $(5 \times 1)$  reconstruction, indicated by the white rectangles. Additionally, the  $(5 \times 1)$  lines jump along the [001] direction (white arrows).

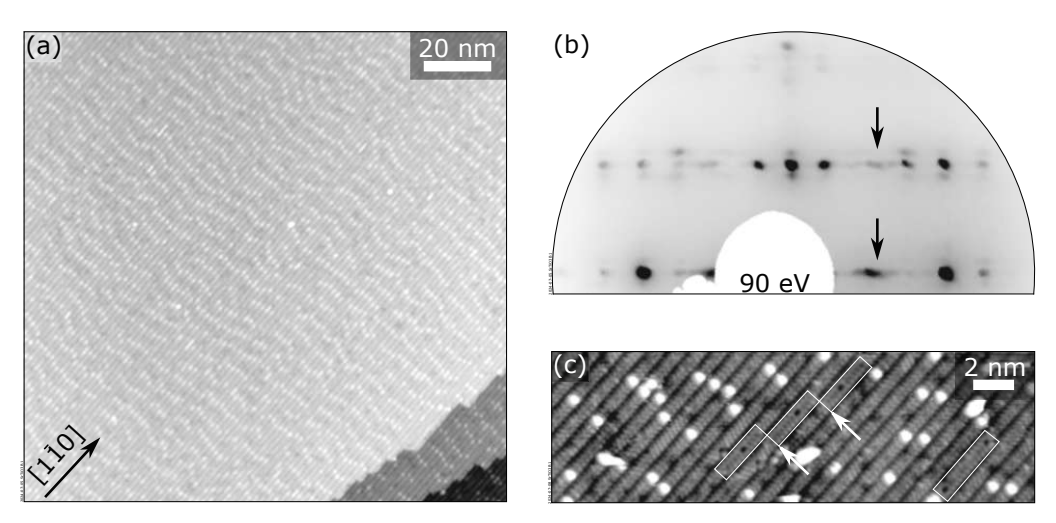
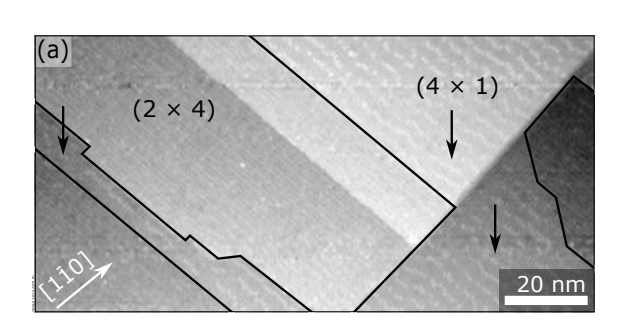


Figure 3.8: Coexistence of the  $(4 \times 1)$  and  $(5 \times 1)$  reconstructions on the SrTiO<sub>3</sub>(110) surface. (a) Overview STM image of a surface after Sr deposition on a  $(2 \times 4)$  reconstruction. (b) LEED pattern at 90 eV showing smeared-out spots (black arrows). (c) Atomically resolved STM image of the reconstructed surface.  $(4 \times 1)$  lines occur together with  $(5 \times 1)$  lines. The latter are outlined with white rectangles. The  $(5 \times 1)$  lines jump along the [001] direction (white arrows). (a)  $U_b = 2.4 \text{ V}$ ,  $I_t = 0.10 \text{ nA}$ ,  $134 \times 140 \text{nm}^2$ ; (c)  $U_{\rm b} = 3.1 \text{ V}$ ,  $I_{\rm t} = 0.10 \text{ nA}$ ,  $48 \times 16 \text{ nm}^2$ 



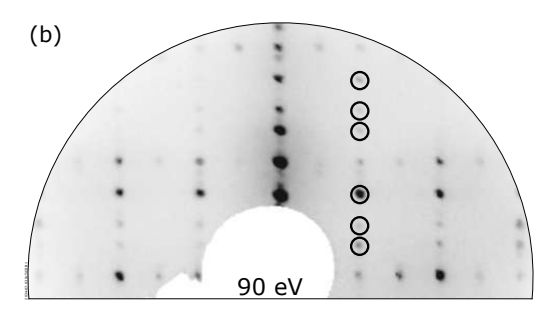


Figure 3.9: Coexistence of the  $(4 \times 1)$  and  $(2 \times 4)$  reconstructions on the SrTiO<sub>3</sub>(110) surface. (a) Overview STM image after Ar<sup>+</sup> sputtering of a mixed  $(2 \times 4)$  and  $(6 \times 4)$ surface, followed by deposition of Sr (1.5 Å) and O<sub>2</sub> annealing. The surfaces exhibits  $(4 \times 1)$ -reconstructed areas (black arrows) and  $(2 \times 4)$ -reconstructed ones (outlined in black). (b) LEED pattern at 90 eV showing a mixed  $(4 \times 1)/(2 \times 4)$  reconstruction. Some of the  $(2 \times 4)$  spots are outlined with black circles. (a)  $U_{\rm b} = 1.9 \text{ V}$ ,  $I_{\rm t} = 0.59 \text{ nA}$ ,  $200 \times 74 \text{ nm}^2$ 

Figure 3.9 illustrates the coexistence of the  $(4 \times 1)$  and  $(2 \times 4)$  reconstructions on the surface. The STM image in panel (a) depicts distinct areas with the  $(4 \times 1)$ reconstruction, identified by the characteristic white dots, indicated by the black arrows. The  $(2 \times 4)$  reconstruction is outlined in black. In Fig. 3.9(b), the LEED pattern (90 eV) also reveals a mixed  $(4 \times 1)/(2 \times 4)$  reconstruction, with a selection of  $(2 \times 4)$  diffraction spots marked by black circles.

#### 3.3.5 LEED-I(V) measurements

Three I(V) curves at different sample–screen distances from 25 to 720 eV were recorded, with an interval of 1 mm between each subsequent measurement. The three measurements will be averaged before comparing them with structure simulations to eliminate the grid contributions, as described in Section 2.5. Given that the simulations for comparing the experimental data with structure models are still in progress, the presentation of R factors of a comparison with models is not possible at this time. Instead, the curves recorded at different distances from the LEED screen throughout the same data acquisition are examined more closely.

The I(V) curves of the three distinct distances were compared to each other, and overall R factors between 0.07 and 0.13 were obtained. From the comparison of individual spots — same diffraction spots but different measuring distances — some R factors are clearly larger than others. In Fig. 3.10(a), the three intensities of the (-3/4|1) spot are shown, with the green curve representing the closest position to the LEED screen (front), the blue curve the position in the middle (center) and the red curve the measurement furthest away (back). It is evident that the red and blue

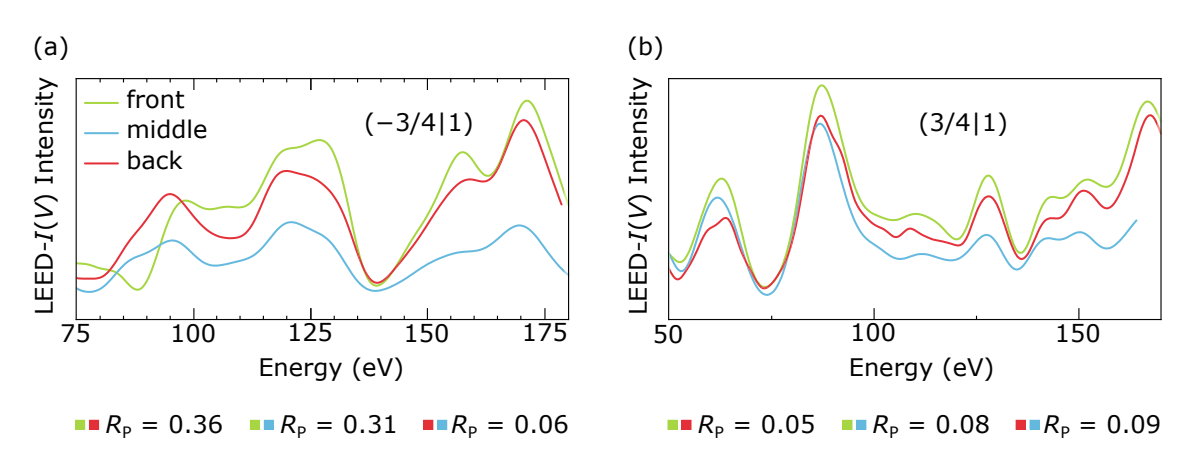


Figure 3.10: LEED-I(V) curves of SrTiO<sub>3</sub>-(4 × 1) measured at different distances between the sample and the LEED screen. The shortest distance is represented in green, the middle distance in blue, and the largest distance in red. (a) Intensities of the (-3/4|1)spot recorded at different screen distances. The blue and red curve are very similar in shape. Both curves compared to the green curve result in  $R_{\rm P}$  factors of 0.31 and 0.36, respectively. (b) Intensities of the (3/4|1) spot acquired at the same measurements as in panel (a). The curves agree well with each other and result in  $R_{\rm P}$  factors of less than 0.1.

curves are very similar in shape  $(R_{\rm P}=0.064)$ , yet they diverge significantly from the green curve. This disparity results in R factors of 0.36 and 0.31, for the red and green and for the blue and green curves, respectively. Figure 3.10(b) instead illustrates the data of the (3/4|1) spot compared in the same way, exemplifying a high degree of correlation between the data sets. R factors of less than 0.1 were obtained.

The LEED-I(V) data was extracted using the spot-tracking tool implemented in ImageJ [43]. During spot tracking across the energy range, the program encountered difficulties in correctly identifying the spots due to the spot splitting in the diffraction patterns. Figure 3.11 shows the tracked spots at energies between 115.5 eV and 137.5 eV. From the images, it can be seen that the spot tracker jumps from the correct spot [Fig. 2.7(a)], to the satellite on the top [Fig. 2.7(b)], and to the satellite at the bottom [Fig. 2.7(c)], with varying energies, as outlined by the red arrows.

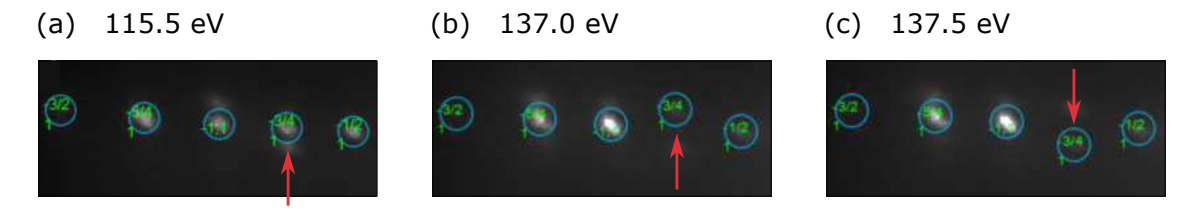


Figure 3.11: Spot-tracking of the (-3/4|1) spot at different energies. The tracker jumps (red arrows) between the spots of the superstructure.

#### 3.4 Discussion

The experimental data presented in this Chapter aligns with findings of previous studies [21]. In case of slight deviations from the ideal near-surface composition for the fully reconstructed  $(4 \times 1)$  surface, a coexistence of different structures appeared. Additionally, the already familiar splitting of the spots due to the periodicity of the antiphase domain boundaries was observed in every diffraction pattern of the  $(4 \times 1)$  and  $(5 \times 1)$  structures.

The results confirmed that the surface exhibits a  $(4 \times 1)$  or  $(5 \times 1)$  reconstruction for Sr depositions on an initial structure at the Ti-rich side of the phase diagram. Ar<sup>+</sup> sputtering followed by O<sub>2</sub> annealing enabled movement in the opposite direction along the phase diagram (Fig. 3.3), leading to structures richer in Ti. This can be attributed to the preferential removal of Sr during a sputtering-annealing cycle. After the sputtering process, the remaining O atoms at the surface are undercoordinated and can easily desorb. This leaves undercoordinated Sr and Ti atoms behind, which then evaporate during the postannealing [7]. Sr has a higher vapor pressure than Ti [62]) and is therefore more volatile. The result is a Ti enrichment of the surface.

The non-uniformity observed on the sample surface can be attributed to the annealing process. The circular shape of the IR laser spot results in higher temperatures in the central regions of the sample, while the outer areas, in direct contact with the sample plate, remain cooler. This temperature gradient causes enhanced Sr evaporation in the center, leading to a higher Ti concentration compared to the outer regions, and consequently to a non-uniformity on the surface. In addition, the sputtering process is carried out in a manner that ensures the Ar<sup>+</sup> ion beam does not raster over the clips, to prevent contamination with Ni, Cr, or Fe. The parameters like scan area and speed, and position offset if needed, are set while the sputter process already started. If this procedure takes too long, it may also impact the surface homogeneity, as some areas are possibly sputtered more (preferential removal of Sr). Large-scale non-uniformity is not an issue for LEED-I(V) measurements, as long as the sample is homogeneous within the approximately 1 mm diameter of the electron beam and that the same spot is consistently targeted for all measurements conducted at varying distances. The recorded I(V) data satisfied this requirement.

Throughout the investigation of the  $(4 \times 1)$  reconstruction, the LEED patterns exhibited a blurring of the spots along with the occurrence of coexisting  $(4 \times 1)$ -

and  $(5 \times 1)$ -reconstructed lines at the microscopic scale. This can be explained by the fact that the  $(4 \times 1)$  and  $(5 \times 1)$  lines are not randomly distributed, but the minority lines have a certain degree of ordering in their distance. This results in a superperiodicity along the [001] direction with coherence lengths in the same order of magnitude as the electron beam, which causes a splitting of the diffraction spots often apparent as blurring [Fig. 3.8]. Moreover, the SrTiO<sub>3</sub>(110) surface showed a coexistence of the  $(4 \times 1)$  and  $(2 \times 4)$  reconstruction, which was apparent in STM through distinct areas.

The spots associated with antiphase domain boundaries sometimes appear brighter than the actual  $(4 \times 1)$  spots in the LEED diffraction pattern, leading to jumps of the spot tracker and further to errors in the extracted intensities. Given that there is a high correlation in the majority of other instances with values below 0.1, it seems unlikely that the occurring discrepancy is due to the experimental setup. Instead, it is more likely related to the issues with post-processing. However, overall R factors in the 0.07–0.13 range between different data acquisitions still suggest a very good agreement and demonstrate the reproducibility of the LEED-I(V) measurements.

#### Conclusion 3.5

This Chapter provided an overview of the preparation and characterization of the  $(4 \times 1)$  reconstruction of SrTiO<sub>3</sub>(110). Furthermore, a comparison of the LEED-I(V) measurements at different positions during the data acquisition emphasized the impact of postprocessing on the quality of the data.

The near-surface composition was adjusted by depositing Sr and Ar<sup>+</sup> sputtering with subsequent  $O_2$  annealing.  $SrTiO_3(110)$  displays a variety of surface reconstructions depending on the relative Sr or Ti content in the near-surface region. The results confirmed that Sr deposition results in  $(4 \times 1)$ - or  $(5 \times 1)$ -reconstructed surface structures. Phases richer in Ti could be achieved with Ar<sup>+</sup> sputtering, which is attributed to a preferential removal of Sr relative to Ti during the subsequent annealing.

Several phenomena occurred during the preparation: Local temperature variations caused by the circular IR laser spot led to increased Sr evaporation at the center, resulting in a non-uniform Sr-to-Ti stoichiometry across the sample surface. This led to the appearance of regions exhibiting a mixture of different reconstructions on the macroscopic scale. On the microscopic scale, a coexistence of  $(4 \times 1)$ and either  $(5 \times 1)$  or  $(2 \times 4)$  reconstructions, respectively, was observed, which is attributed to the sensitivity of the near-surface stoichiometry to local variations.

The splitting of diffraction spots in the LEED patterns was attributed to the presence of periodic antiphase boundaries.

A challenge encountered while extracting the LEED-I(V) data underscores the importance of postprocessing and possible pitfalls. The process of spot tracking is rendered more challenging by the occurrence of split spots, which the program sometimes identifies incorrectly. This leads to errors in the extracted intensities and needs to be addressed prior to comparing the data with the simulated structure models. A temporary solution would a extraction of the intensities in two steps: At lower energies, where splitting of the diffraction spots is evident but with spots that are further apart, one could use a large, circular integration area that encompass both the primary and the satellite spots. At larger energies, where the spots become closer and the splitting of the spots is less problematic, the use of smaller integration areas is possible to prevent their overlap. Subsequently, the two extractions are stitched together over a narrow common energy range.

# $La_{0.8}Sr_{0.2}MnO_3$ films on 4. $SrTiO_3(001)$

#### Introduction 4.1

Lanthanum-strontium manganite ( $La_{1-x}Sr_xMnO_{3\pm\delta}$ , LSMO) is an ABO<sub>3</sub> perovskite oxide with numerous interesting properties and resulting application possibilities. Due to its high electrochemical stability, high electrical conductivity, and high thermal stability, it is one of the most studied and used cathode materials in solid-oxide fuel cells [63, 64]. In thin films, strong lattice-charge-spin coupling allows for the manipulation of magnetic and electronic-transport properties, which is utilized in spintronic devices [65]. It exhibits different electronic ground states, which can lead to either an antiferromagnetic insulating phase or a ferromagnetic metallic phase depending on the doping level, which makes it also subject of research in fundamental physics [66].

This chapter addresses the preparation and characterization of La<sub>0.8</sub>Sr<sub>0.2</sub>MnO<sub>3</sub> thin films grown on Nb-doped  $SrTiO_3(001)$  substrates by PLD. The films exhibit two distinct surface terminations: a Mn-rich surface after growth, and a (La/Sr)rich surface obtained through Ar<sup>+</sup> sputtering followed by oxygen annealing. Mn deposition from an MnO target recovered the  $MnO_x$ -terminated phase. The growth and sputtering processes were monitored using STM, LEED and XPS. A detailed overview of the preparation and characterization is given in Sections 4.3.1–4.3.5. After successfully preparing the two different surface terminations, LEED-I(V) measurements were conducted on both. The results are presented in Section 4.3.6. All the results are discussed in Section 4.4.

### Structure and surface terminations 4.2

In La<sub>1-x</sub>Sr<sub>x</sub>MnO<sub>3± $\delta$ </sub>, La is partially substituted with Sr (A site), where x represents the Sr content. The B site is occupied by Mn. The system undergoes a structural transformation from a orthorhombic to a rhombohedral lattice for Sr contents above 15%, and becomes tetragonal at Sr contents around 50% [67]. For



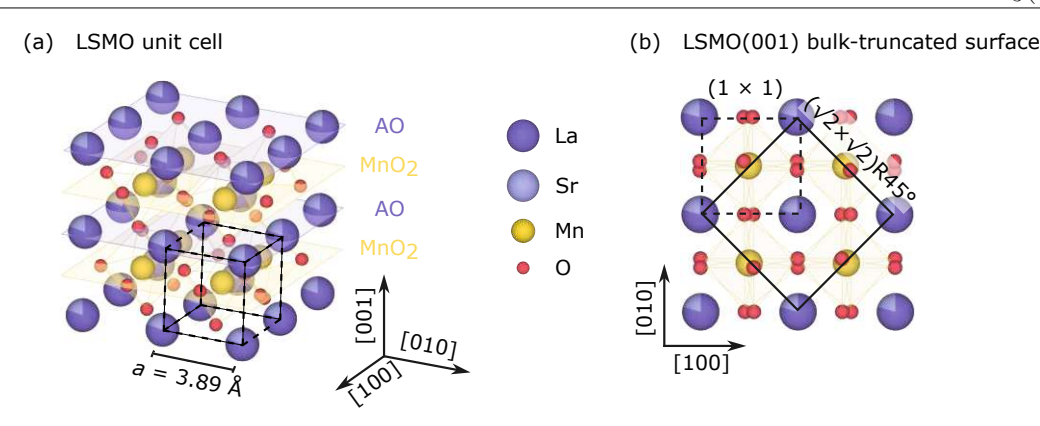


Figure 4.1: Bulk-truncated structure of La<sub>0.8</sub>Sr<sub>0.2</sub>MnO<sub>3</sub>. (a) Perspective view. The dashed cube indicates the  $(1 \times 1)$  perovskite unit cell. (b) Top view with the LSMO primitive unit cell of the surface marked by the solid line. It has a  $(\sqrt{2} \times \sqrt{2})$ R45° superperiodicty with respect to the cubic-perovskite cell (dashed).

 $La_{0.8}Sr_{0.2}MnO_3$  (La:Sr = 80:20), the structure adopts a rhombohedral unit cell with a lattice constant  $a_{\rm R}=5.4732(2)$  Å and an angle  $\alpha_{\rm R}=60.5120(2)^{\circ}$  between the basis vectors [68]. It can be considered as pseudocubic — a deviation of the ideal cubic structure — with the parameters  $a_{PC} = 7.7998(2)$  Å and  $\alpha_{PC} = 90.503^{\circ}$ [69]. The crystal lattice is constructed by building blocks of face-sharing perovskite cubes  $(a = a_{PC}/2 = 3.8999 \text{ Å})$ , where La or Sr occupy the corners and Mn the centers. Mn is sixfold coordinated by oxygen, with the octahedra rotated and tilted in alternating directions. This results in a  $(\sqrt{2} \times \sqrt{2})$ R45° unit cell with respect to the cubic-perovskite lattice, such as the one of  $SrTiO_3$ , as seen in Fig. 4.1(b). The crystallographic directions used in this Chapter follow the cubic-perovskite lattice.

The structure model of Fig. 4.1(a) shows that when cutting the crystal along (001) planes, either the AO layer or the MnO<sub>2</sub> layer stays at the surface. There is no possibility of an existing bulk-truncated structure, as this would create a polar surface for both terminations [8]. Previous research [70] showed that LSMO(001) reveals two different surface reconstructions: a  $(\sqrt{2} \times \sqrt{2})$ R45° an incommensurately modulated structure. The bulk-truncated model indeed exhibits a  $(\sqrt{2} \times \sqrt{2})$ R45° periodicity for the AO plane. However, the  $AO_x$  termination is unlikely to represent a bulk-like stoichiometric AO surface, as such a configuration would not be stable. Instead, it is believed that the surface is stabilized through Sr segregation [71]. The incommensurate surface is typically present on stoichiometric as-grown films. STM studies showed that the surface consists of an aperiodic arrangement of features which lack translational symmetry in real space, yet exhibit sharp diffraction spots in reciprocal space. Four translation vectors are required to describe the diffraction pattern. The AO<sub>x</sub> structure is attributed to the  $(\sqrt{2} \times \sqrt{2})$ R45° surface, as XPS and LEIS experiments indicated that the as-grown (aperiodic) films are Mn-rich relative to the  $(\sqrt{2} \times \sqrt{2})$ R45° surface [70]. Therefore, the two surfaces will be referred to as MnO<sub>x</sub> (as-grown, aperiodic) and AO<sub>x</sub> ( $\sqrt{2} \times \sqrt{2}$ )R45° in the following.

#### Sample preparation and results 4.3

#### 4.3.1 $SrTiO_3(001)$ substrates

For LSMO film growth, single-crystalline  $5 \times 5 \times 0.5 \text{ mm}^3$  Nb-doped (for conductivity) SrTiO<sub>3</sub>(001) substrates with a miscut of less than 0.2° from CrysTec GmbH were used. SrTiO<sub>3</sub> crystallizes in a perovskite structure (a = 3.905 Å) with alternating SrO and TiO<sub>2</sub> layers along the (001) direction, see Fig. 3.2. The miscut of the substrate leads to SrO- or TiO<sub>2</sub>- terminated terraces, which get smaller with increasing miscut. As PLD requires well-defined surfaces, the samples were prepared to only exhibit TiO<sub>2</sub>-terminated surfaces. However, the idea of perfectly SrO- or TiO<sub>2</sub>- terminated terraces remains unrealistic, as the SrTiO<sub>3</sub>(001) surfaces are never bulk-truncated.

Before introducing the substrate into the UHV chamber, it was cleaned as discussed in Section 2.6.1 and subsequently annealed at 1000 °C for 12 h in air. This led to smooth terraces observed in ambient AFM. To remove excess SrO on the surface, the substrate was boiled in deionized ultrapure water [72, 73] for approximately 5 min and mounted as described in Section 2.6.2.

### In-situ preparation

Once the sample was inserted in the UHV chamber, a test annealing at 1000 °C with an oxygen partial pressure  $p_{\rm O_2}=6\times 10^{-6}$  mbar was done to check the mounting. Afterwards, the substrates were sputtered with Ar<sup>+</sup> ions at a sputter current of  $I_{\rm sp}=1.6~\mu{\rm A}$  and an argon partial pressure  $p_{\rm Ar}=5\times10^{-6}$  mbar for 10–15 min. The area for sputtering was chosen to be  $4.5 \times 4.5 \text{ mm}^2$ , the emission current set to  $I_{\rm em} = 10$  mA. The sputtering was followed by  $O_2$  annealing at the same conditions as the test annealing. For STM-mounted samples, a characterization with STM was performed. A large-area STM image of the surface of the SrTiO<sub>3</sub>(001) substrate is depicted in Fig. 4.2(a). Two different domains perpendicular to each other indicated by the black arrows are visible, and can be seen in detail in Fig. 4.2(c), where the unit cell is marked by a white rectangle. The LEED pattern in Fig. 4.2(b) shows

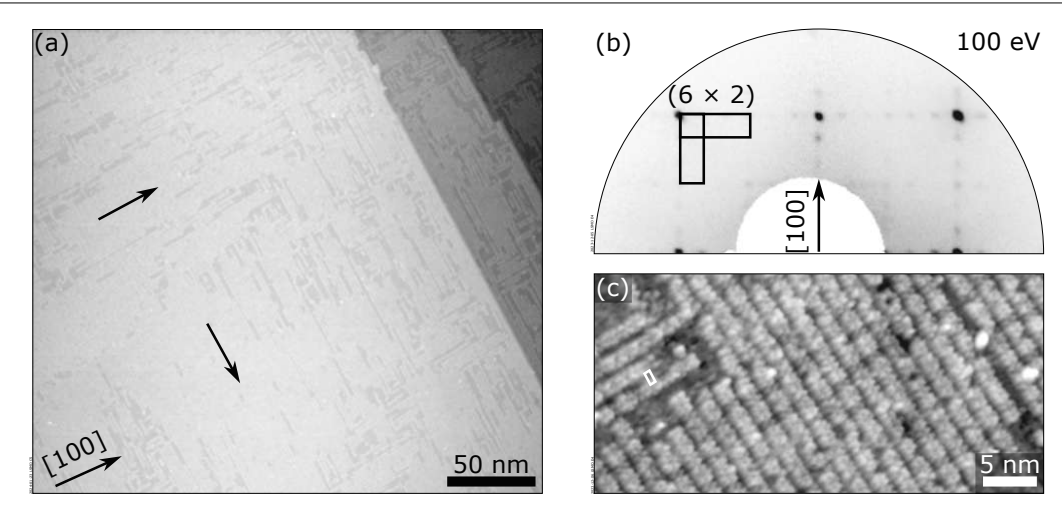


Figure 4.2: Characterization of the surface of the SrTiO<sub>3</sub>(001) substrate after one sputtering—annealing cycle. (a) Large-area STM image of substrate surface. black arrows indicate the two rotational domains present, seen in detail in panel (c). (b)  $(6 \times 2)$  LEED with the two domains at 100 eV. The unit cells are marked in black. (a)  $U_{\rm b} = +1.7 \text{ V}$ ,  $I_{\rm t} = 0.53 \text{ nA}$ ,  $300 \times 260 \text{ nm}^2$ ; (c)  $U_{\rm b} = +2.0 \text{ V}$ ,  $I_{\rm t} = 0.11 \text{ nA}$ ,  $43 \times 25 \text{ nm}^2$ .

a  $(6 \times 2)$  reconstruction with two rotational domains. The  $(6 \times 2)$  unit cells are indicated by the black rectangles. XPS analysis was performed to ensure the cleanliness. All substrates were clean after one sputtering—annealing cycle.

#### 4.3.2Surface structures

Detailed STM images of the MnO<sub>x</sub>-rich and AO<sub>x</sub>-rich surfaces are illustrated in Figs.  $4.3(a_1)$  and  $4.3(b_1)$ , respectively. The surfaces can easily be distinguished based on their coverage of adsorbates. No adsorbates are discernible on the  $MnO_x$ rich phase, and the structure appears to have no translational symmetry. In contrast, the  $AO_x$ -rich structure is covered with a considerable number of adsorbates and exhibits a  $(1 \times 1)$  periodicity in STM. Figures 4.3(a<sub>2</sub>) (MnO<sub>x</sub>) and 4.3(b<sub>2</sub>)  $(AO_x)$  depict their resulting LEED patterns generated by a fast Fourier transformation (FFT) of the images using Image J. Figures 4.3(a<sub>3</sub>) and 4.3(b<sub>3</sub>) show the corresponding diffraction patterns, together with the basis vectors of the  $(\sqrt{2} \times \sqrt{2})$ R45° structure (black) and the two additional vectors needed for the aperiodic surface (red). Since the scanning direction of the STM is rotated by 60°, the FFT-patterns are similarly rotated. The diffraction spots visible in both LEED patterns exhibit a cross-like shape.

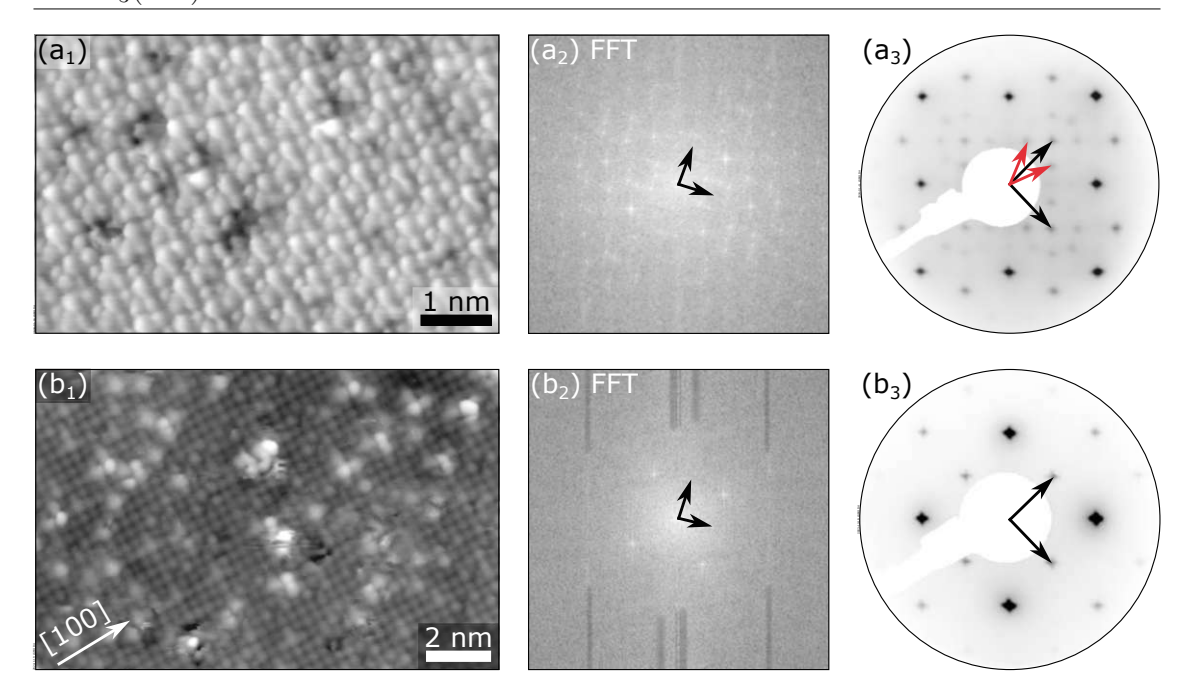


Figure 4.3: Characterization of the two distinct surfaces of LSMO(001). (a<sub>1</sub>) STM image of the  $MnO_x$  surface. No adsorbates are visible, and the surface appears aperiodic. (a<sub>2</sub>) Resulting diffraction pattern generated by the FFT of panel (a<sub>1</sub>). (b<sub>1</sub>)  $AO_x$  termination covered with adsorbates. The surface exhibits a  $(1 \times 1)$  periodicity in STM.  $(b_2)$  Generated diffraction pattern of the  $AO_x$  surface by FFT.  $(a_3)$ ,  $(b_3)$  Corresponding LEED diffraction patterns at 90 eV, with cross-like diffraction spots. The  $(\sqrt{2} \times \sqrt{2})$ R45° unit-cell vectors are indicated by the black arrows, and the two additional vectors to describe the MnO<sub>x</sub>-rich surface are highlighted in red in panel (a<sub>3</sub>). (a<sub>1</sub>)  $U_{\rm b}=+1.4~{\rm V},$  $I_{\rm t} = 0.17 \text{ nA}, 10 \times 6 \text{ nm}^2; (b_1) U_{\rm b} = +2.1 \text{ V}, I_{\rm t} = 0.13 \text{ nA}, 15 \times 9 \text{ nm}^2.$ 

#### 4.3.3 LSMO film growth

Before growing LSMO films, the LSMO target was preablated at the same conditions as during the actual growth, as discussed in Section 2.2. The parameters for LSMO film growth were: repetition rate f = 1 Hz, laser fluence F = 1.87 J/cm<sup>2</sup>, and substrate temperature T=800 °C, followed by an  $O_2$  postannealing, based on the recipe by Franceschi et al. [69].

In total, three LSMO depositions were performed. The first deposition was performed at  $p_{\rm O_2} = 5.7 \times 10^{-2}$  mbar. Another deposition followed at a lower pressure of  $p_{\rm O_2} = 3.8 \times 10^{-2}$  mbar, with characterization measurements conducted in between. Both depositions led to the diffraction pattern of the aperiodic structure in LEED [Fig. 4.4(b)]. Fig. 4.4(a) shows an STM image of an as-grown LSMO film  $(p_{O_2} = 5.7 \times 10^{-2} \text{ mbar}, 1800 \text{ pulses}, \text{ one unit cell corresponding to}$ 66 pulses). The surface exhibits a second phase preferentially located at the step edges (black arrows) and a long-range modulation of the height. Detailed STM

images in Figs.  $4.4(c_1)$  and  $4.4(c_2)$  present the different appearing phases, where the enlarged image shows that the small islands and 'half-step' phases correspond to the periodic  $AO_x$  termination and the larger areas to the aperiodic  $MnO_x$  termination. The height profiles of the corresponding steps can be seen in Fig. 4.4(d), where the  $AO_x$  phase (along the black line) has a step height approximately half the height of an  $MnO_x$ - $MnO_x$  step (along the red line).

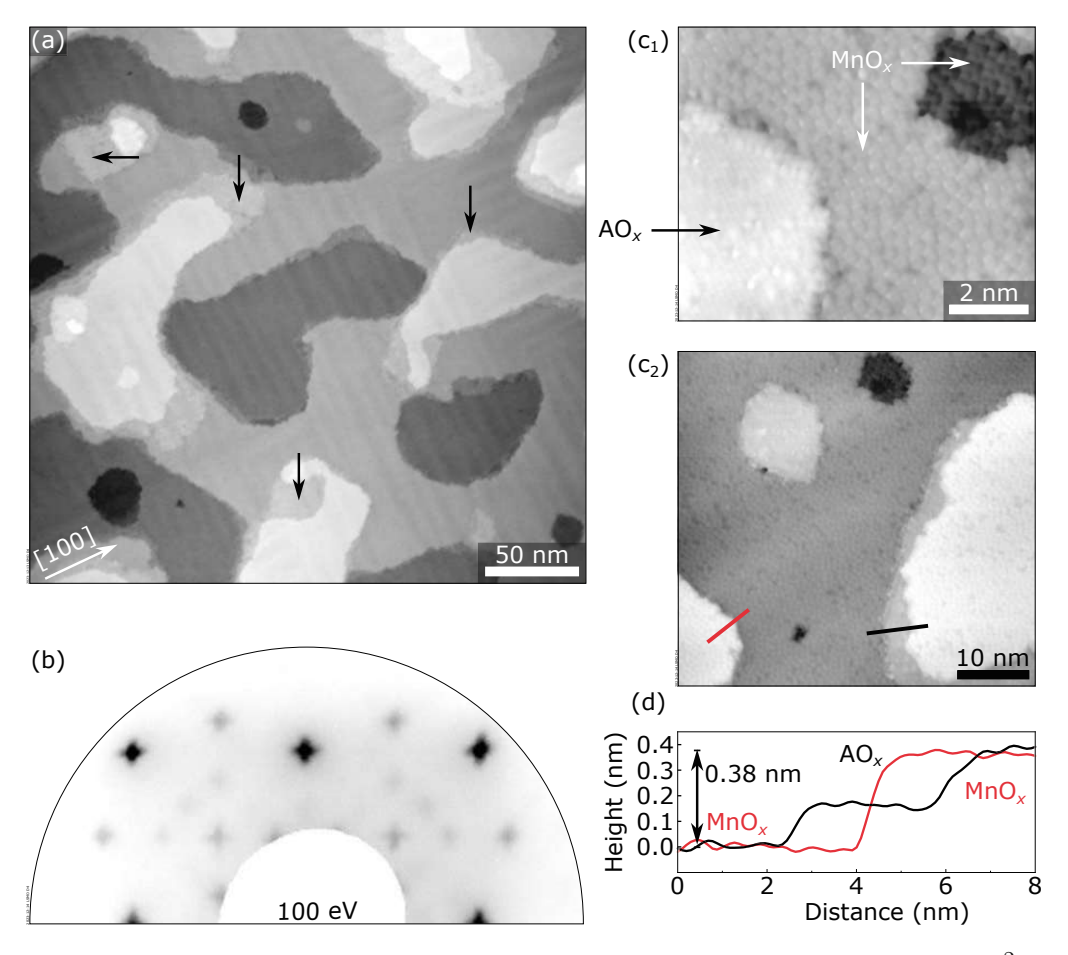


Figure 4.4: Detailed view on the surface after LSMO film growth ( $p_{O_2} = 5.7 \times 10^{-2}$  mbar, 1800 pulses, corresponding to  $\approx 11$  nm). (a) Large-area STM image. Two phases are present. The phase with the smaller surface coverage is preferentially located at the step edges (black arrows). (b) LEED measurement of the surface at 100 eV, showing the diffraction pattern of the  $MnO_x$  termination.  $(c_1)$ ,  $(c_2)$  Detailed STM images of the two phases. In panel (c<sub>1</sub>), the island exhibits a periodic structure, which corresponds to the  $AO_x$  phase; the neighboring terraces, instead, have the aperiodic  $MnO_x$  structure. (d) Height profiles along the red and black lines in panel ( $c_2$ ). The  $AO_x$  phase has approximately half the height of a cubic-perovskite unit cell with respect to the  $MnO_x$  phase. (a)  $U_{\rm b} = +2.2 \text{ V}$ ,  $I_{\rm t} = 0.19 \text{ nA}$ ,  $300 \times 300 \text{ nm}^2$ ; (c<sub>1</sub>), (c<sub>2</sub>)  $U_{\rm b} = +1.8 \text{ V}$ ,  $I_{\rm t} = +0.12 \text{ nA}$ ,  $20 \times 14 \text{ nm}^2$  and  $53 \times 41 \text{ nm}^2$ , respectively.

#### Ar<sup>+</sup> sputtering 4.3.4

Cycles of Ar<sup>+</sup> sputtering, followed by annealing at the growth conditions were conducted on the grown LSMO films to prepare the  $AO_x$  phase. The emission current  $I_{\rm em}$  was set to 5 mA, the energy to 3 keV, the area sputtered to 4  $\times$  4 mm<sup>2</sup>,  $p_{\rm Ar} = 5 \times 10^{-8}$  mbar,  $I_{\rm sp} = 0.46~\mu{\rm A}$ , and sputtering times in the range of 4–8 min. After sputtering and postannealing, the surface exhibited the  $(\sqrt{2} \times \sqrt{2})$ R45° periodicity, as observed in LEED at 100 eV [Fig. 4.5(a<sub>1</sub>)]. A small contribution from the aperiodic phase was visible in the LEED pattern at low energies (30 eV), as seen in Fig. 4.5(a<sub>2</sub>) (black arrows). This decreased with increasing sputtering time and was fully eliminated after a total sputtering time of 24 min [Figs.  $4.5(b_1)$  and  $4.5(b_2)$ ]. STM imaging revealed that a small fraction of a disordered phase with a half-unitcell high step relative to the ordered  $AO_x$  phase was present [Figs. 4.5(c) and 4.5(d)]. The white arrows point out the disordered phase. A surface that exhibits only a single phase, attributed to the  $(\sqrt{2} \times \sqrt{2})$ R45° periodicity in LEED, could not be prepared. Because that phase is disordered, it should not contribute to the diffraction pattern. Thus, LEED-I(V) measurements were performed.

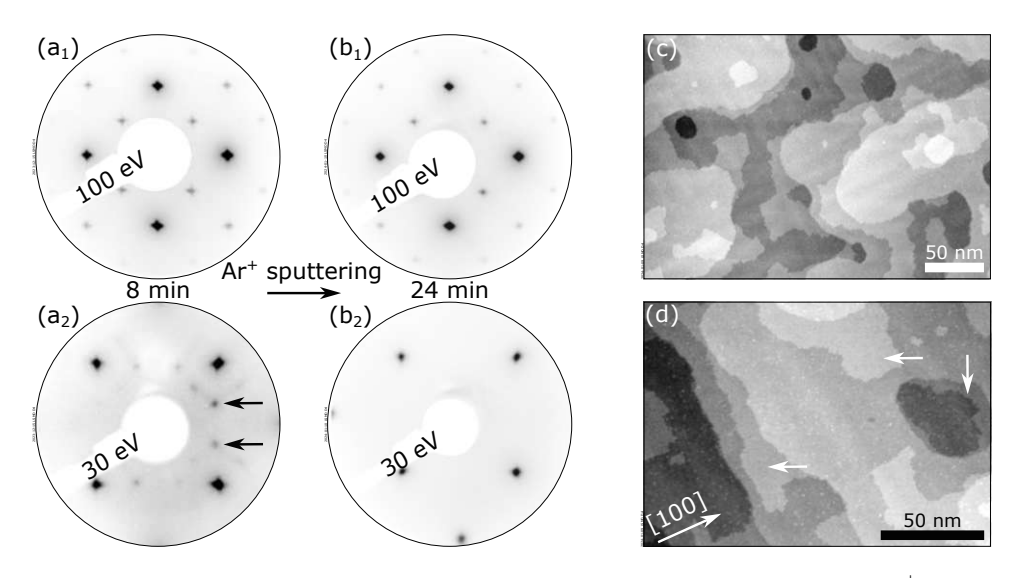


Figure 4.5: LEED patterns and STM images of the surface after Ar<sup>+</sup> sputtering. (a<sub>1</sub>) LEED pattern after 8 min sputtering recorded at 100 eV. (b<sub>1</sub>) LEED pattern at 100 eV after 24 min of sputtering. Both surfaces exhibit the  $(\sqrt{2} \times \sqrt{2})R45^{\circ}$  periodicity. (a<sub>2</sub>) LEED pattern after 8 min of Ar<sup>+</sup> sputtering at 30 eV; diffraction spots from the aperiodic phase (black arrows) are visible. (b<sub>2</sub>) After 24 min sputtering, the diffraction spots of the aperiodic phase disappeared; at 30 eV only  $(\sqrt{2} \times \sqrt{2})$ R45° diffraction spots are visible. (c) Overview STM image after 20 min of Ar<sup>+</sup> sputtering. The surface exhibits an additional phase located at the step edges which is disordered. (d) Detailed view on the disordered phase (white arrows). (c)  $U_{\rm b} = +2.1 \text{ V}$ ,  $I_{\rm t} = +0.34 \text{ nA}$ ,  $300 \times 210 \text{ nm}^2$ ;  $U_{\rm b} = +2.1 \text{ V}, I_{\rm t} = +0.26 \text{ nA}, 150 \times 110 \text{ nm}^2.$ 

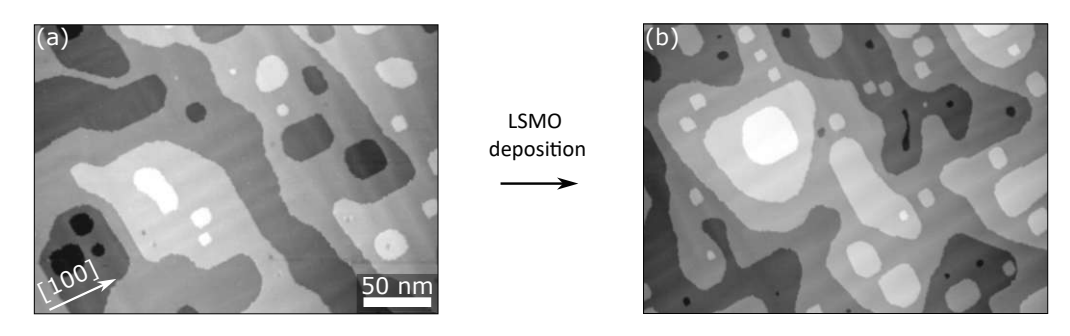


Figure 4.6: STM images of the surfaces after film growth. (a) After MnO deposition  $(p_{\rm O_2}=0.1~{\rm mbar},\,195~{\rm pulses},\,{\rm room~temperature})$  on the  $(\sqrt{2}\times\sqrt{2}){\rm R}45^\circ$  phase. The surface is free of the 'half-step' phase. (b) After LSMO deposition ( $p_{O_2} = 4.5 \times 10^{-2}$  mbar, 364 pulses) on top. Still no half steps visible. (a)  $U_{\rm b} = +1.9 \text{ V}$ ,  $I_{\rm t} = 0.22 \text{ nA}$ ,  $300 \times 215 \text{ nm}^2$ ; (b)  $U_b = +1.9 \text{ V}$ ,  $I_t = 0.33 \text{ nA}$ ,  $300 \times 215 \text{ nm}^2$ .

#### 4.3.5 MnO deposition and subsequent LSMO film growth

An MnO deposition (195 pulses) was performed at room temperature on top of the  $(\sqrt{2} \times \sqrt{2})$ R45° phase at f = 2 Hz,  $p_{O_2} = 0.1$  mbar, and F = 1.5 J/cm<sup>2</sup>. This was followed by annealing at 800 °C and  $p_{\rm O_2} = 5.7 \times 10^{-2}$  mbar. The LEED pattern revealed the diffraction pattern of the  $MnO_x$  termination, and STM images showed a surface without the 'half-step' phase [Fig. 4.6(a)]. An LSMO deposition (364 pulses, corresponding to an additional  $\approx 2$  nm) on top was done at  $p_{O_2} = 4.5 \times 10^{-2}$  mbar, resulting again in a surface free of the 'half-step' phase in STM [Fig. 4.6(b)]. LEED-I(V) measurements were conducted, on both MnO<sub>x</sub>-terminated surfaces.

#### LEED-I(V) measurements 4.3.6

LEED-I(V) curves were recorded for distinct preparations: the  $(\sqrt{2} \times \sqrt{2}) R45^{\circ}$ structure achieved through Ar<sup>+</sup> sputtering, and two aperiodic surface structures resulting from LSMO and MnO deposition, respectively. Figure 4.7 illustrates the comparison of a selected set of I(V) curves acquired on the differently prepared  $MnO_x$ -rich surfaces. Their corresponding agreement, using the Pendry R factor  $(R_{\rm P})$  is shown, with one small [Fig. 4.7(a<sub>1</sub>)] and one somewhat larger [Fig. 4.7(a<sub>2</sub>)]  $R_{\rm P}$ . The MnO<sub>x</sub> termination prepared via LSMO film growth is represented in yellow, the one prepared through MnO deposition in red. A maximum  $R_{\rm P}$  of 0.2 was obtained for the comparison of individual diffraction spots. It exhibits small  $R_{\rm P}$ factors for both high-index spots, exemplified with the (1|5) spot in Fig. 4.7(c<sub>1</sub>), and low-index spots as the LEED-I(V) measurements of the (0|1) spot in Fig. 4.7(c<sub>2</sub>). The overall  $R_{\rm P}$  amounts to 0.08.

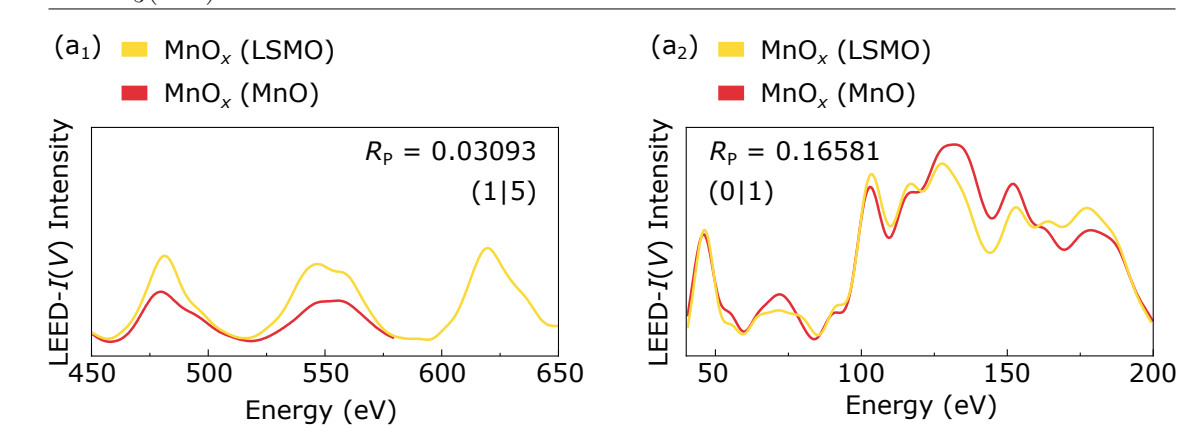


Figure 4.7: Selected LEED-I(V) curves and resulting  $R_{\rm P}$  factors of the two differently prepared  $MnO_x$  surfaces. The  $MnO_x$  termination obtained from LSMO film growth is presented in yellow, and the  $MnO_x$  termination obtained from MnO deposition in red. One small and one large  $R_P$  factor is presented in panels  $(a_1)$  and panels  $(a_2)$ , respectively. The comparison results in small  $R_P$  factors for both high-index spots [panel (a<sub>1</sub>)] and lowindex ones [panel  $(a_2)$ ].

#### Discussion 4.4

The presented data of the LSMO surface preparations correlates with results observed in previous studies [70]. Surfaces of as-grown films reconstructed to a large extent in the aperiodic, Mn-rich structure. Since the first LSMO deposition resulted in a surface with coexisiting surface terminations, the oxygen partial pressure was adjusted to eliminate the small amount of the  $AO_x$  phase. Changing the pressure to lower values enriches the plasma plume with the lighter species [25], which is Mn in the case of LSMO. The resulting film still showed a 'half-step' phase, attributed to an  $AO_x$  phase, which indicates that the PLD parameters for the deposition were slightly off from those needed to obtain a monophase  $MnO_x$  reconstruction.

Removing the  $MnO_x$  phase with  $Ar^+$  sputtering is possible, due to a preferential oxygen sputtering. Additionally, the caused beam damage creates undercoordinated O atoms, resulting in weakly bound O atoms at the surface that can easily desorb [1]. Both processes leave undercoordinated cations behind, which are removed during the postannealing step. The vapor pressure for Mn is higher than that of La [62] and is therefore preferentially evaporated during annealing.

The pseudocubic LSMO lattice deviates by 0.503° from the cubic SrTiO<sub>3</sub> lattice, which causes LSMO to grow in domains. The surfaces of these domains are slightly tilted, giving rise to the cross-like shape of the LEED spots. This tilt also accounts for the undulations observed in the STM images [70].

#### 4.4.1 Influence of the bulk structure on the I(V) curves

For the compared aperiodic structures, an overall  $R_{\rm P}$  of 0.08 indicates a perfect agreement between the two surfaces, meaning they are identical at the subpicometer level. In addition to the comparison of the  $MnO_x$  surfaces, the LEED-I(V) measurement conducted on the  $AO_x$  phase was compared to both the aperiodic structure obtained via LSMO growth and the one resulting from MnO deposition. The  $R_{\rm P}$  values obtained from this are obviously very large (> 0.35), as different structures were compared. However, the  $R_{\rm P}$  factors are only used for quantification of their agreement in order to asses the effect of the bulk structure on the LEED-I(V) measurements. Figure 4.8(a<sub>1</sub>) illustrates a stepwise limitation of the

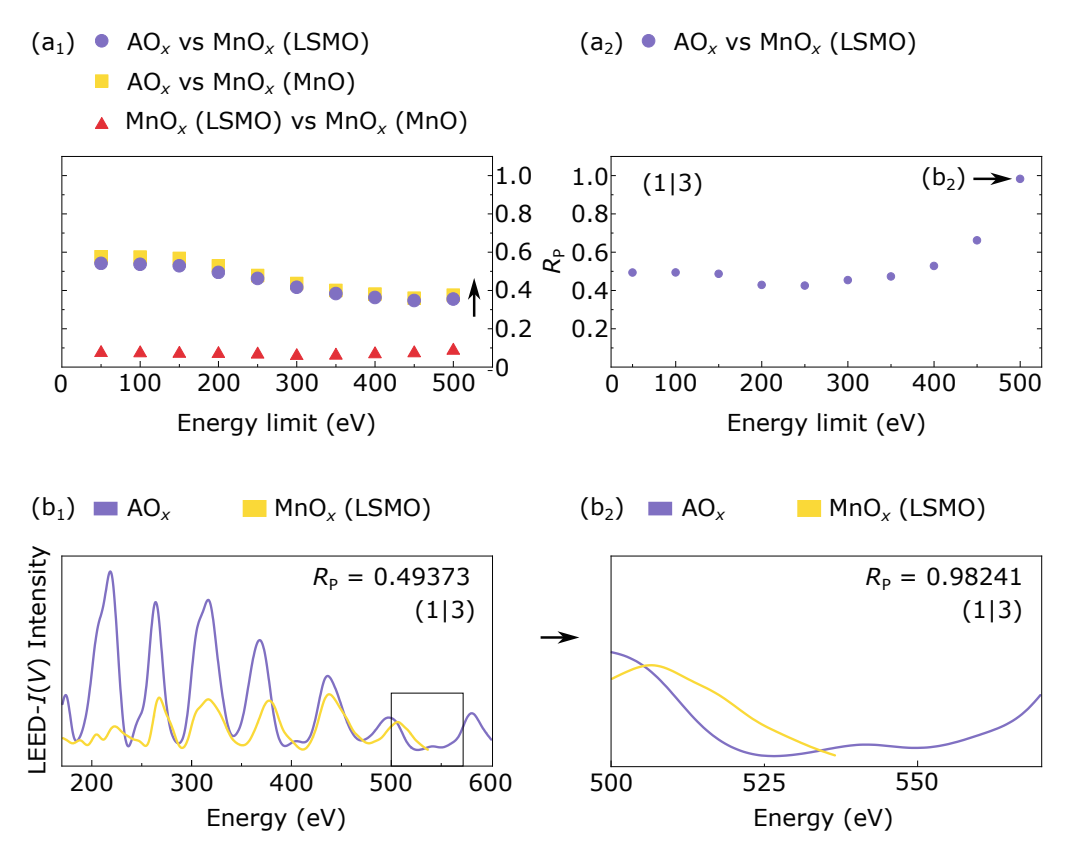


Figure 4.8: (a<sub>1</sub>) Energy dependence of the overall R<sub>P</sub> factors obtained from the LSMO structure comparisons. The restriction to higher energy limits results in decreasing R<sub>P</sub> factors. (a<sub>2</sub>)  $R_P$  factors of the (1|3) spot obtained from the comparison of the  $AO_{x^-}$  and  $MnO_x$ -terminated surface (via LSMO film growth) with increasing energy limits. The  $R_{\rm P}$  factors increase with increasing energy limit. (b<sub>1</sub>) I(V) curves of the (1|3) spot from the  $AO_x$  and  $MnO_x$  termination. (b<sub>2</sub>) Enlarged view of the data for the (1|3) beam above 500 eV. As the energy interval taken into account for the  $R_{\rm P}$  calculations becomes very small, the sensitivity to deviations in the I(V) curves becomes high, and  $R_P$  factors increase accordingly.

energies included in the calculation of  $R_{\rm P}$  factors towards higher energy values.  $R_{\rm P}$  factors of the aperiodic structure comparison (black) remain constant within  $\pm 0.02$ , while the overall  $R_{\rm P}$  factors for the AO<sub>x</sub>- and the MnO<sub>x</sub>-terminated reconstructions (different preparation) decrease (yellow and red). Electrons with higher energies penetrate deeper into the bulk, generating a signal that increasingly represents the bulk structure. As they all exhibit the same bulk structure, the values do not change for the same surface structures, but decrease by approximately 0.2 for the comparison of the  $MnO_x$  with the  $AO_x$  terminations. At very large values of the lower-energy limit (500 eV), the  $R_{\rm P}$  factors start to increase again (black arrow). In Fig. 4.8(a<sub>2</sub>), the dependency of  $R_{\rm P}$  for one representative beam is shown. Interestingly the  $R_{\rm P}$  for curves measured on the  ${\rm AO}_x$  and  ${\rm MnO}_x$  terminations steadily increases as the lower limit of the energy range considered increases above 350 eV. It reaches values of almost one when  $R_{\rm P}$  is calculated keeping only the range between 500 and 600 eV. This is somewhat unexpected, as the higher energies should contain primarily information from the bulk, and should thus cause the  $R_{\rm P}$  to decrease, as is the case for the  $R_P$  calculated for all beams in Fig. 4.8(a<sub>1</sub>). The curves in Fig.  $4.8(b_1)$  present experimental data from the (1|3) spot of the two surface terminations with an enlarged view above 500 eV in Fig. 4.8(b<sub>2</sub>). The energy range in which the comparison of the data takes place becomes smaller as the lower limit increases, making the  $R_{\rm P}$  more sensitive to deviations. From the plots it is visible that the common range for the (1|3) spot becomes very small (down to 36 eV), resulting in an increasing  $R_{\rm P}$  with a strong influence on the overall value.

### 4.5 Conclusion

The focus of this Chapter was the preparation of LSMO(001) films on Nb-doped  $SrTiO_3(001)$  substrates with the PLD technique in order to perform LEED-I(V)measurements on its surfaces.

The prepared LSMO films exhibited two different surface structures, which were clearly distinguishable by their diffraction patterns as well as their appearance in STM. Two fully  $MnO_x$ -terminated surfaces could be prepared by  $MnO_x$ deposition and a following LSMO deposition on top. This surface is characterized by an aperiodic structure in STM, yet showing sharp diffraction spots in the LEED patterns. Repeated cycles of Ar<sup>+</sup> sputtering on the grown films resulted in the  $(\sqrt{2} \times \sqrt{2})$ R45° periodicity with a small share of diffration spots from the aperiodic phase. Increasing sputtering times led to decreasing contributions from the  $MnO_x$  phase to the LEED signal and finally to a surface exhibiting only the

 $(\sqrt{2} \times \sqrt{2})$ R45° periodicity. STM imaging revealed that the surface still retained a small amount of a disordered phase preferentially located at the step edges.

LEED-I(V) measurements were performed on the  $(\sqrt{2} \times \sqrt{2})$ R45° and on the two achieved aperiodic structures. The comparison of the aperiodic structures yielded an overall  $R_{\rm P}$  factor of 0.08, meaning perfect agreement at the sub-picometer level of the surface structures prepared via different routes. Moreover, the two  $MnO_x$ -terminated surfaces were compared to the  $AO_x$ -terminated surface in order to asses the influence of the bulk structure on the I(V) curves. For this, the  $R_{\rm P}$  was employed solely for the quantification of their agreement. By restricting the energy ranges included in the  $R_{\rm P}$  calculations to higher values, the  $R_{\rm P}$  factors decreased with increasing energy limits. As both phases exhibit the same bulk structure, this improvement is because, at high energies, the signal originates more from the bulk.

The experimental data will be compared with structural simulations in the future to enhance the understanding of the chemical nature of the surfaces. Since the LEED-I(V) code only supports simulations of periodic structures, calculating the aperiodic phase presents challenges. Several approaches could address this issue: one option is to simulate the surface using the integer-order spots of the  $(\sqrt{2} \times \sqrt{2})$ R45° structure, incorporating chemical variability in the occupied sites (atoms or vacancies). This could be achieved by applying a weighting factor, which would then be optimized to obtain the best-fit result. The features of the aperiodic structure are always separated by a  $\sqrt{5}$  distance. Therefore, another possibility is to simulate a  $(\sqrt{5} \times \sqrt{5})$  unit cell as an approximant to see if the aperiodic LSMO(001) surface has similar features in the I(V) curves to such a structure. The final and by far the most complex option would be to modify the code to generally enable the treatment of aperiodic structures.

#### Introduction 5.1

The material investigated in this chapter is Cu<sub>2</sub>O, one of the most extensively studied inorganic materials due to its exceptional properties [74, 75]. Cu<sub>2</sub>O finds applications in microelectronics, optics, photocatalysis, and photovoltaics [76]. From an electronic perspective, Cu<sub>2</sub>O is a semiconductor with p-type conductivity. This is rather unusual for binary oxides, as oxygen vacancies — one of the most common defects in oxides — typically act as electron donors, resulting in n-type conductivity. However, the low formation energy of copper vacancies facilitates this p-type conductivity, making Cu<sub>2</sub>O a promising candidate for p-n junctions in oxide electronics [77, 78]. Copper provides catalytically active Cu<sup>+</sup> centers, effective in redox reactions. Its relative low cost compared to noble metals, renders it attractive for catalysis [79]. Given that Cu<sub>2</sub>O is one of the most abundant products of the initial corrosion of copper, an understanding of the surface structure is of particular interest [80]. Copper-based catalysts are already widely used in the water-gas-shift reaction to purify hydrogen gas for fuel cells, and in the synthesis of methanol from syngas (CO, CO<sub>2</sub>, and H) [81]. Moreover, Cu<sub>2</sub>O serves as an effective photocatalyst, capable of splitting water for hydrogen generation under visible-light illumination [82].

In this thesis, the (111) surface of Cu<sub>2</sub>O was studied with the aim of preparing the two known surface terminations, which are the  $(1 \times 1)$  and  $(\sqrt{3} \times \sqrt{3})$ R30° phases [83]. To achieve this, various annealing procedures at different oxygen partial pressures and temperatures were performed. The resulting surfaces were characterized using STM, XPS, and LEED measurements. Throughout the preparation process, several phenomena were observed, including surface artifacts at high oxygen pressures, and a disorder induced by fast cooling rates. These phenomena, along with the surface reconstructions and the challenges encountered during the preparation process, are detailed in Sections 5.3.1–5.3.2. Section 5.3.3 presents the LEED-I(V) measurements recorded on the two surface structures, followed by a discussion of the results in Section 5.4.

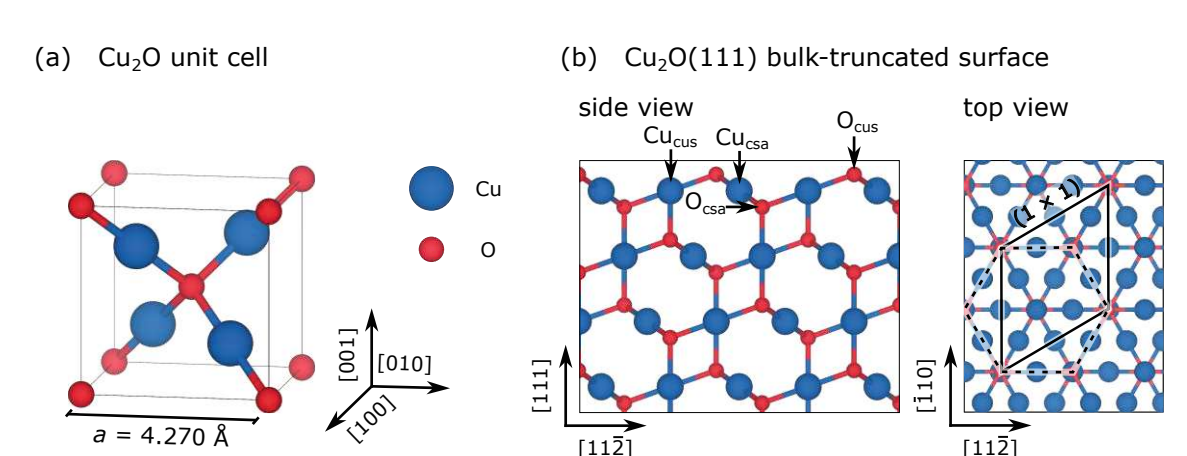


Figure 5.1: Structure model of Cu<sub>2</sub>O. (a) Unit cell in perspective view. The O atoms are surrounded by four Cu atoms (O<sub>csa</sub>), and the Cu atoms have two O atoms as nearest neighbours (Cu<sub>csa</sub>). (b) Cu<sub>2</sub>O(111) bulk-truncated surface in side and top view. Along the [111] direction the bulk shows a stacking of O-4Cu-O trilayers. The (111) surface is formed by coordinatetively saturated and unsaturated Cu and O atoms (labeled as 'csa' and 'cus', respectively), resulting in Cu<sub>6</sub>O<sub>6</sub> rings, where the O atoms are located in the corners of the rings (dashed line). The  $(1 \times 1)$  unit cell is marked with the solid line.

#### 5.2 Bulk structure and surface terminations

Cu<sub>2</sub>O adopts a cubic structure in which each Cu atom is coordinatively saturated by two O atoms, and each O atom by four Cu atoms. These will be referred to as  $Cu_{csa}$  and  $O_{csa}$ , respectively. The structure can be visualized as a bodycentered cubic lattice formed by O ions, with each O ion surrounded by four Cu ions. An illustration of the bulk structure is provided in Fig. 5.1(a). Along the [111] direction, the stacking reveals a repeating sequence of neutral and dipole-free O-4Cu-O trilayers. The (111) surface includes Cu<sub>csa</sub> and O<sub>csa</sub>, and undecoordinated Cu (Cu<sub>cus</sub>) and O (O<sub>cus</sub>) atoms (each missing one nearest neighbor), indicated by the black arrows in Fig. 5.1(b). On the bulk-truncated surface, shown in top view on right side of Fig. 5.1(b), there is an equal number of O<sub>cus</sub> and Cu<sub>cus</sub> ions. The surface exhibits Cu<sub>6</sub>O<sub>6</sub> rings (dashed line), with O ions occupying the corners, and Cu ions located at the centers. These Cu ions are bonded to an O ion in the sublayer [84].

 $Cu_2O(111)$  is known to exhibit two different surface structures, with  $(1 \times 1)$ and  $(\sqrt{3} \times \sqrt{3})$ R30° periodicities [85]. Figure 5.2 presents different models of both terminations. The bulk-truncated surface of Fig. 5.2(a) is labelled as ST (stoichiometric). In Fig. 5.2(b), one can see that removal of each Cu<sub>cus</sub> atom also results in a  $(1 \times 1)$  periodicity (CuD), which leads to a copper-deficient termination. Given that hexagonal symmetry of the surface is consistent with both the ST and CuD sur-

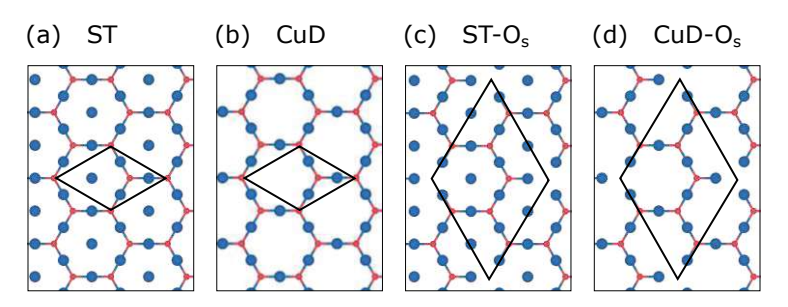


Figure 5.2: Models for the  $(1 \times 1)$  periodicity and vacancy models for the  $(\sqrt{3} \times \sqrt{3})$ R30° reconstruction of  $Cu_2O(111)$ , with unit cells outlined in black. (a) Stoichimetric  $(1 \times 1)$ termination (ST). (b) Copper-deficient termination (CuD) also displaying a  $(1 \times 1)$  periodicity, where each Cu<sub>cus</sub> atom is removed from the surface. (c) and (d)  $(\sqrt{3} \times \sqrt{3})$ R30° reconstruction formed by removing one-third of the O<sub>cus</sub> atoms from the ST or CuD surface, respectively. Reproduced from Ref. 84.

faces, it is not possible to discriminate between them based on qualitative diffraction methods. The  $(\sqrt{3} \times \sqrt{3})$ R30° reconstruction is attributed to an oxygen-deficient surface. This was interpreted as a structure where one-third of the surface O<sub>cus</sub> atoms are removed. This is possible for both the ST (ST-O<sub>S</sub>) and the CuD (CuD-O<sub>S</sub>) terminations. The resulting structures are depicted in Figs. 5.1(c) and 5.1(d), respectively. However, Gloystein et al. [83] have provided a model that matches the experimentally observed STM features found on the surface in previous studies. Herein, the  $(\sqrt{3} \times \sqrt{3})$ R30°-reconstructed surface is characterized by nanopyramids, each consisting of three copper adatoms positioned at the center of every third Cu<sub>6</sub>O<sub>6</sub> ring. These Cu atoms are located above a Cu<sub>cus</sub> atom, with an O ion on top. Figure 5.3(a) illustrates this surface reconstruction (unit cell in black), with the structure of the nanopyramids depicted in side view in Fig. 5.3(b) [84].

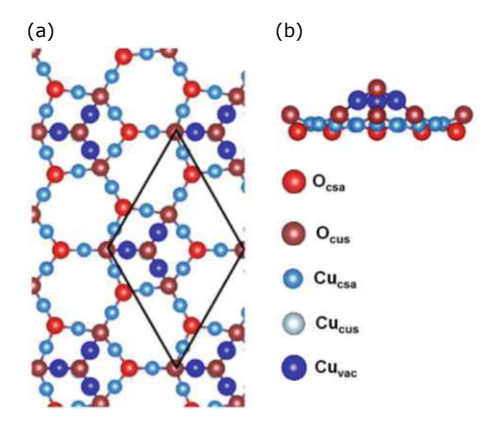


Figure 5.3: Model of the  $(\sqrt{3} \times \sqrt{3})$ R30° reconstruction of Cu<sub>2</sub>O(111) formed by nanopyramids. (a) Top view of the surface. The unit cell is marked in black. The pyramids are located on top of a Cu<sub>cus</sub> in the center of every third Cu<sub>6</sub>O<sub>6</sub> ring, capped with an O atom. (b) Side view of the nanopyramids. Adapted from Ref. 84.



### Sample preparation and results 5.3

The experiments were conducted on a  $6 \times 6 \times 1 \text{ mm}^3$  natural single crystal from SPL. As the crystal had already been used for investigations in another UHV chamber, no ex-situ cleaning to remove polishing residues was necessary, as confirmed by AFM. The sample was mounted for STM measurements as described in Section 2.6.2 and inserted into the UHV chamber.

In-situ preparations aimed to produce homogenous  $(1 \times 1)$  and  $(\sqrt{3} \times \sqrt{3})$ R30° surfaces. To this end, a series of annealing procedures with varying oxygen partial pressures and temperatures were performed. Additionally, some annealing procedures were carried out with an electron-beam heater in the analysis chamber, instead of annealing in the PLD chamber via an IR laser. Moreover, Ar<sup>+</sup> sputtering was performed in some cases. A recipe implemented in the software used for annealing enabled to control the preparation conditions while the temperature was ramped up and down. The oxygen chemical potential was kept approximately constant by alternately adjusting the pressure and temperature. For the temperature adjustment, a step size of 40 °C was used.

Prior to cleaning through Ar<sup>+</sup> sputtering and subsequent O<sub>2</sub> annealing, the sample was test-annealed to check the mounting. XPS was employed to verify the absence of contaminations on the sample surface. This was followed by an annealing study, in which the resulting surface structures were examined by STM. On occasion, XPS and LEED measurements were used for additional characterization. The preparation and characterization procedures revealed a number of different phenomena observed in STM, which are presented in the following sections.

Figure 5.4 illustrates the phase diagram of copper oxide [86]. It was taken as a reference for establishing suitable preparation conditions. Each sample preparation performed in this work is marked in the diagram with a black dot. The area shaded in black outlines the region in which Cu<sub>2</sub>O is presumed to be free of defects. Note that during annealing procedures via electron-beam heating only the pressure was measured; the temperature was not monitored. Instead, the filament current was utilized as a guideline. Previous studies showed that sample temperatures of 300 °C correspond to a current of roughly 1 A. This rough calibration was assumed to provide temperatures for the annealing via electron beam in this diagram. Therefore, the quoted temperatures are only approximations (dependent on the material, and linear correlation assumed, which may not be accurate), and should be treated with caution.



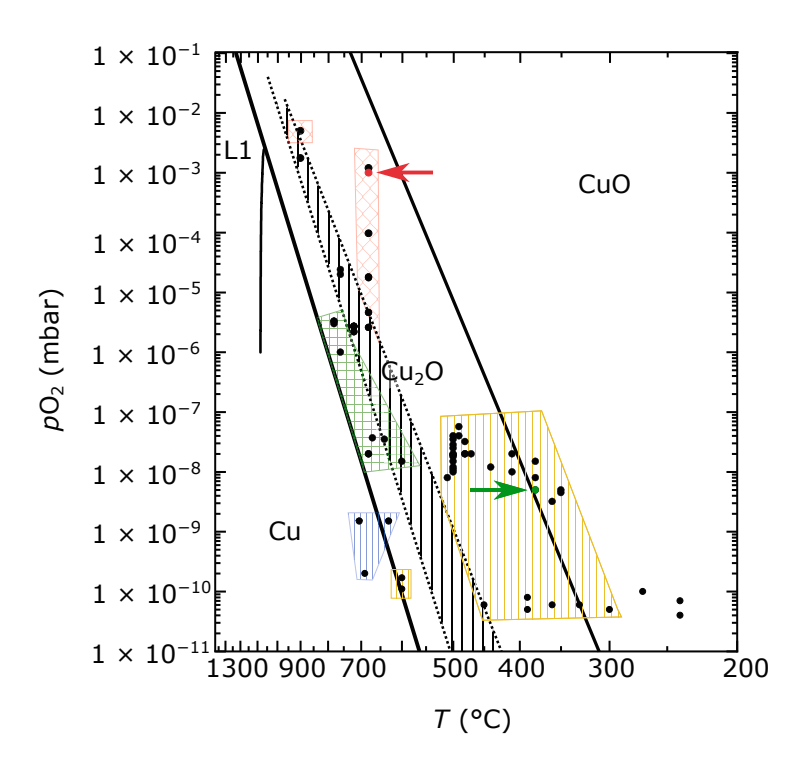


Figure 5.4: Phase diagram of copper oxide. The area shaded in black indicates the conditions in which the Cu<sub>2</sub>O bulk is supposed to be free of defects. Several annealing procedures were carried out, marked by the black dots. In order to prepare the  $(1 \times 1)$ reconstruction, the areas highlighted in red were used. The initial preparations of the  $(\sqrt{3} \times \sqrt{3})$ R30° termination were based on the conditions in the green-hatched area. However, this also resulted in a  $(1 \times 1)$  termination. The remaining dots present the annealing steps carried out after unsuccessful attempts to obtain the  $(\sqrt{3} \times \sqrt{3})R30^{\circ}$  reconstruction. Areas highlighted in yellow led to the  $(\sqrt{3} \times \sqrt{3})$ R30° surface, with a number of additional surface artifacts occurring. The blue area marks the conditions outside of the Cu<sub>2</sub>O phase field, which caused a surface damage through the formation of holes. Conditions not backed with a color resulted in an unchanged structure of the surface. LEED-I(V) measurements were conducted on the  $(1 \times 1)$  (red dot) and  $(\sqrt{3} \times \sqrt{3})$ R30° (green dot) surfaces. The phase-stability regions are adapted from Ref. 86.

The  $(1 \times 1)$  termination is found to be stable under more oxidizing conditions relative to the  $(\sqrt{3} \times \sqrt{3})$ R30° reconstruction, and is observed to exhibit two defect species on the surface: small pyramids and triangular depressions. The pyramids are attributed to the  $(\sqrt{3} \times \sqrt{3})$ R30°-reconstructed surface [83, 85]. As the PLD chamber allows pressures of up to 1 mbar, a first goal was to find conditions that would produce terraces free of nanopyramids. Accordingly, each annealing step was performed in oxygen, with a  $p_{\mathrm{O}_2}$  higher than 1  $\times$  10<sup>-6</sup> mbar, indicated by the red-shaded area in Fig. 5.4.

Previous work [85] on the  $(\sqrt{3} \times \sqrt{3})$ R30°-reconstructed surface stated that this termination occurs at low oxygen partial pressures or after Ar<sup>+</sup>-ion bombardment.



Consequently, the initial preparations were performed within the designated greenhatched area. After struggling to achieve the  $(\sqrt{3} \times \sqrt{3})$ R30° structure [the surface always showed a  $(1 \times 1)$  periodicity, the other conditions in the diagram were used. Each data point in the vellow-shaded area resulted in the  $(\sqrt{3} \times \sqrt{3})$ R30° surface reconstruction. However, a number of different surface artifacts occurred (see Section 5.3.2). Annealing conditions outside of the Cu<sub>2</sub>O phase field, highlighted in blue, led to a damage of the surface structure visible through irregular holes. For annealing procedures that are not backed with a color, the surface structure remained unchanged. In between the various preparation procedures, an annealing step in the 'equilibrium'-region (black) was occasionally performed to restore a defect-free bulk. To this end, temperatures between 720 and 780 °C were employed, with oxygen partial pressures in the  $1.1-3.3 \times 10^{-6}$  mbar range. These conditions generally led to a  $(1 \times 1)$ -terminated surface, and often to a different phase preferentially appearing at the step edges, as reported in Section 5.3.2. Overall, the preparation proved to be challenging, as the results were not reproducible or predictable in most of the cases.

Nevertheless, LEED-I(V) measurements were performed on both the  $(1 \times 1)$ and  $(\sqrt{3} \times \sqrt{3})$ R30° surfaces, obtained by the preparation conditions marked by red and green dots in Fig. 5.4, respectively.

### Characterization of the $(1 \times 1)$ and $(\sqrt{3} \times \sqrt{3}) R30^{\circ}$ 5.3.1surfaces

## $(1 \times 1)$ surface

A representative LEED pattern of a  $(1 \times 1)$ -structured surface at 100 eV is shown in Fig. 5.5(a), with the unit cell outlined in black. Figure 5.5(b) depicts an overview STM image of the sample exhibiting the  $(1 \times 1)$  termination. The terraces appear large and flat, with apparent step heights of approximately 2.5 Å. Two distinct species of defects, highlighted in white, were observed on the surface, as seen in the high-resolution STM image of Fig. 5.5(c). The defects include bright protrusions the pyramids (dashed triangle) — suggested to correspond to three copper atoms with an oxygen atom on top [84]. The dark triangular depressions (solid triangles), are suggested to originate from copper vacancies [87]. These triangular holes sometimes showed an additional, triangular bright feature inside them (white arrow), dependent on the tip resolution. The appearance of the holes was found to depend on the bias voltage applied to the sample. Figures 5.5(d) and 5.5(e) illustrate



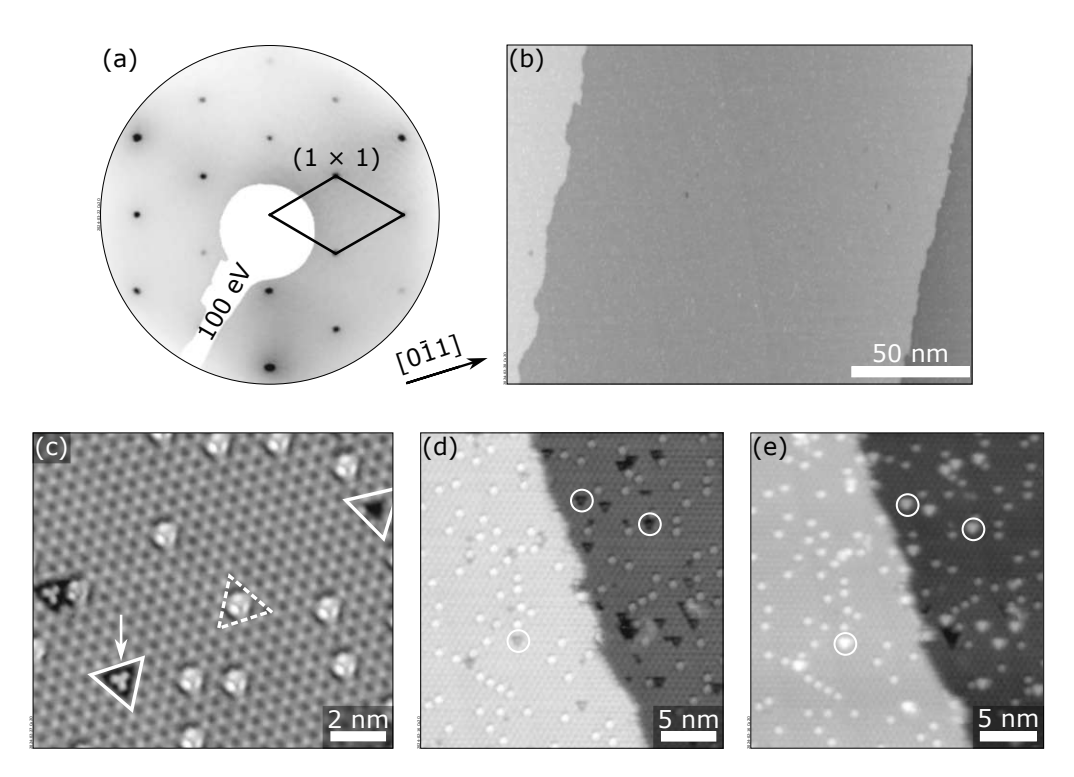


Figure 5.5: Characterization of the  $(1 \times 1)$ -ordered Cu<sub>2</sub>O(111) surface. (a) LEED pattern at 100 eV, showing the  $(1 \times 1)$  diffraction pattern. The unit cell is marked in black. (b) Overview STM image, with large flat terraces. (c) High-resolution STM image with defects on the surface. Bright protrusions, which are referred to as pyramids (dashed triangle), and dark holes with and without a bright feature inside (solid triangle) are visible. The pyramids are attributed to three copper adatoms and one oxygen atom [see Fig. 5.3, and the depressions to copper vacancies. (d),(e) Detailed STM images of the same scanning location on the sample scanned with different sample bias voltages. The holes from panel (c) (white circles) appear as depressions for voltages lower than +1 V, and as bright protrusions for voltages larger than +1 V. (b)  $U_{\rm b} = +1.7$  V,  $I_{\rm t} = 0.34$  nA,  $200 \times 110 \text{ nm}^2$ ; (c)  $U_{\rm b} = +1.0 \text{ V}$ ,  $I_{\rm t} = 0.20 \text{ nA}$ ,  $13 \times 10 \text{ nm}^2$ ; (d)  $U_{\rm b} = +0.8 \text{ V}$ ,  $I_{\rm t} = 0.25 \text{ nA}, 27 \times 30 \text{ nm}^2$ ; (e)  $U_{\rm b} = +2.2 \text{ V}, I_{\rm t} = 0.19 \text{ nA}, 27 \times 29 \text{ nm}^2$ .

the same location on the surface scanned at different voltages. At voltages approximately lower than +1 V, the holes (white circles) appeared dark [Fig. 5.5(d)]. However, when higher voltages, such as 1.68 V, were applied, the holes became bright [Fig. 5.5(e)].

During the preparation procedure of the  $(1 \times 1)$  periodicity, the aim was to prepare a pristine  $(1 \times 1)$  surface (free of pyramids), as the pyramids are assumed to form the  $(\sqrt{3} \times \sqrt{3}) R30^{\circ}$  reconstruction. However, even at very high  $p_{O_2}$  of  $5 \times 10^{-3}$  mbar (T = 900°C), a small percentage of  $2.9 \pm 0.4\%$  of the unit cells remained covered with pyramids. As the LEED patterns did not show any additional spots of the  $(\sqrt{3} \times \sqrt{3})$ R30° reconstruction, LEED-I(V) was conducted (for the preparation conditions see red dot in Fig. 5.4).



# $(\sqrt{3} \times \sqrt{3})$ R30° reconstruction

The characteristic LEED pattern (100 eV) of the  $(\sqrt{3} \times \sqrt{3})$ R30° reconstruction is illustrated in Fig. 5.6(a). The unit cell of the  $(\sqrt{3} \times \sqrt{3})$ R30° reconstruction is outlined by the solid line, and that of the  $(1 \times 1)$  termination by the dashed line. Figure 5.6(b) depicts a large-area STM image of the  $(\sqrt{3} \times \sqrt{3})$ R30°-reconstructed surface, with flat and large terraces. Similarly to the  $(1 \times 1)$ -structured surfaces (Section 5.5), the terraces are separated by steps with a height of 2.5 Å. During the investigation of the surface, defects shown in Fig. 5.6(c) occurred. Holes resulting from missing pyramids (white arrow), and disordered regions (white oval) could be

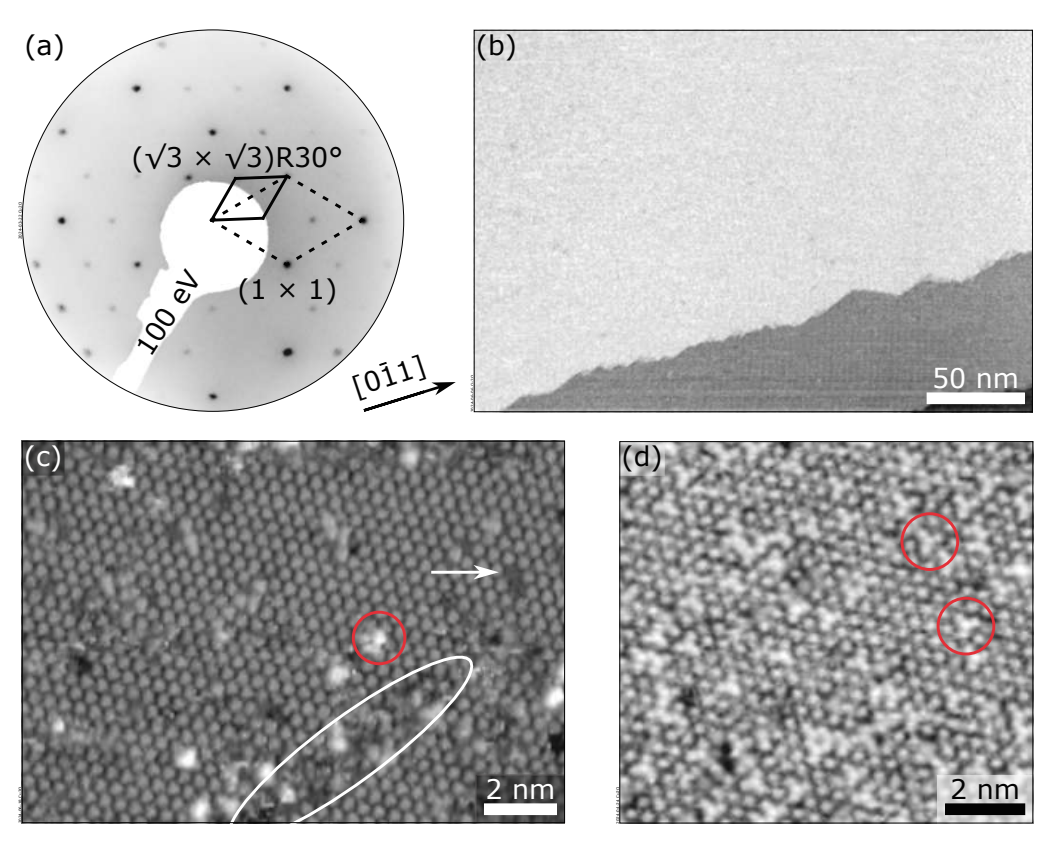
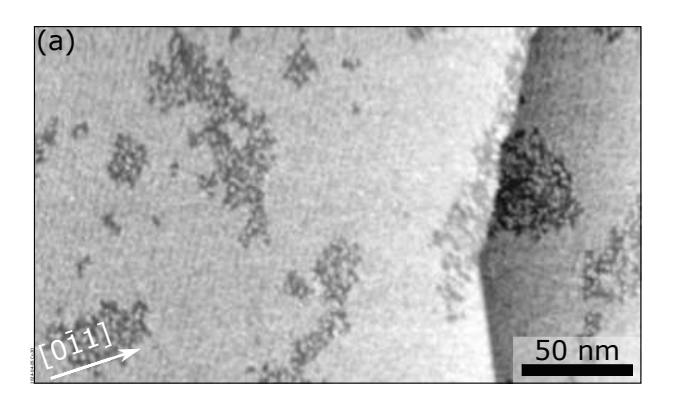


Figure 5.6: Characterization of the  $(\sqrt{3} \times \sqrt{3})R30^{\circ}$  reconstruction of  $Cu_2O(111)$ . (a) LEED pattern at 100 eV with the  $(\sqrt{3} \times \sqrt{3})$ R30° (solid line) and the  $(1 \times 1)$  (dashed line) unit cells outlined. (b) Overview STM image of the surface. The terraces are flat and large. (c) Detailed STM image of the surface and occurring defects. The surface is covered with pyramids, which have been observed as defects on the  $(1 \times 1)$  termination (see Fig. 5.5). Bright features (red circles) explained by a closer packing of the pyramids, disordered regions (white oval), and holes resulting from missing pyramids occurred. (d) Same features as the bright adsorbate-like features in panel (c), both marked with red circles, but with a different appearance, due to a different tip. (b)  $U_{\rm b} = +2.6 \text{ V}$ ,  $I_{\rm t} = 0.71 \text{ nA}$ , 290 × 195 nm<sup>2</sup>; (c)  $U_{\rm b} = +2.1$  V,  $I_{\rm t} = 0.20$  nA,  $35 \times 25$  nm<sup>2</sup>; (d)  $U_{\rm b} = +2.8$  V,  $I_{\rm t} = 0.10 \text{ nA}, 20 \times 20 \text{ nm}^2.$ 

observed. Additionally, the surface exhibited bright features (red circle), sometimes appearing as adsorbate-like features [Fig. 5.6(c)], and sometimes appearing in a distinct shape, as seen in Fig. 5.6(d), where they are also highlighted by red circles. Their appearance was dependent on the tip reolution. These features have been attributed to pyramids having a closer packing [85]. In general, STM measurements performed on the  $(\sqrt{3} \times \sqrt{3})$ R30° reconstruction turned out to be considerably more challenging than those performed on the  $(1 \times 1)$  termination, due to the presence of more defects.

The preparation of the  $(\sqrt{3} \times \sqrt{3})$ R30° reconstruction was carried out in a wide range of temperatures and pressures. This resulted in surfaces exhibiting partially reconstructed  $(\sqrt{3} \times \sqrt{3})R30^{\circ}$  areas observed in STM, such as the one shown in the overview STM image of Fig. 5.7(a). Figure 5.7(b) depicts a detailed image of an area with missing pyramids; the  $(1 \times 1)$  surface can be seen in the holes. Each  $(\sqrt{3} \times \sqrt{3})$ R30°-reconstructed surface occurred at temperatures below 500 °C, except for two preparation conditions at pressures below  $1 \times 10^{-9}$  mbar. Moreover, for prepared surfaces that underwent re-oxidation during the preceding stage, the formation of the  $(\sqrt{3} \times \sqrt{3})$ R30° reconstruction was not observed. LEED-I(V)measurements on the  $(\sqrt{3} \times \sqrt{3})$ R30° reconstruction were performed on a surface almost fully covered with pyramids (for the preparation conditions see green dot in Fig. 5.4).



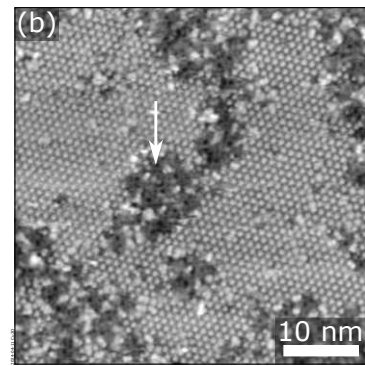


Figure 5.7: Mostly  $(\sqrt{3} \times \sqrt{3})$ R30°-reconstructed surface  $(p_{O_2} = 2 \times 10^{-8} \text{ mbar},$ T = 480 °C). (a) Overview STM image with dark areas not covered by pyramids. (b) Detailed STM image of the areas with missing pyramids (white arrow). The  $(1 \times 1)$  surface can be seen underneath. (a)  $U_b = +2.4 \text{ V}$ ,  $I_t = 0.17 \text{ nA}$ ,  $300 \times 157 \text{ nm}^2$ ; (b)  $U_b = +2.5 \text{ V}$ ,  $I_{\rm t} = 0.28 \text{ nA}, 47 \times 47 \text{ nm}^2$ 



# 5.3.2 Other effects observed during sample preparation Different phase occurring in STM under high $p_{O_2}$

For annealing procedures with high oxygen pressures (>  $1 \times 10^{-6}$  mbar), a different phase was observed in STM. This only occurred for  $(1 \times 1)$  surfaces, with annealing temperatures above 680°C (but not for every annealing procedure at these conditions). Figure 5.8 depicts a series of STM images of surface preparations under conditions in the aforementioned region. The non- $(1 \times 1)$  phase is occasionally located on the terraces, and sometimes located at the step edges. In most of the cases, only a very small fraction of the surface (< 1.5%) assumed this phase. In Fig. 5.8(a<sub>1</sub>), an overview STM image of an area at the surface exhibiting a large coverage with this additional phase can be seen  $(p_{O_2} = 1.2 \times 10^{-3} \text{ mbar}, T = 680^{\circ}\text{C}).$ The non- $(1 \times 1)$  phase appears in the form of equidistant 'rods' with a periodicity of  $\approx 3.83$  nm along the height variation. Additionally, a defined single 'rod' at the step edge (white arrow) located along the [110] direction, and another non- $(1 \times 1)$ phase, indicated by the black arrow, occur. The periodic arrangement of the rods in panel (a<sub>1</sub>) is seen in detail in the STM image of Fig. 5.8(a<sub>2</sub>). The rods do not seem to have a certain width. In between them, patches with the  $(1 \times 1)$  structure and holes with a depth of up to 0.25 nm are visible. A similarly appearing phase was observed at another surface preparation illustrated in Fig. 5.8(b) ( $p_{\rm O_2} = 9.8 \times 10^{-5}$  mbar, T = 680°C). Here, the non-(1 × 1) phase is located at the step edge with a periodicity along the height variation of  $\approx 3.31$  nm. A closer look at the  $(1 \times 1)$  surface in the vicinity of the phase shows that it exhibits an undulation of the height with a periodicity of 4.56 nm, indicated by the white arrows. Figure 5.4(c) gives an example of the phase appearing as a single 'rod' in the middle of a terrace (white arrow) ( $p_{O_2} = 1.2 \times 10^{-3}$  mbar, T = 680°C). It is evident that the edges of the artifact match with the low-index directions of the pristine  $(1 \times 1)$  surface. Further, a height modulation (white arrows) with a smaller periodicity of 1.18 nm as the one determined in Fig.5.8(b) can be seen. The periodicity is 2.15 times larger than the lattice vectors of the Cu<sub>2</sub>O(111) surface, and exhibits a rotation by 24° with respect to the low-index direction. Data analysis showed that it is commensurate with the Cu<sub>2</sub>O lattice at least in one direction. Finally, in Fig. 5.8(d), the mostoften observed case is shown ( $p_{O_2} = 9.7 \times 10^{-5}$  mbar, T = 680°C). The step edges are covered by a little amount of the different phase indicated by the white arrows. This was observed for  $p_{O_2}$  higher than  $1 \times 10^{-6}$  mbar (but not always). Moreover, the non- $(1 \times 1)$  phases can either appear as a depression, as seen in Fig. 5.8(a<sub>1</sub>),

or as protruding phase, as seen in Fig. 5.8(b). Generally, a larger amount of the phase appeared for higher  $p_{O_2}$ , and the differently appearing non- $(1 \times 1)$  phases can coexist on the same surface.

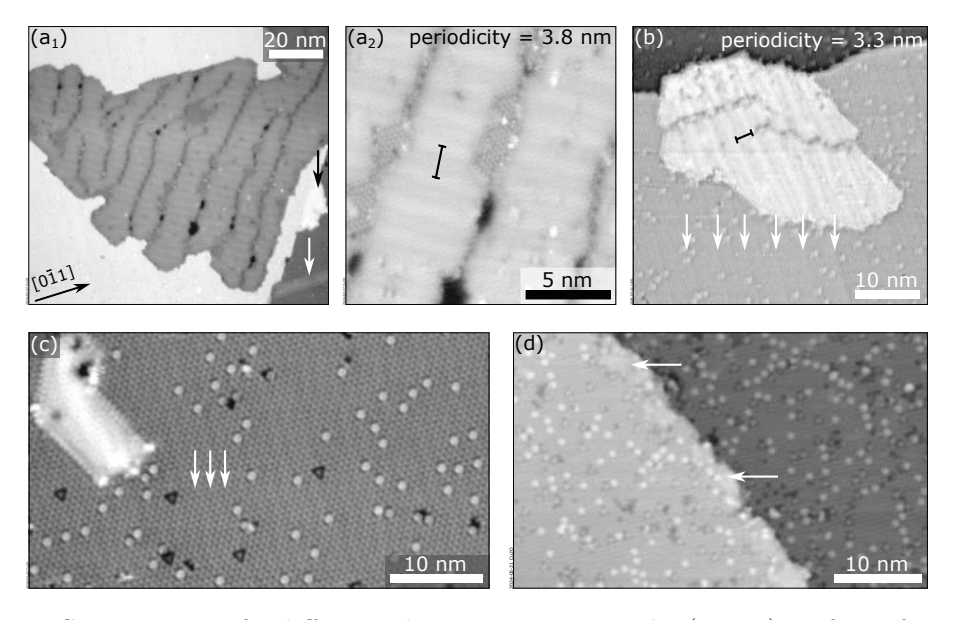


Figure 5.8: STM images of a different phase appearing on the  $(1 \times 1)$  surface after annealing in  $p_{\rm O_2}$  higher than  $1\times 10^{-6}$  mbar. (a<sub>1</sub>) Overview STM image of a surface exhibiting a large-area coverage with the non-(1 × 1) phase  $(p_{O_2} = 1.2 \times 10^{-3} \text{ mbar}, T = 680^{\circ}\text{C}).$ Additionally, a single 'rod' along the  $[0\bar{1}1]$  direction (white arrow) and a less defined phase (black arrow) at the step edge are present. (a<sub>2</sub>) Detailed view of the same location as in panel (a<sub>1</sub>). The phase consists of 'rods' separated by  $\approx 3.84$  nm. (b) Phase occurring for a differently prepared surface at the step edge ( $p_{O_2} = 9.8 \times 10^{-5}$  mbar, T = 680°C). For clearer display, the image is processed with a high-pass filter to enhance the contrast. It shows again a similar periodicity of 3.31 nm as the phase in panel (a<sub>2</sub>). The white arrows indicate an undulation of the  $(1 \times 1)$  surface in the vicinity of the surface artifact (white arrows) with a periodicity of 4.56 nm. (c) Single 'rod' located at a terrace. The phase exhibits sharp edges, which match the lattice directions of the  $(1 \times 1)$  structure  $(p_{\rm O_2} = 1.2 \times 10^{-3} \text{ mbar}, T = 680^{\circ} \text{C})$ . The surface shows again undulations (white arrows) with a smaller periodicity of 1.18 nm as the one observed in panel (b). The periodicity of the undulations is 2.15 times larger than the lattice constant of the Cu<sub>2</sub>O(111) surface, with a rotation of 24° to the low-index direction. (d) Most common case, where the phase covers only small parts of the step edges, as indicated by the white arrows  $(p_{\rm O_2} = 9.7 \times 10^{-5} \text{ mbar}, T = 680^{\circ}\text{C}). (a_1) U_{\rm b} = +1.4 \text{ V}, I_{\rm t} = 0.30 \text{ nA}, 113 \times 105 \text{ nm}^2;$ (a<sub>2</sub>)  $U_{\rm b} = +1.3 \, {\rm V}, \, I_{\rm t} = 0.16 \, {\rm nA}, \, 33 \times 33 \, {\rm nm}^2; \, ({\rm b}) \, U_{\rm b} = +1.2 \, {\rm V}, \, I_{\rm t} = 0.12 \, {\rm nA}, \, 50 \times 47 \, {\rm nm}^2;$ (c)  $U_{\rm b} = +1.1~{\rm V},\, I_{\rm t} = 0.19~{\rm nA},\, 50\times25~{\rm nm}^2;$  (d)  $U_{\rm b} = +2.2~{\rm V},\, I_{\rm t} = 0.12~{\rm nA},\, 47\times30~{\rm nm}^2$ 



### Disorder induced by fast cooling rates

As already mentioned in Section 5.3, in addition to utilizing the IR laser for annealing in the PLD chamber, an electron-beam heating in the analysis chamber was employed, which allowed annealing in UHV with a base pressure of  $4 \times 10^{-11}$  mbar. This annealing method was only used to prepare the  $(\sqrt{3} \times \sqrt{3})$ R30° reconstruction. The temperature regulation of the annealing procedures was performed manually, by direct control of the current of the heating filament, based on a predetermined approximate calibration (different from the PID control of the PLD chamber). Samples annealed via this method showed large regions with disorder in the pyramid arrangement. The typical cooling rates used while annealing in the PLD were 40 °C/min. In the case of heating via electron beam, ramp rates at least three times as large ( $\approx 120$  °C/min) were applied. Figure 5.9(a<sub>1</sub>) depicts an STM image after annealing with the electron-beam heater ( $p_{\rm O_2} = 1.1 \times 10^{-11}$  mbar, I=2 A,  $T\approx 600$  °C). It shows some ordered regions, but also areas with a

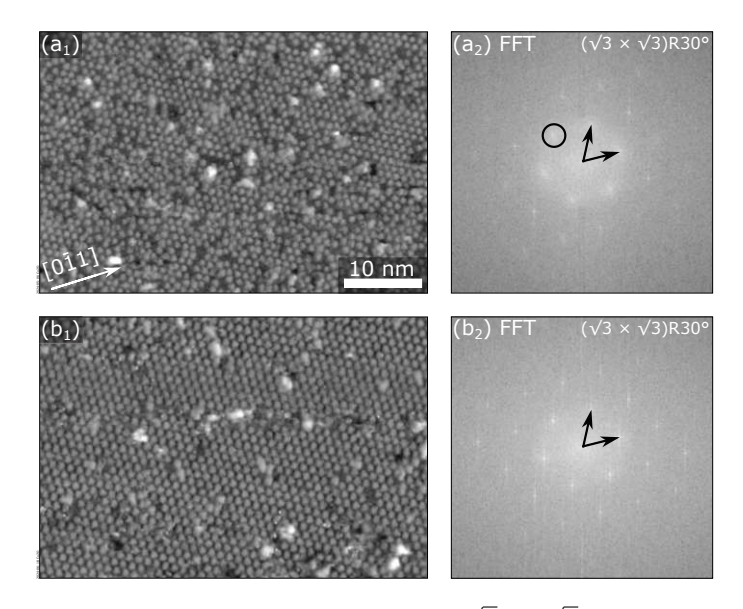


Figure 5.9: Comparison of STM images of the  $(\sqrt{3} \times \sqrt{3})$ R30° surface structure obtained by different cooling rates. (a<sub>1</sub>) High-resolution STM image of the  $(\sqrt{3} \times \sqrt{3})$ R30°reconstructed surface with a fast cooling rate of  $\approx 120$  °C/min ( $p_{O_2} = 1.1 \times 10^{-11}$  mbar, I=2 A corresponding to  $\approx 600$  °C). The structure exhibits large areas with disorder. (a<sub>2</sub>) Corresponding Fourier transform of the image in panel (a<sub>1</sub>). The first-order spots are blurred. (b<sub>1</sub>) Detailed STM image of the  $(\sqrt{3} \times \sqrt{3})$ R30° reconstruction with a slow cooling rate (40 °C/min,  $p_{O_2} = 5 \times 10^{-9}$  mbar, T = 350 °C). A highly ordered surface can be seen. (b<sub>2</sub>) Fourier transform of the image in panel (b<sub>1</sub>), with sharp spots. The reciprocal-lattice vectors of the  $(\sqrt{3} \times \sqrt{3})R30^{\circ}$  unit cell are outlined by black arrows. (a<sub>1</sub>)  $U_{\rm b} = +2.6$  V,  $I_{\rm t} = 0.09$  nA,  $50 \times 30$  nm<sup>2</sup>; (b<sub>1</sub>)  $U_{\rm b} = +2.1$  V,  $I_{\rm t} = 0.41$  nA,  $50 \times 30 \text{ nm}^2$ .

non-periodic pyramid arrangement. Figure 5.9(a<sub>2</sub>) depicts the corresponding Fourier transform. The reciprocal-lattice vectors of the  $(\sqrt{3} \times \sqrt{3})R30^{\circ}$  reconstruction are outlined by the black arrows. It is visible that the fractional-order spots (black circles) are blurred. The integer-order spots are sharp. In Fig. 5.9(b<sub>1</sub>), a detailed STM image of the  $(\sqrt{3} \times \sqrt{3})$ R30° surface achieved through PLD annealing can be seen ( $p_{\rm O_2}=5\times 10^{-9}$  mbar,  $T=380{\rm ^{\circ}C}$ ). The surface displays some defects, yet the pyramid structure is highly ordered. The Fourier transform of this STM image in Fig. 5.9(b<sub>2</sub>) illustrates distinct, sharp spots for both integer and fractional orders.

### Significant changes in the preparation conditions

During the preparation procedures of the  $(\sqrt{3} \times \sqrt{3})R30^{\circ}$  reconstruction, the annealing conditions were changed between oxidizing or reducing conditions. The chemical potential of oxygen  $(\mu_{\rm O})$  is defined as

$$\mu_{\rm O}(T, p_{\rm O_2}) = \frac{1}{2} \mu_{\rm O_2}(T, p_{\rm O_2}) = \frac{1}{2} \mu_{\rm O_2}^0(T) + k_{\rm B}T \ln\left(\frac{p_{\rm O_2}}{p_0}\right) ,$$
 (5.1)

where  $k_{\rm B}$  is Boltzman's constant,  $p_0 = 1$  mbar, and T the absolute temperature in Kelvin [88]. Abrupt changes between two subsequent annealing steps commonly resulted in depressions on the terraces, shown in a large-area STM image of a  $(1 \times 1)$ surface in Fig. 5.10(a) ( $\Delta\mu_{\rm O}=0.16~{\rm eV}$  [89]). The STM image in Fig. 5.10(b) illustrates such a depression in more detail. Figure 5.10(c) shows the height profile along the black line in Fig. 5.10(c). The step height of such layers is approximately 2.8 Å, which aligns with the typical height of a single step observed on the sample.

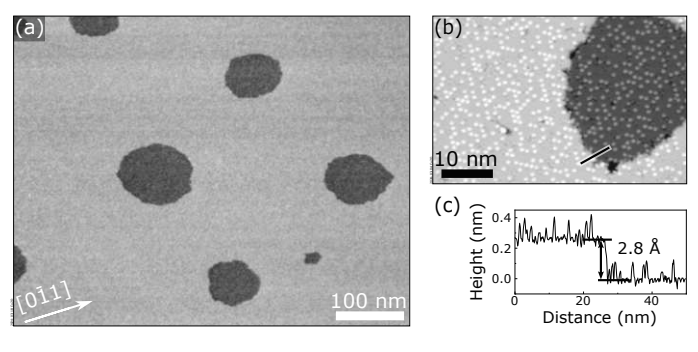


Figure 5.10: One-layer-deep vacancy islands after abrupt changes in the chemical potential of oxygen between two subsequent annealing steps. (a) Overview STM image showing the depressions located on a flat terrace. (b) Detailed STM image of one depression. (c) Height profile of the step along the black line in panel (b). The step height of the depression is 2.8 Å, which is of the same order of magnitude as the typical step heights between neighboring terraces. (a)  $U_{\rm b} = +3.2 \text{ V}$ ,  $I_{\rm t} = 0.8 \text{ nA}$ ,  $300 \times 235 \text{ nm}^2$ ; (b)  $U_{\rm b} = +1.2 \text{ V}$ ,  $I_{\rm t} = 0.06 \text{ nA}$ ,  $50 \times 40 \text{ nm}^2$ .



Inside the vacancy islands, the structure is identical to that of the terraces.

#### LEED-I(V) measurements 5.3.3

The investigations through LEED revealed that the diffraction spots disappear for energies above 240 eV. Therefore, reasonable LEED-I(V) measurements could only be performed in an energy range of 20–300 eV. For both the  $(1 \times 1)$  structure and the  $(\sqrt{3} \times \sqrt{3})$ R30° reconstruction, LEED-I(V) curves were recorded. As the structural calculations are still in progress, no model can be presented at present. Instead, the quality of the acquired data, particularly concerning sample alignment, was assessed. For this, the I(V) curves of symmetry-equivalent spots were compared. As outlined in Section 2.5, three measurements were conducted at different sample-screen distances for each surface structure. The used manipulator in the UHV chamber only allows for the adjustment of two of the three spatial angles. Consequently, some diffraction spots that are supposed to be symmetryequivalent are not equivalent, due to a non-perpendicular incidence of the electron beam on the sample. Figure 5.11 shows the diffraction patterns and the I(V) curves of selected equivalent diffraction spots for both the  $(1 \times 1)$  (left column) and the  $(\sqrt{3} \times \sqrt{3})$ R30° surface (right column). In the diffraction patterns of Figs. 5.11(a<sub>1</sub>) and  $(b_1)$ , the spots for which the subsequent plots display the I(V) curves are marked with green (low energies) and yellow (high energies) circles. Furthermore, some mirror planes are indicated by black dashed lines, for a better understanding of the symmetry properties. The arrows between the patterns demonstrate the adjustable directions in the experimental setup. The LEED-I(V) measurements illustrated in Figs. 5.11(a<sub>2</sub>)-(b<sub>3</sub>) represent the data acquired closest to the LEED screen in red (front), the one in the middle in blue, and the data recorded furthest away in black (back). Additionally, one curve from a diffraction spot that should be equivalent in terms of a perpendicular incidence of the electron beam is added (outlined by the black dotted lines). The displayed diffraction spots are labeled in each plot. Figures. 5.11(a<sub>2</sub>) and 5.11(b<sub>2</sub>) represent the I(V) curves for both surfaces at low energies. In Figs. 5.11(a<sub>3</sub>) and 5.11(b<sub>3</sub>), symmetry-equivalent spots of the two surfaces at higher energies are shown. Each plot demonstrates that the intensity maxima of the symmetry-equivalent diffraction spots are closely aligned, as indicated by the vertical lines. Additionally, the curves show a strong resemblance to one another. The intensity maxima of the dotted curves (representing the spots that are expected to be symmetry-equivalent for perpendicular incidence) clearly deviate from the corresponding other curves in the respective panels.



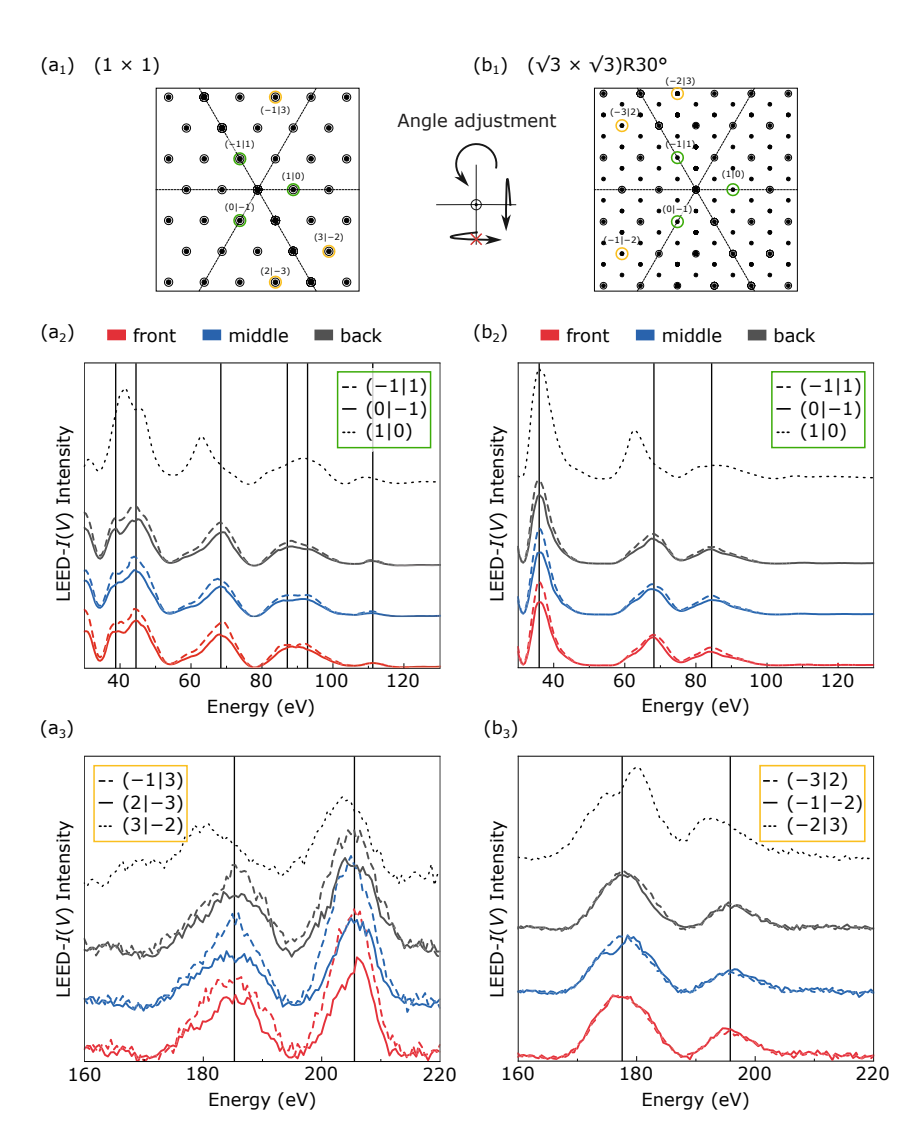


Figure 5.11: Diffraction patterns and comparison of selected symmetry-equivalent diffraction spots obtained from the LEED-I(V) curves recorded on the prepared  $Cu_2O(111)$ The  $(1 \times 1)$  surface is shown in the panels of the left column and the  $(\sqrt{3} \times \sqrt{3})R30^{\circ}$  reconstruction in the panels of the right column. (a<sub>1</sub>), (b<sub>1</sub>) Diffraction patterns of the two surfaces, with the used symmetry-equivalent spots representaive for low and high energies, marked with green and yellow circles, respectively. Some of the mirror planes are indicated by black dashed lines.  $(a_2)$ - $(b_3)$  I(V) curves of two symmetryequivalent spots each recorded at three different sample-screen distances. The smallest distance (front) is represented in red, the middle in blue, and the largest distance in black (back). A third diffraction spot is added, to demonstrate the non-perpendicular incidence of the electron beam (outlined with the dotted black lines).  $(a_2)$ ,  $(b_2)$  I(V)curves of two symmetry-equivalent spots of the  $(1 \times 1)$  and the  $(\sqrt{3} \times \sqrt{3})$ R30° surface, respectively, at low energies. (a<sub>3</sub>), (b<sub>3</sub>) Measurements of symmetry-equivalent spots of the two surfaces representative for higher energies. Each of the four plots illustrates symmetry-equivalent diffraction spots, with positions of the intensity maxima very similar (vertical black lines), and curves that resemble one another. The dotted curves corresponding to the non-equivalent spots (due to an incidence angle of the electron beam different from 90°) clearly deviate in their positions of the intensity maxima.

#### 5.4 Discussion

The results presented in this chapter on the preparation of the  $Cu_2O(111)$  surface partially align with findings from previous studies, particularly in terms of the observed defects, such as the pyramids and the Cu vacancies, and their appearance [83, 85, 87]. Additionally, the varying contrast of Cu vacancies while maintaining the contrast of the pyramids under different sample-bias voltages has also been observed. Ly et al. [90] suggest that Cu vacancies are negatively charged, which would explain their appearance as dark when tunneling into empty states and bright when tunneling into filled states. The pyramids are not charged and thus remain unaltered [90]. Given that all STM measurements presented in this work were acquired with positive sample-bias voltage, only empty states were probed. According to the interpretation from Ref. 90, a change in contrast should not have been visible. A detailed analysis of the energy-dependent density of states is probably needed to explain the bias-dependent contrast observed.

In this work, a fully  $(1 \times 1)$ -structured surface without nanopyramids associated with the  $(\sqrt{3} \times \sqrt{3})$ R30° reconstruction could not be obtained. Even at very high oxygen partial pressures  $(1 \times 10^{-3} \text{ mbar}) \approx 3\%$  of the surface unit cells were occupied by nanopyramids. A possible explanation for this may be charged, extrinsic dopants (relative to Cu) in the vicinity of the surface that reduce the surface. The pyramids could be related to the dopants and are therefore always present on the  $(1 \times 1)$  surface. Normal-emission XPS measurements did not detect any contaminants. However, this does not rule out the presence of a small amount of extrinsic dopants, as such coverage could be achieved with minimal quantities. STM measurements revealed the formation of a distinct phase after annealing at high oxygen pressures [Fig. 5.8]. This non- $(1 \times 1)$  phase appears as rod-like structures, with a modulation of the apparent height with periodicity in the 3.2–3.8 nm range. Moreover, a height modulation on the otherwise pristine  $(1 \times 1)$  surface was observed. An explanation could be that the high oxygen pressures resulted in a defective and distorted bulk structure, which causes the surface layers to adapt the bulk structure under undulation. A distortion of the bulk structure could also be the reason for the vanishing intensity of the LEED diffraction spots at energies above 240 eV, given that higher-energy electrons generate a signal coming from deeper layers [17]. However, this needs further investigation for a correct interpretation.

Throughout the preparation, the surface exhibited one-layer-deep vacancy islands after significant changes in the preparation conditions between two subse-



quent annealing steps. This results from Cu atoms migrating to or from the bulk to adapt to the annealing conditions. Given that the structure within the vacancy islands is identical to the overall surface structure, these did not affect the LEED measurements.

The  $(\sqrt{3} \times \sqrt{3})$ R30° reconstruction has proven to be more challenging to prepare than first assumed. Despite repeated attempts to prepare a surface which is  $(\sqrt{3} \times \sqrt{3})$ R30°-reconstructed, this could not be achieved using annealing procedures under pressures in the order of  $10^{-8}$  mbar, and temperatures exceeding 600 °C. Gloystein et al. [83] reported a remaining  $(\sqrt{3} \times \sqrt{3})$ R30° LEED pattern for conditions of up to  $10^{-4}$  mbar of  $O_2$  but at a temperature of 530 °C, lower than the one employed in this work. Such high oxygen pressures always resulted in a  $(1 \times 1)$  structure throughout this work. A successful preparation was obtained after performing annealing under UHV conditions (5  $\times$  10<sup>-9</sup> mbar) and drastically reducing the temperature to 350 °C. The following annealing procedures always displayed a  $(\sqrt{3} \times \sqrt{3})$ R30° periodicity in STM, as long as the temperature was below 500  $^{\circ}$ C and no previous reoxidation step at pressures in the  $10^{-6}$  mbar range (and  $T \geq 680$  °C) was performed. This behavior gives rise to the conclusion that the focus was initially misplaced, with greater attention paid to lower pressures than to lower temperatures, relative to the  $(1 \times 1)$  preparation. An instability of the  $(\sqrt{3} \times \sqrt{3})R30^{\circ}$  reconstruction at higher temperatures has already been observed [85], which probably indicates that this surface reconstruction is metastable. Moreover, the failure to prepare the  $(\sqrt{3} \times \sqrt{3})$ R30° reconstruction after oxidation indicates that the condition of the bulk structure, along with the annealing history of the sample, plays a crucial role in determining the surface reconstruction one aims to achieve.

A disorder in the pyramid arrangement of the  $(\sqrt{3} \times \sqrt{3})$ R30° reconstruction has previously been observed [83, 85]. Within the investigations in this thesis, a correlation between the cooling rate and the disorder could be shown. Annealing procedures with fast cooling rates ( $\approx 120$  °C/min) exhibited more areas with disorder than with slow cooling rates of 40 °C/min, suggesting that the nanopyramid constituents are mobile during cooling and preferentially form ordered arrangements given a slow enough tempering. When cooling is too fast, the migration of the pyramids is impeded, which quenches the arrangement and results in a disorder. The Fourier transform of the disordered structure in Fig. 5.9(a<sub>2</sub>) depicts fractional-order maxima which are faded. This is a known phenomenon, where short coherence lengths in the structure lead to a broadening of the spots. Integer-



order spots, however, remain sharp. This is because the structure underneath is a well-ordered  $(1 \times 1)$  surface, and each nanopyramid occupies a  $(1 \times 1)$  site, still resulting in sharp integer-order maxima.

The LEED-I(V) curves recorded on the  $(1 \times 1)$  and on the  $(\sqrt{3} \times \sqrt{3})$ R30° surfaces were evaluated to asses the quality of the data. For both low and high energies the data sets exhibit correlating positions of intensity maxima for symmetryequivalent spots [Fig. 5.11]. Moreover, all curves exhibit very similar shape. This agreement demonstrates a precise sample alignment and confirms high-quality data. The third beam that was added to the plots demonstrates the impact of a nonperpendicular electron-beam incidence. Since the positions of the intensity maxima do not align with those of the other curves, this deviation needs to be accounted for during the calculations.

#### Conclusion 5.5

The objective of this chapter was to prepare and characterize the  $Cu_2O(111)$  surface. A variety of annealing procedures were performed at different oxygen partial pressures and temperatures. As a result,  $(1 \times 1)$  and  $(\sqrt{3} \times \sqrt{3})$ R30° surfaces could be achieved, occasionally accompanied by surface artifacts. LEED-I(V) measurements were conducted on both the  $(1 \times 1)$ -ordered surface and the  $(\sqrt{3} \times \sqrt{3})$ R30° reconstruction.

During the preparation procedure of the  $(1 \times 1)$ -ordered surface, the aim was to prepare a surface without nanopyramid defects, which are attributed to the  $(\sqrt{3} \times \sqrt{3})$ R30° reconstruction. However, this was not fully achieved, as approximately 3% of the pristine surface remained covered with pyramids, with any chosen preparation method. Additionally, STM revealed the presence of a different phase on the surface appearing at high oxygen partial pressures, accompanied by surface undulations that may be indicative of a defective bulk structure. LEED investigations showed the disappearance of diffraction spots above 240 eV, possibly due to these bulk defects, as the signal at higher energies originates from deeper layers within the material. To corroborate this assumption, further investigation is necessary.

Although the preparation of the  $(\sqrt{3} \times \sqrt{3})$ R30°-reconstructed surface is generally considered straightforward, it proved difficult to achieve a homogenous sample in this work. Several unsuccessful attempts were made at low oxygen partial pressures and high annealing temperatures (i.e., under strongly reducing conditions). Consequently, the preparation conditions were adjusted to lower temperatures and



TU **Bibliothek**, Die approbierte gedruckte Originalversion dieser Diplomarbeit ist an der TU Wien Bibliothek verfügbar wern vour knowledge hub The approved original version of this thesis is available in print at TU Wien Bibliothek.

 $Cu_2O(111)$ 65

UHV annealing, which typically resulted in a  $(\sqrt{3} \times \sqrt{3})$ R30° reconstruction, although with some areas not covered by pyramids. Moreover, when employing a high cooling rate, a 'quenched' pyramid formation was observed, resulting in a more disorganized arrangement of the features.

Overall, preparing both the  $(1 \times 1)$ -ordered structure and on the  $(\sqrt{3} \times \sqrt{3})$ R30° reconstruction was strongly dependent on the annealing history of the sample, which resulted in a lack of reproducibility in the preparation of the surface structure.

An examination of the LEED-I(V) data regarding sample alignment confirmed that all measurements were precisely adjusted, yielding high-quality data. The ongoing structural calculations will be compared with the provided data in this thesis, aiming to enhance our understanding of the atomic structures of these surfaces.



### 6. Summary and outlook

In this thesis, surface-science studies on SrTiO<sub>3</sub>, La<sub>0.8</sub>Sr<sub>0.2</sub>MnO<sub>3</sub>, and Cu<sub>2</sub>O were conducted. The objective was to prepare the  $(4 \times 1)$  reconstruction of  $SrTiO_3(110)$ , the  $(\sqrt{2} \times \sqrt{2})$ R45° and aperiodic phases of LSMO(001), and both the  $(1 \times 1)$  and the  $(\sqrt{3} \times \sqrt{3})$ R30° surface phases of Cu<sub>2</sub>O(111). All surface structures were successfully achieved, and LEED-I(V) measurements using the ViPErLEED package [41, 43, 44] were performed.

The investigation of SrTiO<sub>3</sub>(110) aligns with previous studies [21], which demonstrate that the near-surface stoichiometry can be adjusted by either the deposition of Sr, or Ar<sup>+</sup> sputtering followed by O<sub>2</sub> annealing. This resulted in the formation of different Sr- or Ti-rich surface reconstructions, respectively, with the possibility of microscopic coexistence, and macroscopic non-uniformity. The data analysis of the LEED-I(V) measurements on the  $(4 \times 1)$ -reconstructed surface revealed challenges in the post-processing stage, as the  $(4 \times 1)$  reconstruction exhibits a splitting of the diffraction spots that introduces an error in the calculation while the intensities of the spots are extracted.

LSMO films were grown on SrTiO<sub>3</sub>(001) substrates via PLD using an LSMO target. The film growth provides an insight into the sensitivity of the film homogeneity to the employed PLD parameters. As-grown films exhibited an  $MnO_x$ -terminated surface, attributed to the aperiodic surface, while  $AO_x$ -terminated films, attributed to the  $(\sqrt{2} \times \sqrt{2})$ R45° periodicity, could be achieved by Ar<sup>+</sup> sputtering followed by annealing in  $O_2$  of the  $MnO_x$  surface. MnO deposition on the  $(\sqrt{2} \times \sqrt{2})R45^{\circ}$ surface restored the aperiodic reconstruction, and a following LSMO deposition also yielded the aperiodic structure. From the comparison of the LEED-I(V) measurements performed on the aperiodic structures, which were prepared in different ways, an R factor of 0.08 was obtained. This suggests that the structures are in perfect agreement with each other. Analyzing the energy dependence of the I(V)curves allowed to distinguish energy ranges where bulk contributions dominate over surface ones.

In the course of preparing the  $(1 \times 1)$ -ordered surface and the  $(\sqrt{3} \times \sqrt{3})$ R30° reconstruction of Cu<sub>2</sub>O(111), several phenomena were observed. These include the appearance of a different phase, possibly related to surface undulations observed



after treating the sample at high oxygen partial pressures. Moreover a disorder in the pyramid arrangement of the  $(\sqrt{3} \times \sqrt{3})R30^{\circ}$  reconstruction was observed, which can be explained by too fast cooling rates. This impedes the migration of the pyramids and quenches their arrangement, resulting in disorder and a broadening of the diffraction spots. In general, the preparation of the  $Cu_2O(111)$  surface exhibited a strong dependence on the annealing history, resulting in poor reproducibility during the surface preparation.

Across all studies, surface reconstructions were highly sensitive to preparation conditions, including deposition techniques, sputtering, annealing, and cooling rates. The parameters influenced the homogeneity of the surfaces. Despite these challenges, the high-quality experimental LEED-I(V) data obtained in this work serves as a foundation for future model validation and structural analysis of the  $SrTiO_3(110)$ , LSMO(001), and  $Cu_2O(111)$  surface.

# Bibliography

- [1] U. Diebold, "The surface science of titanium dioxide", Surface Science Reports **48**, 53–229 (2003).
- [2] G. S. Parkinson and U. Diebold, "Adsorption on Metal Oxide Surfaces", in Surface and Interface Science, edited by K. Wandelt, 1st ed. (Wiley, 2016), pp. 793–817.
- [3] P. Zubko, S. Gariglio, M. Gabay, P. Ghosez, and J.-M. Triscone, "Interface Physics in Complex Oxide Heterostructures", Annual Review of Condensed Matter Physics 2, 141–165 (2011).
- [4] M. Setvín, M. Wagner, M. Schmid, G. S. Parkinson, and U. Diebold, "Surface point defects on bulk oxides: atomically-resolved scanning probe microscopy", Chemical Society Reviews 46, 1772–1784 (2017).
- M. L. Grilli, "Metal Oxides", Metals 10, 820 (2020).
- Y. Wu and T. van Ree, "Energy technologies and their role in our life", in Metal oxides in energy technologies, edited by Y. Wu, Metal Oxides (Elsevier, 2018), pp. 1–16.
- U. Diebold, S.-C. Li, and M. Schmid, "Oxide Surface Science", Annual Review of Physical Chemistry **61**, 129–148 (2010).
- P. W. Tasker, "The stability of ionic crystal surfaces", Journal of Physics C: Solid State Physics 12, 4977 (1979).
- M. Sterrer and H.-J. Freund, "Properties of Oxide Surfaces", in Surface and Interface Science, edited by K. Wandelt, 1st ed. (Wiley, Nov. 2013), pp. 229– 278.
- [10] F. Jona, J. A. Strozier, and W. S. Yang, "Low-energy electron diffraction for surface structure analysis", Reports on Progress in Physics 45, 527–585 (1982).
- "Bragg law Definition, Equation, Diagram, & Facts Britannica", (2024).
- J. M. Cowley, "Diffraction from crystals", in *Diffraction Physics* (Elsevier, 1995), pp. 123–144.

- [13] D. Schwarzenbach and A. A. Pinkerton, Crystallography (J. Wiley, New York, 1996).
- [14]M. Schmid, "Experimentelle Methoden der Oberflächenphysik", 2023.
- [15] K. W. Kolasinski, Surface science: foundations of catalysis and nanoscience, 3rd ed (Wiley, Chichester, West Sussex; Hoboken, N.J., 2012).
- W. Borchardt-Ott, Kristallographie: eine Einführung für Naturwissenschaftler, 6., überarb. und erw. Aufl, Springer-Lehrbuch (Springer, Berlin Heidelberg New York Barcelona Hongkong London Mailand Paris Singapur Tokio, 2002).
- M. Henzler, "LEED studies of surface imperfections", Applications of Surface Science 11-12, 450-469 (1982).
- [18] W. Moritz and M. A. Van Hove, Surface structure determination by LEED and X-rays, First edition (Cambridge University Press, United Kingdom; New York, NY, USA, 2022).
- E. J. Mittemeijer and U. S. Welzel, eds., Modern diffraction methods (Wiley-VCH, Weinheim, 2013).
- J. B. Pendry, "Reliability factors for LEED calculations", Journal of Physics [20]C: Solid State Physics **13**, 937–944 (1980).
- [21] G. Franceschi, "Pulsed Laser Deposition of Functional Oxides with Atomic Scale Control", PhD thesis (TU Wien, 2020).
- S. Gerhold, M. Riva, B. Yildiz, M. Schmid, and U. Diebold, "Adjusting island density and morphology of the  $SrTiO_3(110)$ - $(4 \times 1)$  surface: pulsed laser deposition combined with scanning tunneling microscopy", Surface Science, 76–83 (2016).
- T. Ohnishi, H. Koinuma, and M. Lippmaa, "Pulsed laser deposition of oxide [23]thin films", Applied Surface Science 252, 2466–2471 (2006).
- R. Eason, ed., Pulsed Laser Deposition of Thin Films: Applications-Led Growth [24]of Functional Materials, 1st ed. (Wiley, Nov. 2006).
- J. Chen, M. Döbeli, D. Stender, K. Conder, A. Wokaun, C. W. Schneider, and [25]T. Lippert, "Plasma interactions determine the composition in pulsed laser deposited thin films", Applied Physics Letters 105, 114104 (2014).
- [26] G. Koster, D. Blank, and G. Rijnders, "Oxygen in Complex Oxide Thin Films Grown by Pulsed Laser Deposition: a Perspective", Journal of Superconductivity and Novel Magnetism 33, 10.1007/s10948-019-05276-5 (2020).

- [27] M. Koubaa, A. M. Haghiri-Gosnet, R. Desfeux, P. Lecoeur, W. Prellier, and B. Mercey, "Crystallinity, surface morphology, and magnetic properties of La<sub>0.7</sub>Sr<sub>0.3</sub>MnO<sub>3</sub> thin films: An approach based on the laser ablation plume range models", Journal of Applied Physics 93, 5227–5235 (2003).
- A. Ojeda-G-P, M. Döbeli, and T. Lippert, "Influence of Plume Properties [28]on Thin Film Composition in Pulsed Laser Deposition", Advanced Materials Interfaces 5, 1701062 (2018).
- [29] G. Franceschi, M. Schmid, U. Diebold, and M. Riva, "Atomically resolved surface phases of La<sub>0.8</sub>Sr<sub>0.2</sub>MnO<sub>3</sub>(110) thin films", Journal of Materials Chemistry A 8, 22947–22961 (2020).
- S. N. Magonov and M.-H. Whangbo, "Scanning probe microscopes", in *Surface* analysis with STM and AFM (John Wiley & Sons, Ltd, 1995) Chap. 3, pp. 21-46.
- M. Schmid and G. Pietrzak, "STM", [31]
- J. Tersoff and N. Lang, Scanning Tunneling Microscopy, Google-Books-ID: [32]MtHq0mgF5WgC (Academic Press, Mar. 1993).
- H. Uchida, D. Huang, J. Yoshinobu, and M. Aono, "Single-atom manipulation [33]on the Si(111)  $(7 \times 7)$  surface by the scanning tunneling microscope (STM)", Surface Science **287-288**, 1056–1061 (1993).
- [34] P. Eaton and P. West, Atomic Force Microscopy (Oxford University Press, Mar. 2010).
- G. Haugstad, Atomic force microscopy: understanding basic modes and advanced applications, 1. ed (Wiley, Hoboken, NJ, 2012).
- [36]W. C. Sanders, Atomic force microscopy: fundamental concepts and laboratory investigations (CRC Press/Taylor and Francis, Boca Raton, FL, 2020).
- D. P. Woodruff and T. A. Delchar, Modern Techniques of Surface Science, 2nd ed. (Cambridge University Press, Mar. 1994).
- J. A. Colón Santana, Quantitative Core Level Photoelectron Spectroscopy: A primer (Morgan & Claypool Publishers, Mar. 2015).
- [39] L. Meitner, "Über die  $\beta$ -Strahl-Spektra und ihren Zusammenhang mit der  $\gamma$ -Strahlung", Zeitschrift für Physik **11**, 35–54 (1922).

- [40] J. Wolstenholme, Auger Electron Spectroscopy: Practical Application to Materials Analysis and Characterization of Surfaces, Interfaces, and Thin Films (Momentum Press, New York, UNITED STATES, 2015).
- [41] F. Dörr, M. Schmid, L. Hammer, M. Riva, E. Rheinfrank, M. Schmid, U. Diebold, L. Hammer, and M. Riva, "ViPErLEED package III: Data acquisition for quantitative low-energy electron diffraction", (2024).
- [42] R. Koller, W. Bergermayer, G. Kresse, C. Konvicka, M. Schmid, J. Redinger, R. Podloucky, and P. Varga, "The structure of the oxygen-induced  $c(6 \times 2)$ reconstruction of V(110)", Surface Science 512, 16–28 (2002).
- M. Schmid, F. Kraushofer, A. M. Imre, T. Kißlinger, L. Hammer, U. Diebold, [43]and M. Riva, "ViPErLEED package II: Spot tracking, extraction and processing of I(V) curves", 10.48550/ARXIV.2406.18413 (2024).
- [44] F. Kraushofer, A. M. Imre, G. Franceschi, T. Kißlinger, E. Rheinfrank, M. Schmid, U. Diebold, L. Hammer, and M. Riva, "ViPErLEED package I: Calculation of I(V) curves and structural optimization", 10.48550/ARXIV.2406. 18821 (2024).
- [45] M. Naito and H. Sato, "Reflection high-energy electron diffraction study on the SrTiO<sub>3</sub> surface structure", Physica C: Superconductivity **229**, 1–11 (1994).
- T. K. Andersen, S. Wang, M. R. Castell, D. D. Fong, and L. D. Marks, [46]"Single-layer TiO<sub>x</sub> reconstructions on SrTiO<sub>3</sub>(111):  $(\sqrt{7} \times \sqrt{7})$ R19.1°,  $(\sqrt{13} \times \sqrt{13})$  $\sqrt{13}$ )R13.9°, and related structures", Surface Science **675**, 36–41 (2018).
- F. Yang, Q. Zhang, Z. Yang, J. Gu, Y. Liang, W. Li, W. Wang, K. Jin, L. Gu, [47]and J. Guo, "Room-temperature ferroelectricity of SrTiO<sub>3</sub> films modulated by cation concentration", Applied Physics Letters 107, 082904 (2015).
- [48] I. Sokolović, M. Schmid, U. Diebold, and M. Setvin, "Incipient ferroelectricity: A route towards bulk-terminated SrTiO<sub>3</sub>", Physical Review Materials 3, 034407 (2019).
- [49] Z. Wang, F. Yang, Z. Zhang, Y. Tang, J. Feng, K. Wu, Q. Guo, and J. Guo, "Evolution of the surface structures on SrTiO<sub>3</sub>(110) tuned by Ti or Sr concentration", Physical Review B 83, 155453 (2011).
- [50] Y. S. Kim, D. J. Kim, T. H. Kim, T. W. Noh, J. S. Choi, B. H. Park, and J.-G. Yoon, "Observation of room-temperature ferroelectricity in tetragonal strontium titanate thin films on SrTiO<sub>3</sub>(001) substrates", Applied Physics Letters **91**, 042908 (2007).

- [51] M. Kawasaki, A. Ohtomo, T. Arakane, K. Takahashi, M. Yoshimoto, and H. Koinuma, "Atomic control of SrTiO<sub>3</sub> surface for perfect epitaxy of perovskite oxides", Applied Surface Science 107, 102–106 (1996).
- K. S. Takahashi, M. Gabay, D. Jaccard, K. Shibuya, T. Ohnishi, M. Lippmaa, and J.-M. Triscone, "Local switching of two-dimensional superconductivity using the ferroelectric field effect", Nature 441, 195–198 (2006).
- [53] K. Shibuya, T. Ohnishi, T. Uozumi, T. Sato, M. Lippmaa, M. Kawasaki, K. Nakajima, T. Chikyow, and H. Koinuma, "Field-effect modulation of the transport properties of nondoped SrTiO<sub>3</sub>", Applied Physics Letters 88, 212116 (2006).
- Z. Wang, Z. Zhong, X. Hao, S. Gerhold, B. Stöger, M. Schmid, J. Sánchez-Barriga, A. Varykhalov, C. Franchini, K. Held, and U. Diebold, "Anisotropic two-dimensional electron gas at SrTiO<sub>3</sub>(110)", Proceedings of the National Academy of Sciences of the United States of America 111, 3933–3937 (2014).
- A. Biswas, M. Talha, A. Kashir, and Y. H. Jeong, "A thin film perspective on quantum functional oxides", Current Applied Physics 19, 207–214 (2019).
- T. Ruh, D. Berkovec, F. Schrenk, and C. Rameshan, "Exsolution on perovskite oxides: morphology and anchorage of nanoparticles", Chemical Communications **59**, 3948–3956 (2023).
- A. Žužić, A. Ressler, and J. Macan, "Perovskite oxides as active materials in [57]novel alternatives to well-known technologies: A review", Ceramics International 48, 27240–27261 (2022).
- A. Biswas, P. B. Rossen, C.-H. Yang, W. Siemons, M.-H. Jung, I. K. Yang, R. Ramesh, and Y. H. Jeong, "Universal Ti-rich termination of atomically flat  $SrTiO_3(001)$ , (110), and (111) surfaces", Applied Physics Letters 98, 051904 (2011).
- J. A. Enterkin, A. K. Subramanian, B. C. Russell, M. R. Castell, K. R. Poeppelmeier, and L. D. Marks, "A homologous series of structures on the surface of SrTiO<sub>3</sub>(110)", Nature Materials 9, 245–248 (2010).
- Z. Wang, A. Loon, A. Subramanian, S. Gerhold, E. McDermott, J. A. Enterkin, M. Hieckel, B. C. Russell, R. J. Green, A. Moewes, J. Guo, P. Blaha, M. R. Castell, U. Diebold, and L. D. Marks, "Transition from Reconstruction toward Thin Film on the (110) Surface of Strontium Titanate", Nano Letters 16, Publisher: American Chemical Society, 2407–2412 (2016).

- [61] Z. Wang, F. Li, S. Meng, J. Zhang, E. W. Plummer, U. Diebold, and J. Guo, "Strain-Induced Defect Superstructure on the SrTiO<sub>3</sub>(110) Surface", Physical Review Letters 111, 056101 (2013).
- "Vapor Pressure Calculator [IAP/TU Wien]", [62]
- C. Sun, R. Hui, and J. Roller, "Cathode materials for solid oxide fuel cells: a [63]review", Journal of Solid State Electrochemistry 14, 1125–1144 (2010).
- S. P. Jiang, "Development of lanthanum strontium manganite perovskite cathode materials of solid oxide fuel cells: a review", Journal of Materials Science **43**, 6799–6833 (2008).
- S. Majumdar and S. V. Dijken, "Pulsed laser deposition of  $La_{1-x}A_xMnO_3$ : thin-film properties and spintronic applications", Journal of Physics D: Applied Physics 47, 034010 (2014).
- [66] Z. Liao and J. Zhang, "Metal-to-Insulator Transition in Ultrathin Manganite Heterostructures", Applied Sciences 9, 144 (2019).
- J. Hemberger, A. Krimmel, T. Kurz, H.-A. Krug von Nidda, V. Y. Ivanov, A. A. Mukhin, A. M. Balbashov, and A. Loidl, "Structural, magnetic, and electrical properties of single-crystalline  $La_{1-x}Sr_xMnO_3$  (0.4 < x < 0.85)", Phys. Rev. B **66**, 094410 (2002).
- L. Rørmark, K. Wiik, S. Stølen, and T. Grande, "Oxygen stoichiometry and structural properties of  $La_{1-x}A_xMnO_{3\pm\delta}$  (A = Ca or Sr and  $0 \le x \le 1$ )", Journal of Materials Chemistry 12, 1058–1067 (2002).
- G. Franceschi, R. Heller, M. Schmid, U. Diebold, and M. Riva, "Evolution of the surface atomic structure of multielement oxide films: curse or blessing?", Nanoscale Advances 5, 7009–7017 (2023).
- [70] E. Rheinfrank, M. Brunthaler, M. Kienzer, G. Franceschi, P. Matvija, M. Schmid, U. Diebold, and M. Riva, "Reversible transformation between B-site and A-site-rich surfaces by Ar<sup>+</sup> sputtering and mn deposition on La<sub>0.8</sub>Sr<sub>0.2</sub>MnO<sub>3</sub>(001)", in preparation (2024).
- E. Rheinfrank, "Growth and Surface Structures of La<sub>0.8</sub>Sr<sub>0.2</sub>MnO<sub>3</sub>(001)", PhD thesis (TU Wien, 2024).
- I. Sokolović, G. Franceschi, Z. Wang, J. Xu, J. Pavelec, M. Riva, M. Schmid, U. Diebold, and M. Setvín, "Quest for a pristine unreconstructed SrTiO<sub>3</sub>(001) surface: An atomically resolved study via noncontact atomic force microscopy", Physical Review B **103**, L241406 (2021).



- [73] S. A. Chambers, T. C. Droubay, C. Capan, and G. Y. Sun, "Unintentional F doping of  $SrTiO_3(001)$  etched in HF acid-structure and electronic properties", Surface Science **606**, 554–558 (2012).
- [74] K. H. Schulz and D. F. Cox, "Photoemission and low-energy-electron-diffraction study of clean and oxygen-dosed Cu<sub>2</sub>O (111) and (100) surfaces", Physical Review B **43**, 1610–1621 (1991).
- [75] F. Jensen, F. Besenbacher, and I. Stensgaard, "Two new oxygen induced reconstructions on cu(111)", Surface Science **269-270**, 400-404 (1992).
- [76] B. K. Meyer, A. Polity, D. Reppin, M. Becker, P. Hering, P. J. Klar, T. Sander, C. Reindl, J. Benz, M. Eickhoff, C. Heiliger, M. Heinemann, J. Bläsing, A. Krost, S. Shokovets, C. Müller, and C. Ronning, "Binary copper oxide semiconductors: From materials towards devices", physica status solidi (b) **249**, 1487–1509 (2012).
- J. Robertson and S. J. Clark, "Limits to doping in oxides", Physical Review |77|B **83**, 075205 (2011).
- H. Raebiger, S. Lany, and A. Zunger, "Origins of the p-Type Nature and Cation Deficiency in Cu<sub>2</sub>O and Related Materials", Physical Review. B, Condensed Matter and Materials Physics 76, 10.1103/PhysRevB.76.045209 (2007).
- [79] C. Wang, H. Tissot, C. Escudero, V. Pérez-Dieste, D. Stacchiola, and J. Weissenrieder, "Redox Properties of Cu<sub>2</sub>O(100) and (111) Surfaces", The Journal of Physical Chemistry C 122, Publisher: American Chemical Society, 28684-28691 (2018).
- [80] W. Zhao, R. P. Babu, T. Chang, I. Odnevall, P. Hedström, C. M. Johnson, and C. Leygraf, "Initial atmospheric corrosion studies of copper from macroscale to nanoscale in a simulated indoor atmospheric environment", Corrosion Science **195**, 109995 (2022).
- [81] K. Hayashida, Y. Tsuda, T. Yamada, A. Yoshigoe, and M. Okada, "Revisit of XPS Studies of Supersonic O<sub>2</sub> Molecular Adsorption on Cu(111): Copper Oxides", ACS Omega 6, Publisher: American Chemical Society, 26814–26820 (2021).

- [82] M. Hara, T. Kondo, M. Komoda, S. Ikeda, J. N. Kondo, K. Domen, M. Hara, K. Shinohara, and A. Tanaka, "Cu<sub>2</sub>O as a photocatalyst for overall water splitting under visible light irradiation", Chemical Communications, 357–358 (1998).
- [83] A. Gloystein, J. A. Creed, and N. Nilius, "Atomic view on the (111) Surface of a Cu<sub>2</sub>O single crystal: Reconstruction, Electronic Properties, and Band-Bending Effects", The Journal of Physical Chemistry C 126, Publisher: American Chemical Society, 16834–16840 (2022).
- A. Gloystein, N. Nilius, J. Goniakowski, and C. Noguera, "Nanopyramidal [84]Reconstruction of Cu<sub>2</sub>O(111): A Long-Standing Surface Puzzle Solved by STM and DFT", The Journal of Physical Chemistry C 124, Publisher: American Chemical Society, 26937–26943 (2020).
- A. Önsten, M. Göthelid, and U. O. Karlsson, "Atomic structure of Cu<sub>2</sub>O(111)", Surface Science **603**, 257–264 (2009).
- [86] F. Biccari, "Defects and Doping in Cu<sub>2</sub>O", PhD thesis (Sapienza Università di Roma, Rome (Italy), 2009).
- [87] R. Zhang, L. Li, L. Frazer, K. B. Chang, K. R. Poeppelmeier, M. K. Y. Chan, and J. R. Guest, "Atomistic determination of the surface structure of Cu<sub>2</sub>O(111): experiment and theory", Physical Chemistry Chemical Physics **20**, 27456–27463 (2018).
- G. Franceschi, M. Wagner, J. Hofinger, T. š. Kraj ňák, M. Schmid, U. Diebold, and M. Riva, "Growth of In<sub>2</sub>O<sub>3</sub>(111) thin films with optimized surfaces", Phys. Rev. Mater. 3, 103403 (2019).
- M. Schmid, "Chemical potential Calculator [IAP/TU Wien]",
- T. T. Ly, T. Lee, S. Kim, Y.-J. Lee, G. Duvjir, K. Jang, K. Palotás, S.-Y. Jeong, A. Soon, and J. Kim, "Growing ultrathin Cu<sub>2</sub>O films on highly crystalline Cu(111): a closer inspection from microscopy and theory", The Journal of Physical Chemistry C 123, Publisher: American Chemical Society, 12716– 12721 (2019).

# Acknowledgements

First and foremost, I would like to sincerely thank Univ. Prof.in Dr.in Ulrike Diebold for the opportunity to work on my thesis in the surface science group, for her excellent supervision, and for always being available with helpful advice.

I am deeply grateful to Dr. Michele Riva for his outstanding supervision throughout this work and for the extensive support and guidance he provided whenever needed.

A special thanks goes to Erik Rheinfrank for patiently introducing me to the PLD lab and for offering his help at any time.

And of course, I would also like to express my thanks to the entire surface science group for being simply amazing.

I would like to thank my family for their unwavering support throughout my whole life.

Moreover, I would like to thank my wonderful friends — life would not be the same without you!

And lastly, thank you Thomas, for everything.